

Title: Atomic-scale characterization of the oxidation state of Ti in meteoritic hibonite: Implications for early solar system thermodynamics

Manuscript Number: 8311R

Authors: Pierre-marie Zanetta, University of Arizona Venkat Manga, University of Arizona Yao-Jen Chang, University of Arizona Tarunika Ramprasad, University of Arizona Juliane Weber, Oak Ridge National Laboratory John Beckett, California Institute of Technology Thomas Zega, University of Arizona

24 Using a series of Ti-bearing oxides, we find that the onset intensity of the Ti $L_{2,3}$ edge decreases as
25 a function of increasing Ti-oxidation state, which is corroborated by simulated Ti-oxide spectra using
26 first-principles density-functional theory. We test the relationship on a set of synthetic hibonite grains
27 with known $Ti^{4+}/\Sigma Ti$ values and apply the developed method on a hibonite grain from a compact type
28 A inclusion in the Northwest Africa (NWA) 5028 CR2 carbonaceous chondrite. The STEM-EELS data
29 show that the chondritic hibonite grain is zoned with a $Ti^{4+}/\Sigma Ti$ ratio ranging from 0.75 ± 0.04 to
30 0.96 ± 0.04 over a scale of 100 nm between the core and edge of the grain, respectively. The Ti
31 substitution sites are characterized by experimental and calculated high-angle annular-dark-field
32 (HAADF) images and atomic-level EEL spectrum imaging. Simulated HAADF images reveal that Ti is
33 distributed between the M2 and M4 sites while Mg sites on the M3 site. Quantitative energy-
34 dispersive X-ray spectroscopy shows that this grain is also zoned in Al and Ti. The Mg distribution, in
35 contrast, does not match that for Ti at the nanoscale.

36 The spatial decoupling of the element composition and Ti-oxidation states suggests a multistage
37 evolution for this hibonite grain. We hypothesize that Ti and Mg were incorporated into the structure
38 during condensation at high temperature through multiple reactions. Transient heating, presumably in
39 the solar nebula, adds complexity to the crystal chemistry and potentially redistributed Ti and Mg.
40 Concurrently, the formation of oxygen vacancies as a result of a reducing gas, led to the reduction of
41 Ti^{4+} to Ti^{3+} . The multiple defect reactions occurring in this single hibonite crystal precludes a simple
42 relationship between the $Ti^{4+}/\Sigma Ti$ and the fO_2 of formation. However, moving forward, these
43 measurements are fundamental input for modeling of the thermodynamic conditions under which
44 hibonite formed in the early solar nebula.

45

46 **Keywords:** hibonite, Ti oxidation state, STEM-EELS, chondrites, CAIs, thermodynamic, early solar
47 system, atomic scale, DFT calculations.

INTRODUCTION

48
49
50
51
52
53
54
55
56
57
58
59
60
61
62
63
64
65
66
67
68
69
70
71

The sun and planets formed out of a rotating disk of gas and dust over four billion years ago. It was hypothesized that the temperature of the inner solar nebula was high enough such that solid materials experienced melting, evaporation, and condensation (Cameron 1962). Thermodynamic models subsequently predicted that as the solar gas cooled, solid materials condensed out of it according to their volatility, with the most refractory phases forming at the highest temperatures (Lord 1965; Larimer 1967; Grossman 1972; Lewis 1974; Yoneda and Grossman 1995; Ebel and Grossman 2000; Lodders 2003; Ebel 2006; Grossman et al. 2008; Scott and Krot 2014; Zega et al. 2021). Evidence for such condensation is provided by the mineral assemblages found in Ca-Al-rich inclusions (CAIs) within primitive chondrites. With radiometric age dates of 4.5673 ± 0.00016 billion years (Amelin et al. 2009; Connelly et al. 2012), CAIs mark time zero for our solar system, and our chronological understanding of its evolution is anchored to that time stamp.

Common CAI phases include melilite, spinel, perovskite, hibonite, Ca-pyroxene and forsterite usually with lesser amounts of grossite, metal, and corundum (MacPherson 2014). The composition and structure of these CAI phases are key to determining the chemical pathways through which they formed and to quantifying the conditions under which they condensed or were subsequently altered, whether in the solar nebula or on chondrite parent bodies (Beckett et al. 1988; Simon et al. 1991, 1997; Keller and Buseck 1994; Connolly and Burnett 2003; Grossman et al. 2008; Chi et al. 2009). Thus, measurement of CAI phases from the bulk scale down to the atomic level allows us to gain insight into the thermodynamic landscape surrounding their origins.

Hibonite (nominally $\text{CaAl}_{12}\text{O}_{19}$) is among the first few phases predicted to form, at temperatures between 1400 and 1900 K, in thermodynamic models that consider a cooling gas of solar composition (e.g., (Yoneda and Grossman 1995; Ebel and Grossman 2000; Lodders 2003; Zega et al. 2021). Hibonite

72 can incorporate a variety of solutes into its crystal structure, including: Mg^{2+} , Zn^{2+} , Fe^{2+} and Fe^{3+} , V^{3+}
73 and V^{4+} , Ti^{3+} and Ti^{4+} , Si^{4+} and Th^{4+} as **minor and trace elements** (Allen et al. 1978; Beckett et al. 1988;
74 Bermanec et al. 1996; Rakotondrazafy et al. 1996; Simon et al. 1997). Titanium is particularly
75 important because it is often found in significant concentrations in meteoritic hibonite (>0.1 cations
76 per formula unit (Brearley and Jones 1998)) and it can occur in multiple oxidation states, thereby
77 providing a **redox sensor** of nebular conditions (Allen et al. 1978; Armstrong et al. 1982; Beckett et al.
78 1988; Doyle et al. 2014; Ardit et al. 2016). Quantitative measurement of the Ti oxidation state in
79 hibonite can, therefore, provide fundamental information on the thermodynamic conditions under
80 which it formed or last equilibrated, e.g., composition of the gas, temperature of condensation or
81 thermal processing, and oxygen fugacity (fO_2) (Beckett et al. 1988).

82 Hibonite is part of the magnetoplumbite group of minerals. It has a space group symmetry of
83 $P6_3/mmc$ and is characterized by unit cell parameters $a \approx 5.5\text{\AA}$, $c \approx 22.0\text{\AA}$ (Curien et al. 1956; Bermanec
84 et al. 1996; Nagashima et al. 2010; Holtstam and Hålenius 2020a). This structure contains six cation
85 sites and five oxygen sites. Ca occupies a 12-coordinated polyhedron, whereas the aluminum is
86 distributed among five crystallographic sites (named hereafter M1–M5). M1, M4, and M5 are
87 octahedra, M3 is a tetrahedron, M2 is a trigonal bipyramid, and the atoms within these sites form
88 polyhedral layers perpendicular to the c axis of the hexagonal cell. Atomic substitutions occur
89 abundantly in the hibonite structure, and so the detailed crystal chemistry becomes fundamental to
90 inferring precisely the thermodynamic conditions of the nebular gas at its origin. However, the
91 reactions at the origin of the Ti incorporation, oxidation, and the location of the substitution in the
92 structure are still debated. Ti can be incorporated into the hibonite structure mainly through two
93 pathways. Ti^{3+} can substitute directly for Al^{3+} , or Ti^{4+} and Mg^{2+} can couple substitute for two Al^{3+} (Allen
94 et al. 1978; Bermanec et al. 1996; Nagashima et al. 2010; Doyle et al. 2014; Berry et al. 2017). The
95 oxidation state of Ti can be further affected by the presence of O vacancies and cation defects, both of

96 which are expected to occur in the structure (Beckett et al. 1988; Asaduzzaman et al. 2021). Regarding
97 the location of the Ti substitution within the M sites (Al), Beckett et al. (1988) proposed that Ti^{3+}
98 occupies the M2 site while Ti^{4+} occupies the M4 site. More recently, Doyle et al. (2014, 2016)
99 proposed that Ti^{3+} does not occupy the M2 site, but instead occupies the M4 octahedral site, and Ti^{4+}
100 partitions between the M2 trigonal bipyramidal and the M4 octahedral sites. The Mg (when balancing
101 the charge of the Ti) is expected to occupy the M3 site. Oxygen vacancies can also occur and modify
102 the Mg and Ti partitioning (Beckett et al. 1988). The distribution of Ti within the M2 and M4 sites was
103 recently observed by coupling STEM-HAADF and energy dispersive spectroscopy (EDS) measurements
104 (Han et al. 2021). However, the $Ti^{4+}/\Sigma Ti$ distribution over these sites has not yet been investigated by
105 direct measurement. Thus, establishing a clear connection between the cation site occupancy and the
106 oxidation state of Ti in hibonite is crucial to understanding the nature of the substitution reactions,
107 their thermodynamic history, and what they tell us about the thermodynamic landscape of the solar
108 nebula.

109 Here, we examine the oxidation state of Ti and the chemistry of hibonite via EDS and EELS in an
110 aberration-corrected scanning transmission electron microscope. We: (1) report an alternative
111 method for the quantification of Ti-oxidation state in Ti-bearing oxides using EELS; (2) examine the
112 $Ti^{4+}/\Sigma Ti$ variations in meteoritic hibonite down to the atomic scale; (3) provide new information on the
113 Ti site substitution; and (4) link the $Ti^{4+}/\Sigma Ti$ variation as well as chemical zonation to the
114 thermodynamic history of a hibonite grain from the Northwest Africa (NWA) 5028 CR2 chondrite. We
115 propose that the approach used here is an important steppingstone for the analysis of other Ti-
116 bearing oxides in primitive planetary materials and rigorous treatment of the kinds of defect reactions
117 recorded by them.

118

119

SAMPLES AND METHODS

120 EELS has been used for decades to obtain information on oxidation states of 3d metals in a wide
121 range of earth, planetary, and synthetic materials from micro to nanoscales (Leapman et al., 1982;
122 Brydson et al., 1993; Garvie et al., 1994; Van Aken et al., 1998; Garvie and Buseck, 1998; Van Aken and
123 Liebscher, 2002; Zega et al., 2003; Muller et al., 2008; Chi et al., 2009; Shao et al., 2010; Tan et al.,
124 2011; 2012). Fitting of linear mixing models on energy-loss near-edge structure (ELNES) is one such
125 approach but requires standards whose valence states, coordination polyhedra, and crystal fields
126 ideally match those of the unknown (e.g., Garvie and Buseck, 1998a; Zega et al., 2003). In comparison,
127 the white-line method, so called because the absorption edges of EELS spectra were first observed on
128 photographic film as white lines (Azaroff and Pease 1974), monitors the chemical shift of EELS spectra
129 to higher energy loss with increasing oxidation state using integration windows (Leapman et al. 1982;
130 Garvie et al. 1994; Garvie and Buseck 1998; Van Aken et al. 1998; Van Aken and Liebscher 2002;
131 Stoyanov et al. 2007). The advantage of the white-line method is that it can accommodate materials
132 with varied crystal chemistry (electrical properties, orientation, site symmetry, etc.) without the need
133 to synthesize endmembers (with systematically varied $Ti^{4+}/\Sigma Ti$ ratios) as is the case with a method
134 based on curve fitting. Previous workers developed a calibration curve for Ti based on the white-line
135 approach (Stoyanov et al. 2007). Thus, our purpose here is to modify it as needed to reflect our
136 laboratory and electron-optical conditions.

137

138 **Samples**

139 To reproduce the white-line ratio method, we acquired seven high-purity (>99.8%) standards with
140 known amounts of Ti^{4+} and Ti^{3+} . These materials and their Ti-oxidation states include: TiO (Ti^{2+}), Ti_2O_3
141 (Ti^{3+}), Ti_3O_5 ($Ti^{4+}:Ti^{3+}= 1:2$), Ti_4O_7 ($Ti^{4+}:Ti^{3+}= 1:1$), TiO_2 (Ti^{4+}), $FeTiO_3$ (Ti^{4+}), $CaTiO_3$ (Ti^{4+}). All were acquired
142 from commercial suppliers (CERAC, Alfa Aesar, Phelly Materials, and SigmaAldrich) in powder form
143 except Ti_4O_7 , which was kindly provided by Dr. Lindsay Keller (Keller 1995). Standards were crushed in

144 a agate stone mortar and pestle in dry conditions and deposited onto lacey-carbon films supported by
145 Cu-mesh TEM grids (Fig. S1a). The dry conditions avoided the use of solvents and hence possible
146 alteration of the samples but some grain clustering (up to 200 nm) occurred during the sprinkling of
147 the particles. We measured only those particles that are monodisperse and electron transparent (<
148 100 nm in thickness, see Fig. S1).

149 We also examined synthetic hibonites equilibrated under conditions of controlled temperature
150 and oxygen fugacity (fO_2). We measured the 'ALL' samples reported in [Ihinger and Stolper \(1986\)](#) and
151 [Beckett et al. \(1988\)](#) because their composition and Ti oxidation states are comparable to meteoritic
152 samples. The compositions of these synthetic hibonite samples correspond to the average
153 composition of hibonite in the CG-11 inclusion in the Allende CV3 chondrite. They were chosen
154 because they contain significantly lower concentration of V (which can occur as V^{4+} and V^{3+}) and a
155 higher Ti concentration than the Blue Angel (BA) inclusion from the Murchison meteorite (0.39 vs 1.1
156 V_2O_3 wt.% and 7.3 vs 4.1 TiO2 wt%, respectively) than the BA samples (see [Armstrong et al, 1982](#)).

157 The $Ti^{4+}/\Sigma Ti$ of these samples was originally measured by electron spin resonance (ESR)
158 spectroscopy ([Beckett et al. 1988](#)). We selected the extreme and an intermediate sample of the series
159 that correspond to $Ti^{4+}/\Sigma Ti$ of 0.85 ± 0.01 , 0.91 ± 0.01 , and 0.95 ± 0.01 for ALL 2-55, ALL2-57, and ALL2-6,
160 respectively. Chips from these experiments were embedded in epoxy bullets and polished. Our goal
161 with these measurements was to confirm the accuracy of the calibration using orthogonal approaches
162 of EELS and ESR, and to relate the $Ti^{4+}/\Sigma Ti$ ratio to the fO_2 under which meteoritic hibonite formed or
163 last equilibrated.

164 To test the efficacy of our calibration and apply it to meteoritic hibonite, we examined a CAI within
165 the CR2 chondrite NWA 5028 (thin section from the Center for Meteorite Studies, Arizona State
166 University collection #1845-5). The CAI was identified as a compact type-A (CTA) ([Ramprasad et al.](#)
167 [2018](#)) ([Ramprasad et al. 2018](#)). The hibonite grain is attached to the rim of the CAI (see the RS2 area in

168 [Ramprasad et al. 2018](#)) and identified and quantified using a Cameca SX-100 electron microprobe,
169 located in the Kuiper Materials Imaging and Characterization Facility (KMICF) at the Lunar and
170 Planetary Laboratory, University of Arizona. A 1- μm probe with an acceleration voltage of 15 kV and
171 beam current of 20 nA was used for the analyses, with counting times of 8 to 20 s on the peaks and 4
172 to 10 s on the background for each element. Mg, Na, Si and Al intensity were acquired on a TAP
173 crystal; Ca, Ti, K, Cr, P and Cl on a PET crystal; and Fe, Mn and V on an LIF crystal. Petrographic
174 description of the CAI is reported in [Ramprasad et al. \(2018\)](#).

175 We prepared electron-transparent cross sections of the four hibonite samples (3 synthetic and 1
176 meteoritic hibonite) using the ThermoScientific (formerly FEI) Helios NanoLab 660 G³ focused-ion-
177 beam scanning-electron microscope (FIB-SEM) also located in KMICF. The general procedures of FIB
178 sample preparation, e.g., coarse cutting, lift out, and in situ thinning were previously described ([Zega
179 et al., 2007; 2020](#)) but we note some exceptions briefly here. Rather than attach the FIB sections to Cu
180 support grids in flagpole-style geometry, we used the top of one of the posts that has an M-shape
181 configuration (Fig. S1b) to aid in securing the section on both sides and minimize bending. We created
182 electron-transparent windows of 6 μm x 8 μm . Other areas of the synthetic hibonite FIB sections were
183 kept thick \sim 500 nm, i.e., electron opaque. This mounting approach provided additional stability to the
184 FIB section that was necessary in order to obtain very thin (<40 nm) samples for atomic-resolution
185 analyses. All samples were ion polished down to 8 keV acceleration voltage to remove the amorphous
186 damage layer on each surface created by higher-voltage milling ([Schaffer et al. 2012](#)).

187

188 **STEM**

189 The Ti standards and the natural and synthetic hibonites were measured using a 200 keV
190 aberration-corrected Hitachi HF5000 scanning TEM (S/TEM). The HF5000 is equipped with a cold field-
191 emission gun, a third-order spherical-aberration corrector for STEM mode, bright-field (BF) and

192 annular dark field (ADF) STEM detectors, an Oxford Instruments X-Max N 100 TLE EDS system with
193 dual 100 mm^2 windowless silicon-drift detectors with solid angle (Ω) of 2.0 sr, and a Gatan Quantum
194 ER (model 965) electron energy-loss spectrometer (EELS). The Quantum ER is a Gatan Imaging Filter
195 (GIF) equipped with a 2048×2048 CCD detector and dual EELS capabilities for simultaneous
196 acquisition of low- and core-loss spectra. STEM-HAADF images were acquired using a 200 keV
197 acceleration voltage, a $10 \mu\text{A}$ emission current, and 3.45 eV extraction voltage, a STEM condenser
198 aperture of $25 \mu\text{m}$, and a $2 \mu\text{s}$ dwell time.

199 Three types of EELS spectrum-imaging experiments were performed. These experiments include:
200 (1) large ($30 \times 30 \text{ nm}$ up to $150 \times 150 \text{ nm}$) field-of-view measurements to compare the Ti-oxide
201 standards and the hibonite samples (both natural and synthetic) under the same electron-optical
202 conditions; (2) large field-of-view ($135 \times 135 \text{ nm}$) measurements using a higher probe current and a
203 larger collection angle than in (1); and (3) atomic-resolution maps (field of view: $6.2 \text{ nm} \times 2.5 \text{ nm}$) of
204 the natural hibonite. Each experiment was performed in STEM mode using a similar condition as for
205 the HAADF images. All EELS spectra were corrected for channel-to-channel gain variation and dark
206 current. Each standard and synthetic sample was analyzed two times to verify the reproducibility of
207 results. For the standards, the two measurements represent different grains with different
208 orientations located in different areas on the lacey film of the TEM grid. For the synthetic hibonites,
209 spectra were acquired from different locations in the FIB section.

210 The experimental conditions for the EELS spectrum imaging are as follows. (1) For large field-of-
211 view analysis, the microscope was operated using a 100 pm probe, a STEM condenser aperture of 25
212 μm , a 105 pA probe current, and convergence angle (α) of 28 mrad . Spectra were acquired using an
213 EELS entrance aperture of 2.5 mm , providing a collection angle (β) of 24 mrad . The energy dispersion
214 was set to 0.025 eV/ch and a drift tube offset of 440 eV , enabling acquisition of the Ti $L_{2,3}$ edge with an
215 energy range of $\sim 50 \text{ eV}$ and analysis of its ELNES. At this scale, samples are not beam sensitive and the

216 drift is negligible. Therefore, maps were acquired with a single frame but a large pixel time of 2 s for
217 core loss and 0.01 s for the low loss. Quantitative analysis was performed on summed spectra to
218 enhance the signal-to-noise (S/N) ratio. (2) For EELS large field-of-view analysis, we used a different
219 set of conditions because we wanted a quantifiable spectrum at each pixel. We used a condenser
220 aperture size of 35 μm and a probe current of 330 pA. We increased β to 63 mrad by using high-angle
221 EELS mode, which provides a shorter camera length than standard EELS mode. We also used a 5 mm
222 EELS entrance aperture and a dispersion of 0.5 eV/channel to increase the EELS S/N ratio. Spectral
223 images were acquired by averaging multiple passes (5 frames). A pixel time of 0.2 s for the core loss
224 was used and 0.001 s for the low loss. (3) Atomic-resolution EELS requires lower probe current and
225 shorter acquisition time to minimize the beam damage and the carbon deposition, respectively. Thus,
226 we used a condenser aperture of 30 μm and reduced the probe current to 150 pA. Further, we used
227 the liquid nitrogen cold trap on the HF5000 to limit the carbon deposition during beam rastering and
228 to decrease the sample drift. We used a large EELS spectrometer aperture (5.0 mm), the high-angle
229 EELS mode ($\beta = 63$ mrad), and the 0.5 eV/channel dispersion to ensure a high S/N ratio and short
230 acquisition time. To obtain EELS spectra from individual atomic columns on the hibonite grain from the
231 NWA 5028 meteorite, we oriented it along $[11\bar{2}0]$, with a goniometer tilt of $\alpha = 16.4^\circ$ and $\beta = -2.0^\circ$,
232 enabling analysis of the stacking along $[0001]$. The drift tube offset was set at 400 eV, and EELS maps
233 were acquired with a single frame, a pixel dwell time of 0.2 s for the core loss and 0.001 s for the low
234 loss. These atomic-resolution experiments limited our acquisition time and probe current, and so EDS
235 spectra could not be obtained at this scale of measurement.

236

237 **Data Processing**

238 Spectra were processed using personal Python scripts (available at:
239 <https://github.com/ZanettaPM/Ti-Oxidation-EELS-data-processing>) constructed using Hyperspy (de la

240 [Peña et al. 2021](#)). The energy position of the low-loss and high-loss spectra from different pixels were
 241 calibrated via zero-loss peak (ZLP) centering. The average energy resolution calculated from the full-
 242 width-half-maximum intensity of the ZLP over all standard spectra (experimental condition 1) is
 243 approximately 0.26 eV. The π^* peak of the C K-edge at 285 eV acquired with the same energy
 244 dispersion served as a calibration point. A shift of 1.7 eV is commonly observed at the π^* peak energy
 245 (after ZLP centering) which corresponds to a ~ 2.5 eV shift at the Ti $L_{2,3}$ edge energy. An inverse power
 246 law (AE^{-r}) model, where E is the energy loss and A and r are constants, was used to subtract the
 247 background (random plural and single-scattering contributions). **An energy window measuring 20 eV,**
 248 **placed between 430 eV and 450 eV (for a 0.025 eV/channel dispersion), was used to fit the**
 249 **background function. This range is located after potential ghost peak channels (due to the previous**
 250 **ZLP calibration) and at lower energy than possible Ti $L_{2,3}$ pre-edge peaks.**

251 The plural scattering contributions due to sample thickness were removed by Fourier-ratio
 252 deconvolution. We also removed the continuum beneath the white lines to isolate their intensities.
 253 There are varied methods for such removal, including a linear fit between edge onset and offset
 254 ([Garvie and Buseck 1998](#); [Zega et al. 2003](#)), but for the purposes of reproducibility and consistency
 255 with previous work ([Stoyanov et al. 2007](#)) we applied a double-step function. The onset and the offset
 256 refer to the position at which the energy rapidly decreases to a ground-state intensity before the first
 257 peak and after the last peak in the Ti $L_{2,3}$ edge respectively. The double-step function was initially
 258 implemented by [Van Aken and Liebscher \(2002\)](#) for the Fe $L_{2,3}$ edge and later modified by [Stoyanov et](#)
 259 [al. \(2007\)](#) for Ti in the form of:

260

$$261 \quad f(E) = h * \left(\arctan\left(\left(\frac{\pi}{w}\right) * (\Delta E - E1)\right) + \frac{\pi}{2}\right) + h * \left(\arctan\left(\left(\frac{\pi}{w}\right) * (\Delta E - E2)\right) + \frac{\pi}{2}\right) \quad (1)$$

262

263 where ΔE is the electron energy varying over a range of tens of eV; w represents the width of the
264 functions fixed to 2 eV; E_1 and E_2 are the inflection points fixed at 457.5 and 463.0 eV, respectively;
265 and h is the height of the individual arctan functions. In this work, h is a free parameter fit to the
266 spectrum just after the L_2 edge between 473 and 477 eV depending on the shape of the offset
267 [\(Giannini 2014\)](#).

268 EDS data were also processed using Hyperspy. We fit the spectra, i.e., background and peaks,
269 using a linear combination of the different components and a least square minimization method. The
270 model of the background and its implementation is described in [Zanetta et al. \(2019\)](#). Net peak counts
271 are given by the Gaussian areas which allows us to obtain elemental maps. Quantification was
272 achieved using the Cliff-Lorimer method [\(Cliff and Lorimer 1975\)](#) and an absorption-correction routine
273 developed by [Le Guillou et al. \(2018\)](#) and based on [Horita et al. \(1987\)](#). We used theoretical k-factors
274 provided by Oxford Instruments®. **Hyperspectral maps, measuring about $0.4 \mu\text{m}^2$ in area, with a pixel
275 size of ~ 0.5 nm, were acquired with a dwell time of $30 \mu\text{s}$ during 1h. These maps were then binned to
276 achieve a suitable S/N ratio, quantified, and recalculated as cation per formula unit (pfu). The first set
277 of maps described below is 160×160 pixels and are used to display the elemental distributions of the
278 cations. The second set of maps measure 10×10 pixels and are used to achieve a high number of
279 counts and plot elemental variations. Major elements like Al reach 50,000 counts, Ca, Ti and Mg are
280 around 80,000 counts while minor elements like Fe and Si reach 1000 counts per pixel. The high
281 number of counts, the accurate fitting of the spectrum, and the absorption-correction procedure,
282 which is particularly important to account for the thickness variation and the effect of heavy elements
283 on lighter elements, allow us to give confident errors on the quantified results (less than 3% on major
284 elements including Mg and Ti).**

285 Experimental HAADF images were compared to simulated images computed using the QSTEM
286 software, a multislice image-simulation code [\(Koch 2002\)](#). Two cases were investigated. We initially

287 simulated a nominal hibonite ($\text{CaAl}_{12}\text{O}_{19}$). Then, using the Supercell software (Okhotnikov et al. 2016),
288 we generated a hibonite solid solution of $\text{CaAl}_{10}\text{Ti}_1\text{Mg}_1\text{O}_{19}$ with Ti and Mg substituting on M4 sites and
289 M3 sites, respectively with an occupancy of 0.5. We also investigated the case $\text{CaAl}_{10}\text{Ti}_1\text{Mg}_1\text{O}_{19}$ with Ti
290 substituting between M2 and M4 sites. However, replicating the low concentration of Ti on the M2
291 site (<1 atom/unit cell for the M2 site, i.e., an occupancy of 0.5) is complex and requires a large
292 supercell. So, for simplicity, we assumed in our QSTEM simulation that the M2 site contains only Al,
293 and as discussed later, this assumption is valid (see fig. 4b). From this hibonite structure, we simulated
294 HAADF images to compare to our experimental HAADF images. We also added spherical aberration to
295 our simulations of end-members: $\text{CaAl}_{12}\text{O}_{19}$ and $\text{CaAl}_{10}\text{Ti}_1\text{Mg}_1\text{O}_{19}$, accounting for the A1, B1, and C3
296 components of the aberration function, e.g., Urban et al. (1999); Chang et al. (2006). The model
297 consists of a $60 \times 60 \times 30$ Å supercell. The scan window is 80×80 pixels with a resolution of 0.25 Å/pixel.
298 We fixed the number of slices to 21 with a slice thickness of 1.4286 Å.

299

300 Density Functional Theory

301 To understand the chemical shift and ELNES of our EELS spectra, we used density functional theory
302 (DFT) to simulate spectra. We computed the electronic band structure of the Ti-oxides by means of
303 the linearized augmented plane wave (LAPW) method, as implemented in the Wien2k package (Blaha
304 et al. 2020). Electronic structure calculations of various Ti-bearing compounds were then conducted
305 starting from experimentally reported crystal structures (Table 1). These structures are further relaxed
306 by employing both local spin density approximation (LSDA) and the generalized gradient approach
307 (GGA) (Perdew et al. 1996) exchange-correlation functionals. Both approaches are found to yield
308 similar EELS spectra. Initialization parameters and self-consistent field (SCF) calculation convergence
309 rules were set according to Hébert (2007). The energy to separate core and valence states were fixed
310 at -6 Rydberg (Ry; 1 Ry \approx 13.605 eV), except for FeTiO_3 and hibonite where values of -7 Ry and -8 Ry,

311 respectively, were adopted because of their atomic configurations. After structural relaxation, we
312 used an atomic sphere radius, i.e. muffin-tin radius (RMT), as large as possible but avoiding any
313 overlap. Within the RMT, the Wien2K code uses spherical harmonics, whereas in the interstitial region,
314 plane waves are instead used. Final RMT values range from 1.63 to 1.99 atomic units (a.u.) for the Ti
315 (Table 1). The matrix size RKmax ($R_{\text{mt}} * K_{\text{max}}$) was always fixed at 7.0, where K_{max} is the plane wave
316 cutoff and R_{mt} is the smallest atomic sphere. Spin-polarized calculations were performed for Ti_2O_3 ,
317 Ti_3O_5 , and Ti_4O_7 . Convergence criteria for the SCF cycle were fixed at 0.00001 Ry and 0.5 mRy/au for
318 the energy and the force respectively. After optimization of the structure, we proceeded to the next
319 iteration with higher k-mesh points (sampling points in the irreducible wedge of the first Brillouin zone
320 of the material) until the theoretical electron energy-loss near-edge spectra (TELNES) between two
321 iterations became nearly identical (peak positions differing by <0.1 eV). Final k-mesh sizes are
322 presented in Table 1.

323 The TELNES3 program implemented in Wien2k was used to model EELS spectra ([Jorissen 2007](#)).
324 Spectra were calculated using the same parameters as our experiments. We used a fixed splitting
325 energy of 5.5 eV between the L_3 and L_2 transitions and a branching ratio (intensity ratio between the L_2
326 and L_3 lines) of 0.8 ([Leapman et al. 1982](#); [Stoyanov et al. 2007](#)). We assumed no orientation
327 dependence and so we averaged our calculations over all possible directions of the scattering vector
328 with respect to the crystal. To improve the match between the model and the experimental results,
329 we used $2 \times 2 \times 2$ supercells. A full core-hole calculation for every species was achieved by removing one
330 core electron that was later added to the valence electrons. The spectral broadening, which is mostly
331 dependent on instrumental broadening, was always simulated with the same conditions, i.e., no
332 linearly energy dependent valence broadening and spectrometer broadening set at 0.6 eV
333 (experimentally determined). We kept the core-hole lifetime of the two edges as tabulated in the
334 TELNES3 program.

335 We calculated EELS hixonite spectra for two Ti oxidation states. We investigated two cases with
336 $Ti^{4+}/\Sigma Ti$ ratios of 1 and 0.5, respectively, and a composition of $CaAl_{10}Ti_1Mg_1O_{19}$, and $CaAl_9Ti_2Mg_1O_{19}$
337 respectively. We produced the structures using the Supercell program (Okhotnikov et al. 2016). For
338 the $Ti^{4+}/\Sigma Ti$ ratio of 1, we assumed that all the Ti occurs in the M4 site. For the ratio of 0.5, we
339 randomly distributed the Ti between the M2 and M4 site with a 1:1 ratio. Mg is set to occupy the M3
340 site.

341

342 RESULTS

343 Chemical shift calibration and white-line ratio

344 We acquired EELS spectra at the Ti $L_{2,3}$ edge for standards to develop a calibration curve relating
345 the white-line ratio to the $Ti^{4+}/\Sigma Ti$ ratio under the electron-optical conditions for our laboratory. Figure
346 1 shows the processed spectra normalized to the individual maxima acquired from Ti-bearing
347 reference materials (the absolute intensity variations are normalized). The spectra show a chemical
348 shift, marked by the edge onset, of 456.7 to 457.5 eV at the Ti $L_{2,3}$ edge that correlates with the
349 valence state of the material. We observed doublets (labeled a, b and c, d) at the L_3 and L_2 edges
350 similar to those reported by Stoyanov et al. (2007). The ELNES for these samples increases in
351 complexity from reduced Ti^{2+} in TiO to oxidized Ti^{4+} in TiO_2 . The spectrum of $CaTiO_3$, containing Ti^{4+} ,
352 shows four well-resolved broad peaks labeled a, b, c and d. In comparison, spectra from samples with
353 mixed oxidation state display secondary peaks convoluted with the major ones. As the Ti-oxidation
354 state decreases, peak intensity a and c decline in comparison to b and d peaks. The spectrum of TiO
355 contains only two major peaks and a low-intensity pre-peak a and c (Table S1). The energy positions of
356 the peaks (Table S2) are in agreement with previous measurements of Ti $L_{2,3}$ spectra of Ti-oxides
357 (Leapman et al. 1982; Brydson et al. 1987, 1989; Henderson et al. 2002; Stoyanov et al. 2007).

358 Hibonite samples (synthetic and natural) that contain a high $Ti^{4+}/\Sigma Ti$ ratio (>0.8) also show four
359 major peaks (a, b, c, and d) with secondary peaks on the b or the c peak. As shown in Fig. 2, the four
360 spectra display ELNES features similar to the Ti-oxide standards. A shift in energy is visible from 458.05
361 to 458.4 eV at the a peak position (Table S3).

362 Figure 3a shows the $I(L_2)/I(L_3)$ white-line intensity ratio as a function of Ti oxidation state for the
363 standard reference materials and the synthetic hibonites after removal of background and continuum
364 intensity and integration of 1 eV wide windows centered at energies of 456.3 and 465.75 eV (cf., Fig. 1
365 and 2). We obtained an exponential relationship between the $I(L_2)/I(L_3)$ and the $Ti^{4+}/\Sigma Ti$ ratios. Ti-oxide
366 standards and synthetic hibonites with high $Ti^{4+}/\Sigma Ti$ values (>0.8) display strong ($\pm 50\%$) $I(L_2)/I(L_3)$
367 variation (Fig. 3a). To investigate the effect of the second window position on the $I(L_2)/I(L_3)$ ratio, we
368 normalized all spectra to their individual maxima, and we plotted the value of the L_2 integration
369 window as a function of the $Ti^{4+}/\Sigma Ti$ ratio (Fig. 3b). The data show significant scatter in the integrated
370 intensity of the samples with a high $Ti^{4+}/\Sigma Ti$ ratio. We observe a general positive slope as a function of
371 increasing Ti-oxidation state, but the large scatter in the data precludes a strong correlation between
372 the white-line and $Ti^{4+}/\Sigma Ti$ ratios (Fig. 3a).

373

374 **Comparison of experimental spectrum and simulated spectra**

375 Given the complexities of the Ti $L_{2,3}$ ELNES, we performed first-principles calculations for the
376 reference oxides and hibonites based on previous experimentally determined structures. The goal of
377 these calculations is to verify the electronic-transition energies of the measured materials and to gain
378 insight into the underlying physics. The input structure and parameters for the TELNES 3 calculations
379 are presented in Table 1. To first order, the calculated spectra presented in Figure 4 match well to the
380 experimental data. We observe the same peaks a through d in the simulated spectra (solid lines),
381 giving reasonable 1:1 correspondence with experimental spectra (dashed lines). We observe that the

382 chemical shift, peak position, and width are reproduced. What differs between experimental and
383 simulated spectra is the peak heights. Even if the branching (L_3 to L_2) ratio of 0.8 is well reproduced
384 (Leapman et al. 1982), the ratio of the doublets (i.e., a, b and c, d) are not consistent in certain spectra.
385 In the experimental data, the peak a and c (corresponding to the $2t_{2g}$ level, see §4.1) are always less
386 intense than the peak b and d ($3e_g$ level). In comparison, most of the calculated spectra (Ti_2O_3 , Ti_4O_7 ,
387 $FeTiO_3$, TiO_2 and $CaTiO_3$) exhibit the opposite trend. The most significant difference between the
388 experimental and calculated spectra occurs for $CaTiO_3$. The calculated $CaTiO_3$ spectrum shows wider
389 peaks and a significant peak-height variation compared to the experimental spectrum.

390 The hibonite model spectra shows similar results to the standard calculated spectra. The chemical
391 shift is clearly visible in the calculated spectra for the two selected cases where $Ti^{4+}/\Sigma Ti=0.5$ and
392 $Ti^{4+}/\Sigma Ti=1$ (Fig. 4b, red and purple curves, respectively). Compared to these calculated spectra, the
393 experimental spectra with $Ti^{4+}/\Sigma Ti\sim 0.9$ (ALL-X samples) display an edge onset energy located between
394 these two endmembers (456.5 – 457.8 eV). Similar to the oxide standards, we find that the
395 experimental ratios between the peaks a and b, and c and d are not reproduced by the calculation (cf.,
396 solid and dashed curves in Fig. 4). If calculated and experimental spectra are compared in more detail,
397 the ELNES of the $Ti^{4+}/\Sigma Ti=1$ case where Ti is only located on the M4 site (purple curve) shows a close
398 match to the experimental spectra. In comparison, the model in which $Ti^{4+}/\Sigma Ti=0.5$ and Ti is equally
399 distributed between Al2 and Al4 sites (red curve) shows the presence of b'' and d'' peaks that are not
400 observed in the experimental spectra.

401 Regardless of the specific site occupancies and those effects on the ELNES, our TELNES calculations
402 show that the onset position of the Ti $L_{2,3}$ is predominantly dependent on the oxidation state.
403 However, the position of the offset appears to depend on both the chemical shift and other crystal-
404 field effects with peak position varying for similar $Ti^{4+}/\Sigma Ti$ values (e.g, peak d in $FeTiO_3$ vs TiO_2), which

405 is corroborated in the experimental data (cf., Figs. 3a,b). These observations required us to develop a
406 modified approach to quantify the $Ti^{4+}/\Sigma Ti$ ratio.

407

408 **Edge onset correlation and coupled EELS/EDS NWA 5028 hibonite analysis**

409 As the onset position is only dependent on oxidation state for the Ti-bearing materials
410 investigated in this study, we decided to explore its possible use for quantifying the $Ti^{4+}/\Sigma Ti$ ratio. Thus,
411 we quantified the onset intensity (all spectra are normalized to their individual maxima) of the L_3 edge
412 using a window of 2 eV ranging from 455 to 457 eV (Fig. 1 and 2. single window highlighted in blue) for
413 the Ti-oxides. **The window size and width were selected to give the best calibration (Fig. S3).** We find
414 that the L_3 integrated intensity decreases as a function of increasing oxidation state (Fig. 5). We fit the
415 data to a polynomial function, which yields a 0.99 correlation coefficient (Fig 5). The obtained
416 calibration was compared to the quantified $Ti^{4+}/\Sigma Ti$ ratios of previously synthesized hibonites (ALL
417 series) and this led to a close match (Fig.5). Based on scattering of the data points from the oxide
418 standards around the fitted curve, we estimate an absolute error of $\sim 1\%$ for the determination of the
419 $Ti^{4+}/\Sigma Ti$ ratios (dashed black curves, Fig. 5).

420 A view of the complete CTA CAI and the local area from which the section of NWA 5028 was
421 extracted is shown in Figure 6. **We extracted the hibonite grain in the rim of the CTA. The grain occurs**
422 **at the edge of the inner part of the rim layer (towards the core side of the CAI) with spinel and**
423 **perovskite and is surrounded by a mixture of melilite and diopside.** The hibonite grain contains up to 2
424 at% of Ti (8.3 wt% TiO_2) and Mg (2.4 wt% MgO), and low V 0.16 at % (0.56 wt% V_2O_3) (Table 2) **and**
425 **appears homogeneous in BSE contrast. Inclusions of spinel and perovskite are also observed in the**
426 **grain.** A large field-of-view STEM-HAADF image of the FIB section shows the hibonite grain and
427 surrounding context (Fig. 7a). The absolute thickness of the lower contrast zone is estimated to be <30
428 nm according to the method in [Lakoubovskii et al. \(2008\)](#). We oriented the Hib. 1 grain in Fig. 7a along

429 $[11\bar{2}0]$, enabling imaging along $[0001]$ (Fig. 7b). Analysis of an SAED pattern shows the 2.2 nm spacing
430 along the $[0001]$ direction (Fig. 7c), which appears in the lattice-fringe contrast of the HRTEM image
431 (Fig. 7b). The SAED pattern reveals sharp and discrete reflections indicating local long-range order,
432 free of stacking defects. However, stacking disorder (not shown) was observed in other locations. We
433 focused our study on the Hib. 1 hibonite grain in Fig. 7a, but measurements were also acquired from
434 the Hib. 2 hibonite grain for comparison. We applied the new calibration curve to the Hib. 1 grain (Fig.
435 5). We obtained a mean $Ti^{4+}/\Sigma Ti$ value of 0.86 ± 0.01 using the same acquisition procedure we applied
436 to the standard oxides and synthetic hibonites. This value is in the same range as the orange hibonite
437 from inclusion CG-11 of Allende or hibonite in the Blue Angel inclusion from Murchison (Beckett et al.
438 1988). This $Ti^{4+}/\Sigma Ti$ value is also comparable to those determined by Simon et al. (2009), Zega et al.
439 (2012), Giannini (2014), and Han et al. (2021) even though their measurements were not based on a
440 standard calibration.

441 In order to evaluate the homogeneity of the composition of the hibonite grain extracted from the
442 CTA CAI of the NWA 5028 CR2 carbonaceous chondrite, we acquired simultaneous EDS and EELS
443 spectra from the same area. We quantified each spectrum contained in every pixel of the EDS maps
444 (Fig. 7a, white-dashed box, labeled Map. Fig. 8). Figure 8 shows the elemental distribution per formula
445 unit (pfu) extracted from the X-ray lines present in the spectra of the map. The Ca map shows some
446 spatial variations, likely due to the thickness of the sample, but the magnitude of variation is low and
447 within error. In contrast, Ti and Mg exhibit significant spatial variations (0.65 ± 0.03 to 0.8 ± 0.04 cation
448 pfu) and show inverse spatial correlations with Al. We note that Ti is quantified based on the $K\alpha$ line
449 which is not convoluted with any other line.

450 To further assess the mechanism at the origin of the Ti incorporation and gain insight into cation
451 substitutions, we plotted four pertinent chemical fields based on quantified maps with the highest
452 number of counts (10x10 pixels and thousand counts per peak; Fig. 9). Previous studies indicated that

453 Ti can be incorporated into the structure either by direct substitution of Ti^{3+} for Al^{3+} or Ti^{4+} coupled
454 substitution with Mg^{2+} for two Al^{3+} , and therefore we focused on these three elements (Allen et al.
455 1978; Beckett et al. 1988; Doyle et al. 2014; Berry et al. 2017). If cations are normalized to their sum,
456 i.e. $\text{Al}+\text{Ca}+\text{Ti}+\text{Mg}+\text{V}+\text{Fe}+\text{Cr}=13$, we obtain values of $\text{Al}=10.5\pm 0.1$, $\text{Ca}=1\pm 0.02$ and $\text{O}=19\pm 0.5$.
457 $\text{Ti}+\text{Mg}+\text{V}+\text{Fe}+\text{Cr}$ make up the 1.5 pfu difference. Si counts were near the detection limit (see Table 2;
458 $\text{Si}=0.04$ cation pfu and Fig. S4). Ca is homogeneous with a value close to 1 cation pfu, even as Al varies
459 significantly. The Al concentration linearly decreases as $\text{Ti}+\text{Mg}$ increases; a strong correlation with a
460 slope ~ -1.02 and $R^2 = 0.9$ is observed (Fig. 9a). The Ti and Mg concentrations spatially correlate (Fig. 8)
461 but do not match perfectly (and anticorrelate with Al) with a range of 0.65 to 0.80 cations pfu (Fig. 9c).
462 The concentration of Mg is approximately equivalent to Ti on average, but a significant dispersion
463 around an ideal 1:1 correlation between Ti and Mg is observed (Fig. 9c). The Ca site shows a variation
464 of ± 0.02 . In comparison, Ti and Mg (or $\text{Ti}+\text{Si}$ and $\text{Mg}+\text{Fe}$) show a variation of ± 0.15 cation pfu. Fe, Si, Cr
465 and V are usually associated with the same substitution sites and can modify the relationship between
466 Al and the other cations. Since Cr and V are negligible (Fig. S4) we plotted the effect of Fe and Si on the
467 correlation (Fig. 9 d). Their low concentrations did not significantly affect the relationship (M2/M4
468 sites vs M3 site). We note that on average the concentration of Ti is approximately equivalent to Mg
469 and the $\text{Ti}+\text{Si}$ concentration is approximately equivalent to $\text{Fe}+\text{Mg}$ as shown by the microprobe bulk
470 measurement (Table 2). However, we emphasize that the nanoscale measurements revealed a
471 significant heterogeneity that was not evidenced by the lower scale microprobe measurements.

472 EELS spectral images were acquired with EDS maps, and so we evaluated the Ti $L_{2,3}$ edge acquired
473 over the same field of view. We quantified the chemical shift to obtain a $\text{Ti}^{4+}/\Sigma\text{Ti}$ ratio (Fig. 10) using
474 our onset calibration (Fig. 5). The ratio varies from 0.78 ± 0.04 to 0.93 ± 0.04 ; note that the errors on
475 these values are large due to the use of a smaller energy dispersion for this map (0.5 eV/channel vs
476 0.025 eV/channel). The map exhibits higher Ti^{3+} relative concentrations towards the grain boundary

477 (cf., Fig. 7a). In comparison, the EELS spectrum image (not shown) of the hibonite grain in the top left
478 corner of the FIB section (Fig. 7a) is homogeneous with a mean value of 0.95 ± 0.04 . We used the
479 $Ti^{4+}/\Sigma Ti$ EELS ratio for assessing the electroneutrality of the sample. The ideal charge of 19 O pfu is
480 subtracted from the charge of the cation sum, i.e., $Al^{3+} + Ti^{3+} + Ti^{4+} + Mg^{2+} + V^{3+} + Fe^{2+} + Cr^{3+} + Si^{4+}$. The
481 observed distribution of Ti^{3+} , Ti^{4+} and Mg^{2+} and the low concentrations of other solutes (Fe, Cr, V, Si)
482 does not yield to electroneutrality, even if errors on quantification and possible variations in oxidation
483 states for the other solutes are considered (Fig. S7).

484 To evaluate the crystal chemistry and the atomic-scale variation of the $Ti^{4+}/\Sigma Ti$ ratio, we
485 performed aberration-corrected STEM-HAADF imaging. Such imaging reveals atomic columns
486 arranged in horizontal planes along the c-axis (Fig. 11). The planes are characterized by a high-contrast
487 central row of atomic columns juxtaposed by slightly less intense atomic columns above and below
488 (Fig. 11b,c). The atomic columns form an echelon-like motif that is repeated vertically along [0001]
489 (Fig. 11b,c).

490 Hibonite is a member of the magnetoplumbite group (Holtstam and Hålenius 2020). Its structure
491 can be described as a sequence of spinel blocks (or S-blocks) interspersed with conductor layers (or R-
492 blocks), which are visible in Fig. 11d (Nagashima et al. 2010). The spinel block consists of the M1, M3,
493 and M5 sites giving a stoichiometry of Y_6O_8 where Y represents a small cation like Al (see Doyle et al.,
494 2014 for graphical representation). The R-Block contains large cations such as Ca along with the M2
495 and M4 octahedral sites, yielding an overall composition of AY_6O_{11} , where A represents a large cation
496 (Ca for instance). In hibonite, the S- and R-blocks alternate, hence the final formula is $AY_{12}O_{19}$. In the
497 model, the Ca atoms are shown in red and match the central atom of the R-block in the HAADF image
498 with the highest brightness (Fig. 11d). In this orientation (and in contrast to Han et al., 2021), Ca is
499 adjacent to the M2 and M4 sites, i.e., the light and dark blue spheres in the model that complete the
500 R-block (Fig. 11c, d, e, f, g). The M1 and M3 sites occur in the darkest areas of the HAADF image,

501 revealing clear separation of each echelon-like motif (Fig. 11 f, g). Finally, the M5 columns (green
502 spheres in the model) surround the R-block and are visible as bright columns. In this orientation [11-
503 20], every other M5 column is brighter due to a higher atomic occupancy. The relatively darker M5
504 columns adjacent to the bright M5 columns contain lower occupancy (50% lower in this direction).
505 Light elements such as O are generally not detectable with HAADF imaging (see [Carter and Williams,](#)
506 [2016](#)) and are therefore not visible on the image simulation (Fig. 11d, f). The simulation in Fig. 11g
507 closely matches the experimental HAADF image (Fig.11c), in particular, reproducing the ‘dumbbell’
508 configuration where Ti atoms substitute onto the two adjacent M4 columns (red ellipses). The
509 simulation of Mg substituting on the M3 site gives darker areas, reproducing the contrast observed in
510 the HAADF image (Fig. 11c and 11g). The Ti concentration within the M2 site in this local area is below
511 the detection limit.

512 We performed aberration-corrected STEM-EELS mapping of the local region of hibonite at its
513 boundary with perovskite to determine its atomic-scale composition (cf., Fig. 7a). Our focus here is on
514 Ti but because the Ca $L_{2,3}$ edge occurs at an energy close to that of Ti (346 eV and 456 eV,
515 respectively), our energy dispersion allows the acquisition of both the Ca $L_{2,3}$ and Ti $L_{2,3}$ edges. We
516 therefore mapped both cations. We note that the intensity of the Al L and K edges tend to be weak
517 and located at lower and higher energy losses, (78 and 1560 eV, respectively) than Ca $L_{2,3}$ and Ti $L_{2,3}$
518 and are therefore not represented here. The O atoms, which are distributed throughout the structure
519 are generally not detected with HAADF (although they can be observed using annular-bright-field
520 STEM) and can be challenging to resolve by EELS, and so are also not represented here. The STEM-
521 EELS mapping shows that the Ca columns are well defined (Fig.12b) and match well to the model with
522 atoms in the center of the R-block (Fig. 11c-g). All columns present relatively similar intensities
523 suggesting that their occupancy is similar over the sampled area. The Ti $L_{2,3}$ map reveals that it occurs
524 in the region of the M2 and the M4 sites adjacent to the Ca (Fig. 12c). The relative concentrations of Ti

525 in M2 and M4 are difficult to determine by EELS, but the high-intensity pixels are distributed around
526 the line defined by the Ca atoms, suggesting higher Ti concentration on the M4 site (Fig. 12c), as
527 shown by the HAADF image simulation (Fig. 11g). We applied our edge onset calibration to the Ti L_{2,3}
528 edge to determine the Ti⁴⁺/ΣTi ratio of this local area (Fig. 12d). The data show that the Ti⁴⁺/ΣTi ratio is
529 heterogeneous at the atomic scale with **potentially more** hotspots of higher Ti⁴⁺ on the center of the R
530 block **even if Ti³⁺ hotspots are also observed in the center of R-block in the bottom part of the map.**
531 We observe pure Ti⁴⁺ atomic columns but no pure Ti³⁺ columns.

532

533 DISCUSSION

534 Validity of the single-window method

535 In EELS, edges result from the transition of core electrons to unoccupied states above the Fermi
536 level. The observed peaks in the Ti-oxide standards can mostly be explained by four possible
537 ionizations. The interaction between the Ti 3d, 4s, and 4p atomic orbitals and oxygen 2s and 2p atomic
538 orbitals gives rise to the following molecular orbital levels: 1a_{1g}(σ), 1t_{1u}(σ), 1e_g(σ), 2a_{1g}(σ), 2t_{1u}(σ),
539 2e_g(σ), 1t_{2g}(π), 3t_{1u}(π), t_{2u}(π⁰), t_{1g}(π⁰), 2t_{2g}(π*), 3e_g(σ*), 3a_{1g}(σ*), 4t_{1u}(σ,π*) (Fischer 1970; Stoyanov et al.
540 2007). In all of the Ti-oxides measured here, the molecular orbitals are filled up to the t_{1g}(π⁰). The
541 dipole selection rules exclude the 4t_{1u}(σ, π*) as a possible final state, and the 3a_{1g}(σ*) level, at higher
542 energy, is a lower probability transition. However, evidence of secondary peaks at 472 and 477 eV
543 were observed in the TiO₂ spectrum that could correspond to 2p_{1/2},2p_{3/2} → 3a_{1g} transitions. The
544 number and intensity of the Ti L_{2,3} ELNES peaks is, therefore, mostly controlled by the 2p_{1/2},2p_{3/2} →
545 2t_{2g}(π*),3e_g(σ*) transitions and the degree of occupancy of the 2t_{2g} level (Fig.1 and Table S1; Stoyanov
546 et al. 2007).

547 In contrast to the oxide standards measured here, where Ti is restricted to one or two
548 crystallographically distinct octahedral sites, hibonite has three distinct octahedra, M1 (point

549 symmetry D3d), M4 (C3v) and M5 (Cs), a M3 tetrahedron (C3v), and the unusual fivefold-coordinated
550 trigonal bipyramid M2 (D3h). Previous work suggested that Ti mostly occupies the M4 site (Beckett et
551 al. 1988; Doyle et al. 2014, 2016; Ardit et al. 2016; Berry et al. 2017). Ti is therefore located in a site
552 with an octahedral coordination (except for low Ti concentration e.g., Berry et al., 2017) similar to the
553 Ti-oxide standards (Table 1). This similar Ti environment explains why ELNES of the Ti standards with
554 $Ti^{4+}/\Sigma Ti$ ratio=1 (TiO_2 , $CaTiO_3$, and $FeTiO_3$) and the hibonite spectra show similar peak doublets.

555 The quantized electronic transitions mainly control the observed peak positions, e.g., Fig. 4.
556 However, previous work showed that ELNES are also affected by other interactions. For instance,
557 distortion of the Ti polyhedra, depending on the material, can add complexity to the Ti $L_{2,3}$ ELNES
558 (Stoyanov et al. 2007). The peak width, which depends on the time it takes for the ionized electron to
559 decay to the ground state, can also vary according to the electronic environment (Egerton 1996).
560 Decoupling the portion of the chemical shift due to the oxidation state is therefore challenging. The
561 white-line approach has the advantage of tracking the shift in energy as a means to quantifying
562 oxidation-state ratios rather than precise fitting of the ELNES which is particularly challenging for early
563 3d metals that contain complex crystal-field effects superimposed on a chemical shift (Fischer 1970;
564 Leapman et al. 1982; De Groot et al. 1990; Brydson et al. 1993; Garvie and Buseck 1998; Stoyanov et
565 al. 2007). The white-line approach has been applied to 3d metals such as Fe (Van Aken et al. 1998; Van
566 Aken and Liebscher 2002) and Ti (Stoyanov et al. 2007). In the latter work, Stoyanov et al. (2007)
567 showed a relationship between the white-line intensity ratio (L_2/L_3) and the oxidation state of Ti. Thus,
568 we attempted a similar approach to obtain a calibration of the shift of the Ti $L_{2,3}$ edge as a function of
569 Ti oxidation state under the electron-optical conditions in our laboratory (Figure 1, 2, 3a). However,
570 because the Ti-oxide standards and synthetic hibonites with high $Ti^{4+}/\Sigma Ti$ values (>0.8) display large
571 ($\pm 50\%$) IL_2/IL_3 variations (Fig. 3a), the fit that we obtained is markedly different from the one reported
572 by Stoyanov et al. (2007). We attribute this difference to the position of the edge offset window (IL_2 :

573 465.25-466.25 eV; cf., Fig. 1 and Fig. 3b). For standards with similar $Ti^{4+}/\Sigma Ti$ values (>0.8), we note that
574 the L_2 integration window (465.25-466.25 eV) can occur on the left side of the d peak, as can be seen
575 for $FeTiO_3$ and TiO_2 standards or directly on the crest as in $CaTiO_3$ (Fig.1). Thus, this difference in
576 position will significantly impact the final L_2 intensities and hence the IL_2/IL_3 white-line ratio.
577 Moreover, our experimental results and DOS calculations demonstrate that the dependency of the
578 edge-offset position on other effects, e.g., electronic structure, does not relate to our experimental
579 microscope conditions (Fig. 4). These observations suggest that dependency of the white-line ratio on
580 both oxidation and crystal-field effects complicates the development of a universal curve for Ti.

581 Difficulty in reproducing the white-line ratio method for Ti was also noted by [Giannini \(2014\)](#). As
582 an alternative method, [Giannini \(2014\)](#) proposed using relative heights of the four peaks that occur in
583 hibonite spectra as a possible proxy for the oxidation state. To tackle the crystal-field dependency, we
584 first tried various methods that could relate the features present in the spectra to the oxidation state.
585 Spectral parameters that are related to $Ti^{4+}/\Sigma Ti$, but not to the site occupancy, distortion, or Ti content
586 would be ideal for a Ti-valence calibration curve. We therefore tested a variety of potential tracers for
587 the valence state including: the position of the d peak (Fig. 2), the doublet dissociation in energy, the
588 edge center energy (defined by the difference between the onset and the offset), the edge variance,
589 and the relative heights (as proposed by [Giannini \(2014\)](#)). We concluded however, that all of these
590 parameters depend on effects other than just the chemical shift. **The only alternative method leading**
591 **to a satisfactory calibration curve was obtained when taking the ratio of the peak d energy range**
592 **(464.5-468.5 eV) divided by the L_2 energy range (462.5-468.5) (Le Guillou et al. 2015). This method**
593 **leads to a larger dispersion around the calibration curve but might be considered as an alternative if**
594 **the S/N ratio of the acquisition is low (since it integrates energy ranges with higher intensities than the**
595 **single window approach).** The IL_3 onset window (455.8-456.8 eV) shows a more accurate correlation
596 with the Ti oxidation state. We therefore used the IL_3 onset window for our $Ti^{4+}/\Sigma Ti$ calibration.

597 However, the use of a wider window (455-457 eV) increases the final R^2 (Fig. 5) and reduces artifacts
598 that are background related (Fig. S3). We note that the almost linear relationship between the IL_3
599 intensity and the $Ti^{4+}/\Sigma Ti$ ratio is linked to the evolution of the width of the band gap for the various
600 oxidation states. For TiO , which shows metallic conductivity, the conduction and the valence bands
601 overlap, but for an insulator such as TiO_2 (or hironite), the band gap becomes larger and the electronic
602 screening poorer, leading to a shift to higher energy relative to metallic Ti.

603 As a test of the efficacy of the alternative method developed here, we find that the $Ti^{4+}/\Sigma Ti$ ratios
604 of the ALL sample series quantified with our approach (Fig. 5) are ALL2-6= 0.91 ± 0.01 , ALL2-
605 57= 0.88 ± 0.01 , and ALL2-55= 0.84 ± 0.01 . These values compare favorably with the corresponding ratios
606 of 0.95 ± 0.01 , 0.91 ± 0.01 , and 0.85 ± 0.01 , measured by [Beckett et al. \(1988\)](#) using electron spin
607 resonance (ESR) spectroscopy. The agreement of the data sets from these orthogonal approaches and
608 the lower data dispersion around the fitted curve in comparison to the previously discussed white-line
609 ratio method suggests that the alternative method provides a higher accuracy under our optical
610 conditions.

611

612 **Error estimation on the bulk $Ti^{4+}/\Sigma Ti$ ratio determination and mapping limitations**

613 The single-window method described above based on the edge-onset position requires that each
614 spectrum must first be normalized to its own maximum to remove the intensity variations due to the
615 sample thickness or Ti concentration. This normalization is possible because the d peak always
616 corresponds to the maximum value of the spectra in the studied materials. The use of only one
617 window in front of the edge potentially makes this method sensitive to the background noise
618 especially for samples with high $Ti^{4+}/\Sigma Ti$ ratio (>0.8). Such noise sensitivity does not apply in the two-
619 window method (e.g. [Stoyanov et al., \(2007\)](#)) because at least one window is placed at energies where
620 the signal/background (S/B) ratio is high ($S/B > 10$). In comparison, the edge-onset method described

621 here requires 1) a high S/B ratio ($S/B > 5$) to avoid any noisy spike that would impact the integrated
622 value and 2) correct removal of the background. The background should ideally fall to zero intensity
623 before the edge. To increase the reproducibility of $Ti^{4+}/\Sigma Ti$ quantification, we fixed the energy window
624 used for the background removal to a constant energy range and position (see method section).

625 For either the two-window method or our approach here, the calibration of the position of the
626 edge is essential. In our case, we fixed the π^* peak of the C, K edge at 285 eV for the standard
627 calibration. Keeping the same dispersion and acquiring the C edge of amorphous carbon immediately
628 after the Ti edge maps provided reproducible measurements of the Ti edge with shift variations < 0.04
629 eV between all the standard carbon π^* peak positions. This protocol resulted in a small shift of about 2
630 eV of the Ti edge to lower energy among all the standards (Table S2). In comparison, [Stoyanov et al.](#)
631 [\(2007\)](#) used a dispersion of 0.3 eV/channel for the carbon calibration step and a dispersion of 0.05
632 eV/channel for the Ti edge acquisition. This difference in choice of dispersion is partly responsible for
633 why we obtain a different exponential calibration curve shown in Fig. 3a in comparison to [Stoyanov et](#)
634 [al. \(2007\)](#). The data show that standards define an error of $\pm 1.1\%$ around the calibration curve for a
635 dispersion of 0.025 eV/channel (Fig. 5). The $Ti^{4+}/\Sigma Ti$ ratio is therefore well constrained for bulk
636 measurements. This error is approximately similar to the 10% error on the Ti^{3+} wt% value determined
637 by [Beckett et al. \(1988\)](#) for values contained between 0.8 to 1 $Ti^{4+}/\Sigma Ti$. For lower $Ti^{4+}/\Sigma Ti$ values, our
638 approach presents a higher accuracy than ESR measurements (if the Ti^{3+} wt% increases relatively to
639 Ti^{4+}).

640 We find that errors on the $Ti^{4+}/\Sigma Ti$ ratio are larger for nanoscale mapping than for the bulk values
641 (experimental condition 1 in §2.2), which is mostly related to the larger energy dispersion. The higher
642 probe current and collection angle increase the S/N ratio and enable correct removal of the
643 background intensity, which are, as we note above, are the main sources of uncertainties in this
644 method. The lower dispersion (0.5 eV/ch), however, gives lower spectral resolution and generates,

645 therefore, an inherently less accurate integration of the onset-position intensity. To determine the
646 accuracy of the $Ti^{4+}/\Sigma Ti$ ratio determination, we measured the Ti_3O_5 standard ($Ti^{4+}/\Sigma Ti$ ratio=0.5) with
647 two different dispersions, 0.025 and 0.5 eV/channel (noted as experimental conditions 1 and 2 in
648 §2.2). We estimate a difference in the $Ti^{4+}/\Sigma Ti$ ratio between these two dispersions of ± 0.04 , which
649 implies a relative error of $\pm 8\%$ for the Ti_3O_5 standard and a $\pm 5\%$ relative error for $Ti^{4+}/\Sigma Ti=0.86$ in the
650 NWA 5028 hibonite grain.

651 Atomic-scale measurements are more complex than the nanoscale measurements described
652 above because the sample is beam-sensitive and carbon deposition can occur for exposure times
653 $>0.2s$. These experimental limitations force short acquisition times, which gives a lower S/N ratio than
654 in the nanoscale maps. The background is therefore noisier, leading to larger errors in the $Ti^{4+}/\Sigma Ti$ ratio
655 determination. This error is added to the error due to lower energy dispersion (0.5 eV/ch). Even
656 though the pre-edge background can be strongly affected by the noise, the S/N ratio of the Ti $L_{2,3}$ edge
657 is still above the detection limit and the shift is easily resolved (e.g., Fig. S5). The range of $Ti^{4+}/\Sigma Ti$
658 obtained at the atomic level is consistent with bulk values obtained on the same samples. Based on
659 the noise level, we estimate an absolute error in atomic scale maps of ± 0.08 for the $Ti^{4+}/\Sigma Ti$
660 determination, which represents a relative error of $\pm 12\%$. The bulk measurement allows an accurate
661 quantification of the mean $Ti^{4+}/\Sigma Ti$ value of the grain whereas maps constrain variations in $Ti^{4+}/\Sigma Ti$
662 down to the atomic scale.

663

664 **Heterogeneities at the nanoscale**

665 The microprobe measurement (Table 2) of the hibonite that we extracted from the CAI in NWA
666 5028 gives a composition (Ca=1.0, Al=10.49 and Ti = 0.70 pfu and Mg \sim Ti) that is within the range of
667 previous measurements for meteoritic hibonites (e.g., [Keil and Fuchs 1971](#); [Allen et al. 1978](#);
668 [Armstrong et al. 1982](#); [MacPherson and Grossman 1984](#); [Ihinger and Stolper 1986](#); [Beckett et al. 1988](#);

669 Kööp et al. 2016), although it is Ti-rich (0.12 to 0.62 Ti pfu: Fig. S6 and Grossman 1975; Paque et al.
670 1987; Bischoff et al. 1993; Weber, D., & Bischoff 1997; Srinivasan et al. 2000; Lin et al. 2003; Sapah
671 2015). Other solutes such as Fe, Si, Cr or V occur in relatively low concentration (<0.05 pfu), which
672 simplifies the crystal chemistry of the hibonite in this CAI. However, hibonite grains in chondrites can
673 exhibit heterogeneous compositions at the nanometer scale (Doyle et al. 2016). Such variations reflect
674 the spatial and temporal evolution of the thermodynamic conditions, i.e., chemical potential,
675 temperature, and pressure of the system in which grains formed or last equilibrated. Our TEM data do
676 show that the hibonite chemistry is heterogeneous at the nanoscale, which is particularly clear in the
677 elemental maps for Ti, Mg and Al (Fig. 8 and 9). The plotted elemental compositions (Fig. 9) shows that
678 Ca has negligible variation, whereas Al and Ti+Mg are anticorrelated, suggesting that Ti and Mg are
679 only present on Al sites. We emphasize that the bulk sample exhibits approximately equal Mg and Ti
680 concentrations (Table 2), but that compositional heterogeneities occur at the nanoscale for these two
681 elements (Fig. 8 and 9c). The highlighting of such nanoscale heterogeneities could suggest that similar
682 nanoscale variations occur in other hibonite grains.

683 **Crystal chemistry and Ti substitution sites**

684 The crystal chemistry of hibonite solid solutions, including description of the site occupancies,
685 oxidation states of Mg, Ti, and other solutes is fundamental to the understanding of precise defect
686 reactions that have occurred during the formation and equilibration of the phase. Recent studies
687 showed that Ti mostly occupies the M4 site but that Ti^{4+} can also occupy the M2 site (Nagashima et al.
688 2010; Doyle et al. 2014; Berry et al. 2017; Asaduzzaman et al. 2021; Han et al. 2021). The Ti^{4+}
689 distribution between the two sites is dependent on the Ti concentration (Berry et al. 2017).

690 In our hibonite DFT calculations, we set the Ti to the M4 site or homogeneously distribute it
691 between the M2 site and the M4 site according to the literature (Doyle et al. 2014). Such relatively
692 simple site distributions facilitate investigation of the effect of the Ti occupancy on the ELNES. In our

693 calculations, the equal distribution of the Ti atoms on the M2 and M4 sites in hibonite gives a
694 spectrum containing groups of peaks equal in intensity, e.g., b and b' (or d and d') and b'' (or d'', see
695 Fig. 4b, red spectrum). These ELNES features are not representative of the experimental spectra likely
696 because of the too high concentration of Ti on the M2 site. Rather, a closest match between
697 experimental and simulated spectra, in terms of ELNES features, occurs where Ti occupies only the M4
698 site (%Ti⁴⁺=1 case; Fig. 4b, purple spectrum). Therefore, the ELNES modelled by our DFT calculations
699 confirm that Ti mostly occupies the M4 site and that Ti is more concentrated on the M4 site rather
700 than the M2 site, consistent with previous observations and computational work (Doyle et al. 2014;
701 Berry et al. 2017; Asaduzzaman et al. 2021).

702 In this study, the use of aberration corrected STEM coupled with image simulation and a
703 hyperspectral data-processing script developed in-house, allowed for the first time a direct
704 measurement of the Ti distribution between the M2 and M4 site in the hibonite structure. STEM-
705 HAADF images show brighter spots on the M4 site and the weaker intensity of the M3 sites. The image
706 simulations confirm that these features are due to the Ti and Mg substituting in M4 and M3 sites,
707 respectively (Fig. 11). We did not observe strong contrast on the M2 position of the HAADF image,
708 suggesting this site contains a low concentration of Ti. Al and Ca sites exhibit homogeneous intensities
709 similar to the simulations (Fig 11 c). Vacancies may occur but are under the HAADF simulation
710 detection limit (2 to 3 at%).

711 EELS spectrum imaging of the Ca L_{2,3} edge corroborates the STEM-HAADF data, i.e., homogeneous
712 intensity of the atomic columns, and suggests that there is no significant cation defect on the Ca site
713 (Fig 12 a, b). In comparison, the EELS spectrum image of the Ti L_{2,3} edge shows high intensity pixels
714 that are dispersed around the Ca site. This dispersion around the Ca rows confirms the HAADF
715 measurements and indicates that Ti mostly occupies the two adjacent face-sharing octahedral M4
716 sites (which appear as dumbbells in projection). It was proposed that this configuration is energetically

717 favored due to stabilization of the Ti-Ti interaction (Doyle et al. 2014; Asaduzzaman et al. 2021). In
 718 addition to the Ti substitution site determination, the data show that pure Ti^{4+} columns ($Ti^{4+}/\Sigma Ti=1$) are
 719 more abundant in the center of the row where the M2 sites are located (Fig. 12 d). Although the
 720 uncertainties on the $Ti^{4+}/\Sigma Ti$ ratio are larger at the atomic level than the nanoscale or bulk, the spatial
 721 distribution suggested by our STEM-EELS data indicate that if Ti^{4+} is distributed between the M2 and
 722 M4 sites, then Ti^{3+} mainly occupies the M4 site, which is consistent with previous work (Doyle et al.
 723 2014). The observations made at the atomic scale allow us to discuss the mechanism of incorporation
 724 which we discuss below.

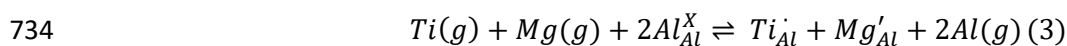
725

726 Mechanism of incorporation and Ti oxidation state

727 The observed crystal chemistry and the heterogeneities in conjunction with the knowledge of
 728 substitution mechanism(s) of solutes into the measured hibonites can shed light on the
 729 thermodynamic conditions that prevailed during condensation and subsequent alteration in the early
 730 solar nebula. Ti and Mg are the most concentrated solutes in chondritic hibonites (Brearley and Jones
 731 1998), and the two key substitution reactions hypothesized for their incorporation are:



733 and



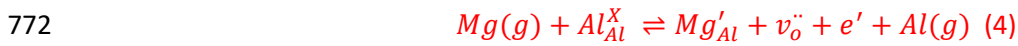
735 Where Al_{Al}^X represents an aluminum ion sitting on an aluminum lattice site, with neutral charge, Ti_{Al}^{\cdot}
 736 a titanium ion sitting on an aluminum lattice site, with a single positive charge (in comparison to the
 737 neutral charge) and Mg'_{Al} a magnesium ion sitting on an aluminum lattice site, with a single negative
 738 charge. Thus, coupling the analysis of the spatial distribution of Mg and Ti and its oxidation state is
 739 fundamental to testing the hypothesized substitution reactions in hibonite. Previous work showed
 740 that most meteoritic hibonite grains exhibit a nearly 1: 1 correlation of Mg:Ti (Allen et al. 1978;

741 [Armstrong et al. 1982](#); [Doyle et al. 2014](#); [Berry et al. 2017](#)). This well-known 1:1 Mg:Ti correlation led
742 previous workers to conclude that reaction (3) was the main pathway for Ti (and Mg) incorporation
743 ([Allen et al. 1978](#); [Armstrong et al. 1982](#); [Beckett et al. 1988](#); [Han et al. 2021](#)). The dispersion around
744 the 1:1 line (Fig. 9c) was also observed and attributed to a minor amount of Ti^{3+} being directly
745 incorporated through reaction (2) without Mg. Similarly, by plotting Si+Ti vs Fe+Mg, previous authors
746 questioned the incorporation mechanisms of Si and Fe (frequently present in the hibonite crystal
747 chemistry) and their impact on the 1:1 correlation ([Simon et al. 2006, 2019](#); [Han et al. 2015, 2021](#)).
748 Part of the dispersion around the 1:1 curve (e.g., see Fig. 11b of [Han et al. 2021](#)), not explained by
749 reaction (2) and (3), was therefore interpreted as being due to secondary substitution of Fe^{2+} for Mg^{2+}
750 and Si^{4+} for Ti^{4+} in the parent body settings.

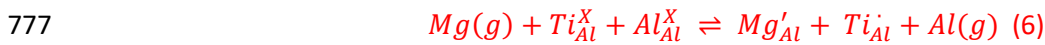
751 In our study of this particular hibonite grain, several lines of evidence cannot be explained by
752 reactions (2) and (3) as well as by the incorporation of Fe and Si and lead us to propose new
753 mechanisms of Ti and Mg incorporation into the hibonite structure. To be clear, we are not suggesting
754 that previously proposed mechanisms are not possible, but rather that they cannot explain the crystal
755 chemistry of the hibonite grain that we measure here. First, some points in Fig. 9c occur above the 1:1
756 correlation line and show that Mg is locally more concentrated than Ti which is unexpected if only
757 reaction (2) and (3) occur. Second, Fe and Si are in low concentrations, and so the magnitude of the
758 dispersion around the curve (Fig. 9d) cannot be explained by the substitution of these cations during a
759 secondary event as previously proposed [Simon et al. \(2006, 2019\)](#) and [Han et al. \(2015, 2021\)](#). Lastly,
760 the Ti oxidation state distribution of the NWA 5028 hibonite grain does not correlate with the Mg and
761 Ti distribution. If, as previously proposed in the literature, reaction (3) is predominant and the direct
762 substitution reaction (2) is responsible for the dispersion around the Ti:Mg 1:1 line, then the Ti
763 oxidation state should correlate with the Ti and Mg distribution. To highlight this discrepancy, we
764 calculated the excess of Mg (i.e., the ratio of Mg^{2+} relative to Ti^{4+} cations). Our data show that Mg is in

765 excess in most of the pixels, and that a significant amount of Mg is therefore not associated with Ti^{4+}
766 (Fig. 13). These data indicate that part of Mg has been introduced independently from Ti into the
767 structure and that a portion of Ti^{4+} was reduced to Ti^{3+} .

768 Based on the EDS nanoscale quantification (Figs. 8 and 9) and the comparative EDS and EELS data
769 (Fig. 13), we infer that additional reactions must be considered to explain both the Mg concentration
770 and the Ti oxidation state distribution. If Mg substitutes independently in the structure, an oxygen
771 vacancy is locally formed to ensure local charge neutrality.



774 (e.g. Kröger and Vink, 1956) where O_o represents an oxygen anion, $v_o^{\cdot\cdot}$ a doubly ionized oxygen
775 vacancy, and e^- a free electron. If Mg substitutes near a Ti^{3+} already present in the structure, then the
776 Ti is oxidized to Ti^{4+} :



778 Lastly, we showed that Ti^{4+} could also be reduced to Ti^{3+} (Fig. 13) by trapping the free electrons
779 originating from the formation of oxygen vacancies (5), i.e.,



781 In order to test the hypothesis that oxygen vacancies could occur and play a key role in dictating
782 the concentration of Ti^{3+} (and the distribution of Ti and Mg) in the structure, similar to the mechanism
783 originally proposed by Beckett et al. (1988), we compared our $Ti^{4+}/\Sigma Ti$ maps to the total charge of the
784 cation sum subtracted by 19 O pfu (see §3.3). As noted, electroneutrality was not obtained, and we
785 find that the charge difference matches our $Ti^{4+}/\Sigma Ti$ maps (Fig. S7). Based on quantification of the
786 electroneutrality from our EDS and EELS data, we estimate that oxygen vacancies represent 0.25 to 0.5
787 pfu of the grain (Fig. S7). An oxygen vacancy of 0.5 pfu represents 1/12 of the atoms on the O4
788 Wyckoff site (which is the closest site to the M3 where Mg substitute) and 1 oxygen atom per unit cell

789 (which contains 38 oxygen atoms). Several additional pieces of evidence support that the charge
790 difference is certainly due to O vacancies including: (1) neither Ca nor Al cation vacancies were
791 observed in the experimental HAADF images, which was confirmed by comparison to the calculated
792 images; (2) no abundant Ca vacancies were observed on the Ca L_{2,3} EELS spectrum image; (3) other
793 solutes (V, Cr, Fe) are in too low concentration to explain the charge difference; and (4) substitutions
794 (2), (3), or (6) are unlikely to explain the Ti⁴⁺/ΣTi distribution because the Mg/Ti and Ti⁴⁺/ΣTi spatial
795 distribution are not correlated (Fig. 13).

796 We conclude that multiple reactions are needed to correctly describe the crystal chemistry of this
797 specific hibonite grain including reactions producing oxygen vacancies. Therefore, the Ti oxidation
798 state distribution in this grain is not only controlled by the Mg/Ti ratio as proposed by (Berry et al.
799 2017). As showed by reaction (6), the sequence of occurrence of these reactions is also important
800 from the geological context and is discussed in detail in the next section. These multiples reactions
801 preclude direct connection of Ti⁴⁺/ΣTi to the *f*O₂ of the system. Instead, we suggest that the Ti (μ_{Ti}) and
802 Mg chemical potential (μ_{Mg}) as well as the *f*O₂ of the gas play an important role in the final Ti⁴⁺/ΣTi
803 ratio recorded by the grain. Under reducing conditions, the *f*O₂ of the gas might prevail over the μ_{Mg} ,
804 whereas in oxidizing environment, the μ_{Mg} could prevail over the *f*O₂.

805

806 Cosmochemical Implications

807 NWA 5028 is a CR2 chondrite, and therefore, is not expected to have experienced high-
808 temperature processing (thermal metamorphism with T > 400°C) on its parent body (Harju et al. 2014).
809 In contrast, evidence for parent body aqueous alteration in the form of Fe-silicates within veins in
810 spinel were observed in the chondrite (Ramprasad et al. 2018). However, we infer that such low-
811 temperature processes are not expected to modify significantly the Ti⁴⁺/ΣTi gradient or the total Ti/Mg
812 ratio in hibonite over the timescales inferred for parent-body processing because of the low Ti and Mg

813 diffusion rates (Brady and Cherniak 2010). Fe^{2+} could however exchange with Mg^{2+} and increase the
814 diffusion rate of the two cations but the Fe concentration in this hibonite is low (<0.04 pfu) suggesting
815 that Fe^{2+} did not replace a significant amount of Mg^{2+} (Simon et al. 2006, 2019). Thus, it is unlikely that
816 parent-body processing impacted the parameters of interest in this study, and so we explore nebular
817 processes below.

818 CAIs are classified into different types based on their mineralogy and morphology. Fluffy type-A
819 (FTA) CAIs are melilite-rich objects that contain highly irregular and nodular structures and are
820 believed to have been formed by gas-solid condensation in the early solar nebula. In comparison, CTAs
821 exhibit more spheroidal shapes and are thought to have undergone partial to complete melting and
822 recrystallization sometime after condensation but prior to incorporation into their parent bodies
823 (MacPherson and Grossman 1984; Simon et al. 1999). The CAI selected here was typed as a CTA
824 (Ramprasad et al. 2018). Therefore, at least two stages need to be considered as potential source of
825 the heterogeneity in the grain (Fig. 9c and d). The grain could have incorporated homogeneous
826 amounts of Ti and Mg that were later redistributed in the grain. Alternatively, the heterogeneity could
827 have been directly inherited from the gas phase during initial condensation of the grain. Lastly, both
828 scenarios could have occurred consecutively. We note that this hibonite grain that is at the boundary
829 of the Wark-Lovering (WL) rim (Fig. 6), exhibits a low concentration of Si (Table 2), which suggests that
830 this hibonite did not equilibrate with a silica-rich melt that might have formed from the secondary
831 event that modified the morphology of the CTA. The heterogeneous Al, Ti, and Mg concentrations
832 observed at the nanoscale (Fig. 8,9) as well as a $\text{Ti}^{4+}/\Sigma\text{Ti}$ gradient directed toward the grain boundary
833 (away from the capping layer Fig. 7, 10) indicate that the thermal event that led to the chemical,
834 structural, and morphological modification of the CAI was, locally, either too brief or at too low a
835 temperature to fully re-equilibrate this hibonite grain with surrounding material.

836 The complex history recorded by this hibonite grain is shown schematically in Fig. 14. We consider
837 two scenarios. In scenario 1, the heterogeneity is inherited during nebular equilibration, i.e., before
838 the transient thermal event. 1.a) we hypothesize that the hibonite grain is formed through
839 backreaction with previously condensed material, in accordance with thermodynamic predictions,
840 producing a nominal $\text{CaAl}_{12}\text{O}_{19}$ composition; 1.b) Ti is incorporated at high temperature through a
841 direct substitution (reaction 2). 1.c) Mg solubility in hibonite increases as the temperature decreases
842 (e.g., Lodders, 2003) and is added through multiple reactions. Equilibrium between the grain and the
843 gas was not achieved and an elemental gradient was recorded, i.e., the grain became zoned in Ti and
844 Mg and $\text{Ti}^{4+}/\Sigma\text{Ti}$. 1.d) a transient thermal event occurred, presumably in the solar nebula but prior to
845 accretion of the CAI in its parent body. This secondary event may have remodified the Ti, Mg, and
846 $\text{Ti}^{4+}/\Sigma\text{Ti}$ distribution. For instance, if the $f\text{O}_2$ was sufficiently low during the thermal processing,
847 formation of new oxygen vacancies (reaction 5) could have led to the reduction of Ti^{4+} to Ti^{3+} via
848 reaction (7).

849 In the second scenario, both 2.a) solid-gas interaction or 2.b) a direct condensation of molecular
850 species to form the hibonite grain could have led to a homogeneous composition. Ti and Mg are
851 incorporated simultaneously through a coupled substitution (reaction 3 above) at high temperature
852 into the hibonite structure. Indeed, Doyle et al. (2014) showed that a local Mg^{2+} and Ti^{4+} association in
853 the structure (replacing two nearest Al^{3+}) are energetically favored in hibonite rather than the
854 formation of isolated defects (i.e., dissociated Ti and Mg atoms). If Ti facilitates the incorporation of
855 Mg at temperature higher than its normal condensation temperature (according to thermodynamic
856 predictions, e.g., Lodders, 2003), then it is likely that the Mg^{2+} and Ti^{4+} association (i.e., the coupled
857 substitution reaction 3) will dominate. A small amount of direct substitution reaction (2) could have
858 occurred. At this stage, the Mg/Ti distribution matches the $\text{Ti}^{4+}/\Sigma\text{Ti}$ distribution and the 1:1 correlation
859 still occurs in the grain. 2.d) The heterogeneity is inherited from the stage 2. The transient thermal

860 event impacting the CTA modifies the distribution of Ti and Mg and oxygen vacancies are formed. The
861 $Ti^{4+}/\Sigma Ti$ is modified by the reaction (7) reducing Ti^{4+} present in the structure to Ti^{3+} . The 1:1 Mg:Ti
862 correlation is lost and the Ti and Mg distributions do not match the $Ti^{4+}/\Sigma Ti$ distribution.

863 It is difficult to conclude whether scenario 1 or 2 is the correct interpretation for the history of this
864 grain because thermodynamic models of Mg and Ti in hibonite are not available in the literature.
865 Therefore, thermodynamic equilibrium calculations only predict hibonite as pure Ca-Al-oxides.
866 Therefore, measurement of hibonite grains extracted from FTA CAIs and the development of a more
867 comprehensive thermodynamic model would be important steppingstones in understanding which
868 scenario occurred for this grain and what such defects can tell us about the conditions in which
869 hibonite formed or last equilibrated.

870

871 **Hibonite as nebular oxygen barometer?**

872 Hibonite is among one of the first several crystalline phases thermodynamically predicted to form
873 in a gas of solar composition (Yoneda and Grossman 1995; Ebel and Grossman 2000; Lodders 2003).
874 According to such models, corundum (Al_2O_3) which is calculated to condense first, can back react with
875 Ca (as atomic Ca or molecular CaO) in the nebular gas to form hibonite. If the hibonite grain
876 equilibrates with the gas, then the $Ti^{4+}/\Sigma Ti$ in hibonite should reflect the T, P, and fO_2 of the system. It
877 was proposed that under sufficiently oxidizing conditions, the $Ti^{4+}/\Sigma Ti$ in hibonite is linearly correlated
878 to the oxygen fugacity (fO_2) of the environment in which it formed (Beckett et al. 1988). This
879 relationship was established assuming that: 1) most of the Ti in hibonite is Ti^{4+} and incorporated
880 through the coupled substitution reaction (3) and 2) Ti^{4+} was reduced to Ti^{3+} by trapping free electrons
881 originating from the formation of oxygen vacancies (reactions 5 and 7). In their study, Beckett et al.,
882 (1988) investigated this relationship for specific hibonite compositions, i.e., with homogeneous Mg
883 concentrations and hence a fixed chemical Mg potential (μ_{Mg}). In comparison, Doyle et al. (2014) and

884 [Berry et al. \(2017\)](#), argued that the Ti^{3+} concentration in the hibonite structure is directly dependent
885 on the Mg activity in the gas (reaction 7) and that $\text{Ti}^{4+}/\Sigma\text{Ti}$ might be independent of the $f\text{O}_2$. This
886 scenario implies that in the absence of Mg, all Ti in hibonite must be Ti^{3+} . We note that in their studies
887 they investigated $f\text{O}_2$ conditions similar to those synthesized by [Beckett et al. \(1988\)](#) but on samples
888 with different Mg concentrations, i.e., variable μ_{Mg} . Thus, moving forward, we underline three
889 uncertainties that must be resolved for hibonite to be used as an oxybarometer.

890 First, the analysis of hibonite in the CTA from NWA 5028 reveals that the Mg activity played a key
891 role in the Ti oxidation state recorded by the hibonite grain. The final Mg concentration must
892 therefore be considered because the relationship between $\text{Ti}^{4+}/\Sigma\text{Ti}$ and $f\text{O}_2$ will depend on the
893 availability of Mg according to reaction (4). The synthesis of hibonite matching the compositions of
894 specific samples (BA and ALL samples) allowed [Beckett et al. \(1988\)](#) to determine a relationship for a
895 specific set of conditions and a fixed Mg chemical potential. Thus, understanding the relationship of
896 $\text{Ti}^{4+}/\Sigma\text{Ti}$ and $f\text{O}_2$ in other hibonite samples, with different compositions, requires knowledge of the a_{Mg} .

897 Another complexity in relating $\text{Ti}^{4+}/\Sigma\text{Ti}$ and the $f\text{O}_2$ is that numerous 3d metals can substitute into
898 the hibonite crystal, i.e., Fe, Cr, V ([Allen et al. 1978](#); [Beckett et al. 1988](#); [Bermanec et al. 1996](#);
899 [Rakotondrazafy et al. 1996](#); [Simon et al. 1997](#)). Of these, V can occur in relatively high concentration in
900 certain types of CAIs, e.g., the blue angel inclusion from Murchison that contains up to 1.8 wt% V_2O_3
901 ([Armstrong et al. 1982](#)). If, e.g., V^{3+} or V^{4+} compete with Ti for similar Al sites, the measured $\text{Ti}^{4+}/\Sigma\text{Ti}$
902 ratio alone will not be representative of the $f\text{O}_2$ of the material when it last equilibrated. Other
903 elements can also compete with Ti in meteoritic hibonites. Even if they occur in lower abundance than
904 V, the estimation of their concentration is also important to establishing the relationship between
905 $\text{Ti}^{4+}/\Sigma\text{Ti}$ and the $f\text{O}_2$.

906 In addition, the $f\text{O}_2$ variation as a function of temperature should be considered. For $\text{Ti}^{4+}/\Sigma\text{Ti}$ to be
907 useful in constraining redox conditions for natural hibonites, the temperature pathway experienced by

908 the grain would ideally be known. For example, the temperature of formation and hence fO_2 of a
909 hibonite grain extracted from an FTA CAI preserving primary signatures of condensation could be
910 estimated based on equilibrium thermodynamic predictions. However, the case of a CTA CAI, as
911 measured here, is more complex. On the one hand, it is likely that kinetics played an important role on
912 the recorded Ti-oxidation state during the brief and intense thermal processing that the CTA may have
913 experienced, precluding correlation of the $Ti^{4+}/\Sigma Ti$ ratio to the fO_2 without an appropriate kinetic
914 model. On the other hand, the elemental and the oxidation gradients could be used to determine the
915 time–temperature path associated with the diffusion process from profile modeling (Cuvillier et al.
916 2015). However, the temperature and the duration of thermal processing of this CTA CAI was not
917 estimated because it requires disentangling if the zonation inherited from growth during condensation
918 or because of diffusion in a subsequent event and is, therefore, beyond the scope of this paper.

919 Developing methods to quantify the nebular fugacity is challenging because the entire crystal
920 chemistry, including all possible crystal defects, must be known. A complete model considering the
921 parameters discussed above, e.g., μ_{Mg} , temperature history, the solutes competing with Ti, and the
922 reaction paths for Ti incorporation would give a correct estimation of the fO_2 of the gas in which the
923 grain formed or last equilibrated. Such a model will be the subject of a future paper.

924

925

CONCLUSIONS

926 We developed an EELS method to measure the $Ti^{4+}/\Sigma Ti$ ratio of oxide materials at various spatial
927 scales. Experimental data, supported by first-principles DFT calculations, confirm that use of the EELS
928 Ti $L_{2,3}$ edge onset is suitable to quantify Ti-oxidation states in heterogeneous materials. By coupling
929 STEM-EDS and -EELS and applying them to measurement of a hibonite grain from a CTA CAI extracted
930 from the NWA 5028 CR2 chondrite, we constrained the hibonite chemistry. The grain is zoned, with Al
931 and Ti anticorrelating, and Ti occurring as both Ti^{3+} and Ti^{4+} . Further, applying our developed

932 quantitative EELS method at the atomic scale, we find that the Ti^{3+} mainly occupies the M4 site, Ti^{4+} is
933 distributed between the M2 and M4 sites, and Mg occupies M3. From the crystal chemistry, we infer
934 that multiple reaction paths incorporated both Ti and Mg, and that coupled substitution is not the only
935 reaction incorporating these cations into the hibonite structure. The formation of oxygen vacancies in
936 a reducing nebular gas impacted the concentration of the reduced Ti. We conclude that the observed
937 zoning testifies to a complex history in which hibonite may have been witness to large changes in
938 nebular oxygen fugacity. However, the use of hibonite as an oxybarometer via measurement of its
939 $\text{Ti}^{4+}/\Sigma\text{Ti}$ ratio alone is made complicated by its crystal chemistry, the solutes that can compete with Ti,
940 and the varied reaction paths for Ti incorporation. We show that the μ_{Ti} , μ_{Mg} , and $f\text{O}_2$ of the system,
941 play an important role in the final $\text{Ti}^{4+}/\Sigma\text{Ti}$ ratio recorded by the grain. Depending on the redox
942 conditions of the system, the $f\text{O}_2$ or the μ_{Mg} could prevail. Thus, careful measurement of these
943 variables and consideration of the reaction paths are essential. An approach combining measurements
944 and modelling of the kind we report here could allow for more widespread use of hibonite (and other
945 phases) as direct probes of the thermodynamic landscape of the early solar nebula.

946

947

ACKNOWLEDGEMENTS

948 Research supported by the NASA Emerging Worlds (80NSSC19K0509) and Laboratory Analysis of
949 Returned Samples (80NSSC18K1475) Programs. We also thank Dr. Lindsay Keller for the Ti_4O_7 powder.
950 The DFT results are based upon High Performance Computing (HPC) resources supported by the
951 University of Arizona TRIF, UITS, and Research, Innovation, and Impact (RII) and maintained by the
952 UArizona Research Technologies department. We gratefully acknowledge NASA (grants #NNX12AL47G
953 and #NNX15AJ22G) and NSF (grant #1531243) for funding of the instrumentation in the Kuiper
954 Materials Imaging and Characterization Facility at the Lunar and Planetary Laboratory, University of

955 Arizona. We thank members of the Planetary Materials Research Group at LPL for helpful discussions.

956 P-M. Z. thanks Dr. Kenneth Domanik for his help with microprobe measurements.

957

958

959

REFERENCES CITED

- 960
- 961 Afir, A., Achour, M., and Saoula, N. (1999) X-ray diffraction study of Ti-O-C system at high temperature
962 and in a continuous vacuum. *Journal of Alloys and Compounds*, 288, 124–140.
- 963 Allen, J.M., Grossman, L., Davis, A.M., and Hutcheon, I.D. (1978) Mineralogy, textures and mode of
964 formation of a hibonite-bearing Allende inclusion. *Lunar and Planetary Science Conference*
965 *Proceedings*, 9, 1209–1233.
- 966 Amelin, Y., Connelly, J., Zartman, R.E., Chen, J.H., Göpel, C., and Neymark, L.A. (2009) Modern U-Pb
967 chronometry of meteorites: Advancing to higher time resolution reveals new problems.
968 *Geochimica et Cosmochimica Acta*, 73, 5212–5223.
- 969 Ardit, M., Borcănescu, S., Cruciani, G., Dondi, M., Lazău, I., Păcurariu, C., and Zanelli, C. (2016) Ni-Ti
970 Codoped Hibonite Ceramic Pigments by Combustion Synthesis: Crystal Structure and Optical
971 Properties. (J. McKittrick, Ed.) *Journal of the American Ceramic Society*, 99, 1749–1760.
- 972 Armstrong, J.T., Meeker, G.P., Huneke, J.C., and Wasserburg, G.J. (1982) The Blue Angel: I. The
973 mineralogy and petrogenesis of a hibonite inclusion from the Murchison meteorite. *Geochimica*
974 *et Cosmochimica Acta*, 46, 575–595.
- 975 Asaduzzaman, A., Muralidharan, K., and Zega, T.J. (2021) Density Functional Theory Driven Analysis of
976 the Interplay among Structure, Composition, and Oxidation State of Titanium in Hibonite, Spinel,
977 and Perovskite. *ACS Earth and Space Chemistry*, acsearthspacechem.0c00309.
- 978 Azaroff, L. V., and Pease, D.M. (1974) X-ray absorption spectra. *X-ray Spectroscopy*.
- 979 Beckett, J.R., Live, D., Tsay, F.D., Grossman, L., and Stolper, E. (1988) Ti³⁺ in meteoritic and synthetic
980 hibonite. *Geochimica et Cosmochimica Acta*, 52, 1479–1495.
- 981 Bermanec, V., Holtstam, D., Sturman, D., Criddle, A.J., Back, M.E., and Ščavničar, S. (1996) Nežilovite, a
982 new member of the magnetoplumbite group, and the crystal chemistry of magnetoplumbite and
983 hibonite. *Canadian Mineralogist*, 34, 1287–1297.

984 Berry, A.J., Schofield, P.F., Kravtsova, A.N., Miller, L.A., Stephen, N.R., Walker, A.M., Soldatov, A. V.,
985 Ireland, T.R., Geraki, K., and Mosselmans, J.F.W. (2017) The limitations of hibonite as a single-
986 mineral oxybarometer for early solar system processes. *Chemical Geology*, 466, 32–40.

987 Bischoff, A., Palme, H., Ash, R.D., Clayton, R.N., Schultz, L., Herpers, U., Stöfler, D., Grady, M.M.,
988 Pillinger, C.T., Spettel, B., and others (1993) Paired Renazzo-type (CR) carbonaceous chondrites
989 from the Sahara. *Geochimica et Cosmochimica Acta*, 57, 1587–1603.

990 Blaha, P., Schwarz, K., Tran, F., Laskowski, R., Madsen, G.K.H., and Marks, L.D. (2020) WIEN2k: An
991 APW+lo program for calculating the properties of solids. *Journal of Chemical Physics*, 152,
992 074101.

993 Brady, J.B., and Cherniak, D.J. (2010) Diffusion in Minerals: An Overview of Published Experimental
994 Diffusion Data. *Reviews in Mineralogy and Geochemistry*, 72, 899–920.

995 Brearley, A.J., and Jones, R.H. (1998) Chondritic meteorites. *Reviews in Mineralogy and Geochemistry*,
996 36, 3–398.

997 Brydson, R., Williams, B.G., Engel, W., Sauer, H., Zeitler, E., and Thomas, J.M. (1987) Electron energy-
998 loss spectroscopy (EELS) and the electronic structure of titanium dioxide. *Solid State*
999 *Communications*, 64, 609–612.

1000 Brydson, R., Sauer, H., Engel, W., Thomass, J.M., Zeitler, E., Kosugi, N., and Kuroda, H. (1989) Electron
1001 energy loss and x-ray absorption spectroscopy of rutile and anatase: A test of structural
1002 sensitivity. *Journal of Physics: Condensed Matter*, 1, 797–812.

1003 Brydson, R., Garvie, L.A.J., Craven, A.J., Sauer, H., Hofer, F., and Cressey, G. (1993) L_{2,3} edges of
1004 tetrahedrally coordinated d₀ transition-metal oxyanions XO₄ⁿ⁻. *Journal of Physics: Condensed*
1005 *Matter*, 5, 9379–9392.

1006 Cameron, A.G.W. (1962) Formation of the solar nebula. *Icarus*, 1, 339–342.

1007 Carter, C.B., and Williams, D.B. (2016) *Transmission Electron Microscopy: Diffraction, Imaging, and*

1008 Spectrometry, 1–518 p. (C.B. Carter & D.B. Williams, Eds.)Springer. Springer.

1009 Chang, L.Y., Kirkland, A.I., and Titchmarsh, J.M. (2006) On the importance of fifth-order spherical
1010 aberration for a fully corrected electron microscope. *Ultramicroscopy*, 106, 301–306.

1011 Chi, M., Ishii, H.A., Simon, S.B., Bradley, J.P., Dai, Z., Joswiak, D., Browning, N.D., and Matrajt, G. (2009)
1012 The origin of refractory minerals in comet 81P/Wild 2. *Geochimica et Cosmochimica Acta*, 73,
1013 7150–7161.

1014 Cliff, G., and Lorimer, G.W. (1975) The quantitative analysis of thin specimens. *Journal of Microscopy*,
1015 103, 203–207.

1016 Connelly, J.N., Bizzarro, M., Krot, A.N., Nordlund, Å., Wielandt, D., and Ivanova, M.A. (2012) The
1017 absolute chronology and thermal processing of solids in the solar protoplanetary disk. *Science*,
1018 338, 651–655.

1019 Connolly, H.C., and Burnett, D.S. (2003) On type B CAI formation: Experimental constraints on fO₂
1020 variations in spinel minor element partitioning and reequilibration effects. *Geochimica et*
1021 *Cosmochimica Acta*, 67, 4429–4434.

1022 Curien, H., Guillemin, C., Orcel, J.T., and Sternberg, M. (1956) La hibonite, nouvelle espèce minérale.
1023 *Comptes Rendus Hebdomadaires des Seances de l'Academie des Sciences*, 242, 2845–2847.

1024 Cuvillier, P., Leroux, H., Jacob, D., and Hirel, P. (2015) Fe-Mg interdiffusion profiles in rimmed forsterite
1025 grains in the Allende matrix: time–temperature constraints for the parent body metamorphism.
1026 *Meteoritics & Planetary Science*, 50, 1529–1545.

1027 De Groot, F.M.F., Fuggle, J.C., Thole, B.T., and Sawatzky, G.A. (1990) L q 3 x-ray-absorption edges of d
1028 compounds: K+, Ca²⁺, Sc³⁺, and Ti³⁺ in Oh (octahedral) symmetry, 15 p. *PHYSICAL REVIEW* Vol. 8.

1029 de la Peña, F., Prestat, E., Fauske, V.T., Burdet, P., Furnival, T., Jokubauskas, P., Nord, M., Ostasevicius,
1030 T., Lähnemann, J., MacArthur, K.E., and others (2021) hyperspy/hyperspy: Release v1.6.3.

1031 Doyle, P.M., Schofield, P.F., Berry, A.J., Walker, A.M., and Knight, K.S. (2014) Substitution of Ti³⁺ and

- 1032 Ti⁴⁺ in hibonite (CaAl₂O₉). *American Mineralogist*, 99, 1369–1382.
- 1033 Doyle, P.M., Berry, A.J., Schofield, P.F., and Mosselmans, J.F.W. (2016) The effect of site geometry, Ti
1034 content and Ti oxidation state on the Ti K-edge XANES spectrum of synthetic hibonite.
1035 *Geochimica et Cosmochimica Acta*, 187, 294–310.
- 1036 Ebel, D.S. (2006) *Condensation of Rocky Material in Astrophysical Environments IN: Meteorites and
1037 the Early Solar System* (ed. D.S. Lauretta and H.Y. McSween). University of Arizona Press, 253–
1038 277.
- 1039 Ebel, D.S., and Grossman, L. (2000) Condensation in dust-enriched systems. *Geochimica et
1040 Cosmochimica Acta*, 64, 339–366.
- 1041 Egerton, R.F. (1996) *Electron Energy-Loss Spectroscopy in the Electron Microscope*, 3rd editio.
1042 (Springer, Ed.)*Electron Energy-Loss Spectroscopy in the Electron Microscope*.
- 1043 Fischer, D.W. (1970) Molecular-Orbital Interpretation of the Soft X-Ray L II,III Emission and Absorption
1044 Spectra from Some Titanium and Vanadium Compounds ARTICLES YOU MAY BE INTERESTED IN
1045 Band Structure and the Titanium L II, III X-Ray Emission and Absorption Spectra from Pure.
1046 *Journal of Applied Physics*, 41, 3561.
- 1047 Garvie, L.A.J., and Buseck, P.R. (1998) Ratios of ferrous to ferric iron from nanometre-sized areas in
1048 minerals. *Nature*, 396, 667–670.
- 1049 Garvie, L.A.J., Craven, A.J., and Brydson, R. (1994) Use of electron-energy loss near-edge fine structure
1050 in the study of minerals. *American Mineralogist*, 79, 411–425.
- 1051 Giannini, M. (2014) The crystal chemistry of hibonite: an indicator for oxygen fugacity during Solar
1052 nebula condensation? Thesis.
- 1053 Grossman, L. (1972) Condensation in the primitive solar nebula. *Geochimica et Cosmochimica Acta*,
1054 36, 597–619.
- 1055 ——— (1975) Petrography and mineral chemistry of Ca-rich inclusions in the Allende meteorite.

1056 *Geochimica et Cosmochimica Acta*, 39, 433–454.

1057 Grossman, L., Beckett, J.R., Fedkin, A. V., Simon, S.B., and Ciesla, F.J. (2008) Redox conditions in the
1058 solar nebula: Observational, experimental, and theoretical constraints. *Reviews in Mineralogy*
1059 and *Geochemistry*, 68, 93–140.

1060 Han, J., Brearley, A.J., and Keller, L.P. (2015) Microstructural evidence for a disequilibrium
1061 condensation origin for hibonite-spinel inclusions in the ALHA77307 CO3.0 chondrite. *Meteoritics*
1062 & *Planetary Science*, 50, 2121–2136.

1063 Han, J., Ohnishi, I., Yasuhara, A., and Keller, L.P. (2021) Atomic-scale structure and non-stoichiometry
1064 of meteoritic hibonite: a transmission electron microscope study. *American Mineralogist*.

1065 Harju, E.R., Rubin, A.E., Ahn, I., Choi, B.-G.G., Ziegler, K., and Wasson, J.T. (2014) Progressive aqueous
1066 alteration of CR carbonaceous chondrites. *Geochimica et Cosmochimica Acta*, 139, 267–292.

1067 Hébert, C. (2007, January 1) Practical aspects of running the WIEN2k code for electron spectroscopy.
1068 Micron. Elsevier Ltd.

1069 Henderson, G.S., Liu, X., and Fleet, M.E. (2002) A Ti L-edge X-ray absorption study of Ti-silicate glasses.
1070 *Physics and Chemistry of Minerals*, 29, 32–42.

1071 Holtstam, D., and Hålenius, U. (2020a) Nomenclature of the magnetoplumbite group. *Mineralogical*
1072 *Magazine*, 84, 376–380.

1073 ——— (2020b) Nomenclature of the magnetoplumbite group. *Mineralogical Magazine*, 84, 376–380.

1074 Horita, Z., Sano, T., and Nemoto, M. (1987) Simplification of X-ray absorption correction in thin-sample
1075 quantitative microanalysis. *Ultramicroscopy*, 21, 271–276.

1076 Iakoubovskii, K., Mitsuishi, K., Nakayama, Y., and Furuya, K. (2008) Thickness measurements with
1077 electron energy loss spectroscopy. *Microscopy Research and Technique*, 71, 626–631.

1078 Ihinger, P.D., and Stolper, E. (1986) The color of meteoritic hibonite: an indicator of oxygen fugacity.
1079 *Earth and Planetary Science Letters*, 78, 67–79.

1080 Jorissen, K. (2007) The ab initio calculation of relativistic electron energy loss spectra. Ph. D. thesis.

1081 Keil, K., and Fuchs, L.H. (1971) Hibonite [Ca₂(Al, Ti)₂₄O₃₈] from the Leoville and Allende chondritic
1082 meteorites. *Earth and Planetary Science Letters*, 12, 184–190.

1083 Keller, L.P. (1995) TRANSMISSION ELECTRON MICROSCOPE STUDIES OF EXTRATERRESTRIAL
1084 MATERIALS. Final Technical Report for NASA Contract:NAS 9-18992.

1085 Keller, L.P., and Buseck, P.R. (1994) Twinning in meteoritic and synthetic perovskite. *American*
1086 *Mineralogist*, 79, 73–79.

1087 Koch, C. (2002) DETERMINATION OF CORE STRUCTURE PERIODICITY AND POINT DEFECT DENSITY
1088 ALONG DISLOCATIONS. Dissertation.

1089 Kööp, L., Nakashima, D., Heck, P.R., Kita, N.T., Tenner, T.J., Krot, A.N., Nagashima, K., Park, C., and
1090 Davis, A.M. (2016) New constraints on the relationship between ²⁶Al and oxygen, calcium, and
1091 titanium isotopic variation in the early Solar System from a multielement isotopic study of spinel-
1092 hibonite inclusions. *Geochimica et Cosmochimica Acta*, 184, 151–172.

1093 Kröger, F.A., and Vink, H.J. (1956) Relations between the Concentrations of Imperfections in Crystalline
1094 Solids. *Solid State Physics - Advances in Research and Applications*, 3, 307–435.

1095 Larimer, J.W. (1967) Chemical fractionations in meteorites-I. Condensation of the elements.
1096 *Geochimica et Cosmochimica Acta*, 31, 1215–1238.

1097 Le Guillou, C., Changela G., H., and Brearley, A.J. (2015) Widespread oxidized and hydrated amorphous
1098 silicates in CR chondrites matrices: Implications for alteration conditions and H₂ degassing of
1099 asteroids. *Earth and Planetary Science Letters*, 420, 162–173.

1100 Le Guillou, C., Leroux, H., Zanetta, P.M., Brearley, A.J., De La Pena, F., and Marinova, M. (2018) Water
1101 Content in Amorphous Silicates of Chondrite Matrices Determined by Advanced TEM Analysis---
1102 And Scanning Transmission X-Ray Microscopy. In *Lunar and Planetary Science Conference Vol.*
1103 49.

1104 Leapman, R.D., Grunes, L.A., and Fejes, P.L. (1982) Study of the L23 edges in the 3d transition metals
1105 and their oxides by electron-energy-loss spectroscopy with comparisons to theory. *Physical*
1106 *Review B*, 26, 614–635.

1107 Lewis, J.S. (1974) The temperature gradient in the solar nebula. *Science*, 186, 440–443.

1108 Lin, Y., Kimura, M., and Wang, D. (2003) Fassaites in compact type A Ca-Al-rich inclusions in the
1109 Ningqiang carbonaceous chondrite: Evidence for partial melting in the nebula. *Meteoritics and*
1110 *Planetary Science*, 38, 407–417.

1111 Lodders, K. (2003) Solar system abundances and condensation temperatures of the elements. *The*
1112 *Astrophysical Journal*, 591, 1220.

1113 Loehman, R.E., Rao, C.N.R., and Honig, J.M. (1969) Crystallography and defect chemistry of solid
1114 solutions of vanadium and titanium oxides. *Journal of Physical Chemistry*, 73, 1781–1784.

1115 Lord, H.C. (1965) Molecular equilibria and condensation in a solar nebula and cool stellar
1116 atmospheres. *Icarus*, 4, 279–288.

1117 MacPherson, G.J. (2014) Calcium–Aluminum–Rich Inclusions in Chondritic Meteorites. In *Treatise on*
1118 *Geochemistry Vol. 1*, pp. 139–179. Elsevier.

1119 MacPherson, G.J., and Grossman, L. (1984) “Fluffy” Type A Ca-, Al-rich inclusions in the Allende
1120 meteorite. *Geochimica et Cosmochimica Acta*, 48, 29–46.

1121 Moore, P.B., Sen Gupta, P.K., and Le Page, Y. (1989) Magnetoplumbite, $Pb^{2+}Fe^{3+}12O_{19}$: Refinement
1122 and Long-Pair Splitting. *American Mineralogist*, 74, 1186–1194.

1123 Muller, D.A., Fitting Kourkoutis, L., Murfitt, M., Song, J.H., Hwang, H.Y., Silcox, J., Dellby, N., and
1124 Krivanek, O.L. (2008) Atomic-scale chemical imaging of composition and bonding by aberration-
1125 corrected microscopy. *Science*, 319, 1073–1076.

1126 Nagashima, M., Armbruster, T., and Hainschwang, T. (2010) A temperature-dependent structure study
1127 of gem-quality hibonite from Myanmar. *Mineralogical Magazine*, 74, 871–885.

1128 Newnham, E.E., and Haan, Y.M. DE (2014) Refinement of the a Al_2O_3 , Ti_2O_3 , V_2O_3 and Cr_2O_3
1129 structures. *Zeitschrift für Kristallographie - Crystalline Materials*, 117, 235–237.

1130 Okhotnikov, K., Charpentier, T., and Cadars, S. (2016) Supercell program: A combinatorial structure-
1131 generation approach for the local-level modeling of atomic substitutions and partial occupancies
1132 in crystals. *Journal of Cheminformatics*, 8, 17.

1133 Onoda, M. (1998) Phase Transitions of Ti_3O_5 . *Journal of Solid State Chemistry*, 136, 67–73.

1134 Paque, J.M., Paque, and M., J. (1987) CaAl_4O_7 From Allende Type A Inclusion NMNH 4691. *LPI*, 18,
1135 762.

1136 Perdew, J.P., Burke, K., and Ernzerhof, M. (1996) Generalized gradient approximation made simple.
1137 *Physical Review Letters*, 77, 3865–3868.

1138 Rakotondrazafy, M.A.F., Moine, B., and Cuney, M. (1996) Mode of formation of hibonite ($\text{CaAl}_{12}\text{O}_{19}$)
1139 within the U-Th skarns from the granulites of S-E Madagascar. *Contributions to Mineralogy and*
1140 *Petrology*, 123, 190–201.

1141 Ramprasad, T., Mane, P., and Zega, T.J. (2018) Transmission Electron Microscope Analysis of a Spinel-
1142 Perovskite Assemblage Within a Refractory Inclusion from the Northwest Africa (NWA) 5028 CR2
1143 Chondrite. In *Lunar and Planetary Science Conference* p. No. 2083.

1144 Sapah, M.S. (2015) Characterization and chronology of refractory inclusions (CAIs) in the CV3
1145 chondrite NWA 4502.

1146 Schaffer, M., Schaffer, B., and Ramasse, Q. (2012) Sample preparation for atomic-resolution STEM at
1147 low voltages by FIB. *Ultramicroscopy*, 114, 62–71.

1148 Scott, E.R.D., and Krot, A.N. (2014) *Treatise on Geochemistry*, ed. AM Davis. Oxford: Elsevier.

1149 Shao, Y., Maunders, C., Rossouw, D., Kolodiaznyi, T., and Botton, G.A. (2010) Quantification of the Ti
1150 oxidation state in $\text{BaTi}_{1-x}\text{Nb}_x\text{O}_3$ compounds. *Ultramicroscopy*, 110, 1014–1019.

1151 Simon, Sutton, S.R., and Grossman (2009) First Ti-XANES analyses of refractory inclusions from

1152 Murchison. Lpsc, 60637, 1–2.

1153 Simon, S.B., Grossman, L., and Davis, A.M. (1991) Fassaite composition trends during crystallization of
1154 Allende Type B refractory inclusion melts. *Geochimica et Cosmochimica Acta*, 55, 2635–2655.

1155 ——— (1997) Multiple generations of hibonite in spinel-hibonite inclusions from Murchison.
1156 *Meteoritics and Planetary Science*, 32, 259–269.

1157 Simon, S.B., Davis, A.M., and Grossman, L. (1999) Origin of compact type A refractory inclusions from
1158 CV3 carbonaceous chondrites. *Geochimica et Cosmochimica Acta*, 63, 1233–1248.

1159 Simon, S.B., Grossman, L., Hutcheon, I.D., Phinney, D.L., Weber, P.K., and Fallon, S.J. (2006) Formation
1160 of spinel-, hibonite-rich inclusions found in CM2 carbonaceous chondrites. *American*
1161 *Mineralogist*, 91, 1675–1687.

1162 Simon, S.B., Krot, A.N., Nagashima, K., Kööp, L., and Davis, A.M. (2019) Condensate refractory
1163 inclusions from the CO3.00 chondrite Dominion Range 08006: Petrography, mineral chemistry,
1164 and isotopic compositions. *Geochimica et Cosmochimica Acta*, 246, 109–122.

1165 Smyth, J.R., Swope, R.J., and Pawley, A.R. (1995) H in rutile-type compounds: II. Crystal chemistry of Al
1166 substitution in H-bearing stishovite. *American Mineralogist*, 80, 454–456.

1167 Srinivasan, G., Huss, G.R., and Wasserburg, G.J. (2000) A petrographic, chemical, and isotopic study of
1168 calcium-aluminum-rich inclusions and aluminum-rich chondrules from the Axtell (CV3) chondrite.
1169 *Meteoritics and Planetary Science*, 35, 1333–1354.

1170 Stoyanov, E., Langenhorst, F., and Steinle-Neumann, G. (2007) The effect of valence state and site
1171 geometry on Ti L_{3,2} and O K electron energy-loss spectra of Ti_xO_y phases. *American*
1172 *Mineralogist*, 92, 577–586.

1173 Tan, H., Turner, S., Yücelen, E., Verbeeck, J., and Van Tendeloo, G. (2011) 2D Atomic Mapping of
1174 Oxidation States in Transition Metal Oxides by Scanning Transmission Electron Microscopy and
1175 Electron Energy-Loss Spectroscopy.

- 1176 Tan, H., Verbeeck, J., Abakumov, A., and Van Tendeloo, G. (2012) Oxidation state and chemical shift
1177 investigation in transition metal oxides by EELS. Ultramicroscopy.
- 1178 Urban, K., Kabius, B., Haider, M., and Rose, H. (1999) A way to higher resolution: spherical-aberration
1179 correction in a 200 kV transmission electron microscope, 821–826 p. *Journal of Electron*
1180 *Microscopy* Vol. 48.
- 1181 Van Aken, P.A., and Liebscher, B. (2002) Quantification of ferrous/ferric ratios in minerals: New
1182 evaluation schemes of Fe L23 electron energy-loss near-edge spectra. *Physics and Chemistry of*
1183 *Minerals*, 29, 188–200.
- 1184 Van Aken, P.A., Liebscher, B., and Styrsa, V.J. (1998) Quantitative determination of iron oxidation
1185 states in minerals using Fe L2,3-edge electron energy-loss near-edge structure spectroscopy.
1186 *Physics and Chemistry of Minerals*, 25, 323–327.
- 1187 Wark, D., and Boynton, W. V. (2001) The formation of rims on calcium-aluminum-rich inclusions: Step
1188 I-fsah heating. *Meteoritics and Planetary Science*, 36, 1135–1166.
- 1189 Weber, D., & Bischoff, A. (1997) Refractory inclusions in the CR chondrite Acfer 059 El Djouf 001:
1190 Petrology, chemical composition, and relationship to inclusion populations in other types of
1191 carbonaceous chondrites. *CHEMIE DER ERDE-GEOCHEMISTRY*, 57, 1–24.
- 1192 Wechsler, B.A., and Prewitt, C.T. (1984) Crystal structure of ilmenite (FeTiO₃) at high temperature and
1193 at high pressure. *American Mineralogist*, 69, 176–185.
- 1194 Yamanaka, T., Hirai, N., and Komatsu, Y. (2002) Structure change of Ca_{1-x}Sr_x TiO₃ perovskite with
1195 composition and pressure. *American Mineralogist*, 87, 1183–1189.
- 1196 Yoneda, S., and Grossman, L. (1995) Condensation of CaO–MgO–Al₂O₃–SiO₂ liquids from cosmic
1197 gases. *Geochimica et Cosmochimica Acta*, 59, 3413–3444.
- 1198 Zanetta, P.-M.P.-M., Le Guillou, C., Leroux, H., Zanda, B., Hewins, R.H.H., Lewin, E., and Pont, S. (2019)
1199 Modal abundance, density and chemistry of micrometer-sized assemblages by advanced electron

1200 microscopy: Application to chondrites. *Chemical Geology*, 514, 27–41.

1201 Zega, T., Nittler, L.R., Stroud, R.M., Division, T., and Berkeley, L. (2012) Measurement of the oxidation
1202 state of Ti in solar and presolar hibonite. *Lunar and Planetary Science 43rd*, 9, 4–5.

1203 Zega, T.J., Garvie, L.A.J., and Buseck, P.R. (2003) Nanometer-scale measurements of iron oxidation
1204 states of cronstedtite from primitive meteorites. *American Mineralogist*, 88, 1169–1172.

1205 Zega, T.J., Nittler, L.R., Busemann, H., Hoppe, P., and Stroud, R.M. (2007) Coordinated isotopic and
1206 mineralogic analyses of planetary materials enabled by in situ lift-out with a focused ion beam
1207 scanning electron microscope. *Meteoritics and Planetary Science*, 42, 1373–1386.

1208 Zega, T.J., Haenecour, P., and Floss, C. (2020) An in situ investigation on the origins and processing of
1209 circumstellar oxide and silicate grains in carbonaceous chondrites. *Meteoritics and Planetary
1210 Science*, 55, 1207–1227.

1211 Zega, T.J., Manga, V.R., Ciesla, F., Muralidharan, K., Watanabe, K., and Inada, H. (2021) Atomic-scale
1212 Evidence for Open-system Thermodynamics in the Early Solar Nebula. *The Planetary Science
1213 Journal*, 2, 115.

1214

1215

1216

Standard	Ti ⁴⁺ /ΣTi ratio	Space group	Ti Symmetry	RMT Ti a.u.	RMT O a.u.	RKMax (R _{mt} * K _{max})	Energy threshold (Ry)	Final Kmesh points	Final Kmesh point for supercell	Initial cif file
TiO ₂	1	P4 ₂ /mnm	D _{2h}	1.82	1.65	7	-6	2000	100	(Smyth et al. 1995)
CaTiO ₃	1	Pmna	C _i	1.94	1.76	7	-6	200	10	(Yamanaka et al. 2002)
FeTiO ₃	1	R-3C	C _{3i}	1.99	1.77	7	-7	500	10	(Wechsler and Prewitt 1984)
Ti ₄ O ₇	0.7	P-1	C ₁	1.74	1.57	7	-6	100	6	(Afir et al. 1999)
Ti ₃ O ₅	0.5	C2/m	C _s	1.63	1.48	7	-6	100	5	(Onoda 1998)
Ti ₂ O ₃	0	R3cH	C _{3i}	1.71	1.55	7	-6	100	10	(Newnham and Haan 2014)
TiO	(2+)	Fm-3m	O _h	1.96	1.77	7	-6	1000	100	(Loehman et al. 1969)
Hibonite	0.5 - 1	P6 ₃ /mmc	C _{3v} and D _{3h}	1.74	1.63	7	-8	10	3	(Moore et al. 1989; Doyle et al. 2014)

1217 *Table 1: DOS parameters for the SCF calculation and optimization of the different species. Space group shown in Hermann-Mauguin notation;*
1218 *Ti symmetry shown in Schoenflies notation. RMT: muffin-tin radius, corresponding to the non-overlapping largest-atomic spheres in a spherically*
1219 *symmetric potential approximation. Ry; 1 Ry ≈ 13.605 eV. Kmesh point = sampling points in the irreducible wedge of the first Brillouin zone of the*
1220 *material. See text for more details. Visualization of the structures is presented in Fig. S2*

1221

1222

1223

1224

1225

<i>Elements</i>	<i>Wt%</i>	<i>At%</i>	<i>1 σ</i>	<i>pfu</i>
<i>Mg</i>	2.44	2.12	0.07	0.68
<i>Si</i>	0.16	0.12	0.02	0.04
<i>Al</i>	41.95	32.79	0.59	10.49
<i>Cr</i>	0.04	0.02	0.01	0.01
<i>Ca</i>	5.98	3.14	0.10	1.00
<i>Fe</i>	0.10	0.04	0.05	0.01
<i>Ti</i>	4.99	2.20	0.08	0.70
<i>K</i>	0.01	0.00	0.01	0.00
<i>Mn</i>	0.00	0.00	0.00	0.00
<i>V</i>	0.38	0.16	0.06	0.05
<i>Na</i>	0.00	0.01	0.02	0.00
<i>P</i>	0.01	0.00	0.02	0.00
<i>Cl</i>	0.00	0.00	0.00	0.00
<i>O</i>	45.06	59.40		19.00
<i>Total</i>	101.11	100.00	Sum cations	12.99

1226

1227 *Table 2: Composition of the hibonite grain as measured via EPMA before FIB sampling. Composition given in weight percent (Wt%) and*
 1228 *atomic percent (at%) and in cation per formula unit (pfu) based on 19 O atoms.*

1229

Figure 1: Stack of ELNES spectra of the Ti-bearing oxides. Two sets of data were processed and averaged for each sample. Spectra are ordered according to their $Ti^{4+}/\Sigma Ti$ ratio. White line integration windows defined by Stoyanov et al, (2007) are indicated in red (i.e. L_3 and L_2 windows). The boundaries of the single integration window for the edge onset method presented in this work are indicated in blue. See text for discussion of window width and placement. Peak positions are given in Table S2.

Figure 2: ELNES spectra of the synthetic (ALL series) and natural (NWA 5028) hibonite stacked in order of increasing $Ti^{4+}/\Sigma Ti$ ratio. Two sets of data were processed and averaged for each sample. White line integration windows defined by Stoyanov et al. (2007) are indicated in red (i.e. L_3 and L_2 windows). The single integration window for the edge onset method presented in this work is indicated in blue. Peak positions are given in Table S3.

Figure 3: The white-line ratio shown as a function of Ti oxidation state. a) Application of the white-line ratio method using the window positions and the background subtraction method detailed in Stoyanov et al, (2007). Both Ti-bearing oxides (blue crosses) and synthetic hibonites (red circles) are plotted. The fitted curve formula is given in the top left corner of the graphic. b) The L_2 edge intensity (after normalization; see text for details) plotted as a function of $Ti^{4+}/\Sigma Ti$. Both Ti-bearing oxides (blue crosses) and synthetic hibonites (red circles) are plotted. Large variations are revealed for samples with similar $Ti^{4+}/\Sigma Ti$ close to 1 (i.e., $CaTiO_3$, TiO_2 , $FeTiO_3$ and synthetic hibonites).

Figure 4: ELNES from experimental (dashed curves) measurements and DFT calculations (solid curves). a) TELNES (DOS + Broadening) calculation of the previously listed Ti-bearing oxide standards compared to their experimental spectra. b) TELNES (DOS + Broadening) calculation of two hibonite structures with distinct Ti oxidation states (as indicated, $\%Ti^{4+}=0.5-1$) compared to the synthetic hibonite experimental spectra. All spectra are normalized to their maxima. In the $\%Ti^{4+}=1$ case, Ti substitutes on the M4 site; in the $\%Ti^{4+}=0.5$ case, Ti is distributed over the M2 and M4 sites.

Figure 5: The normalized L_3 intensity, single window as shown in Figs. 1 and 2, as a function of the Ti^{4+} concentration. Synthetic hibonite with known Ti^{4+}/Ti^{3+} falls on the same correlation line. Blue crosses are Ti-bearing oxide standards. Red circles are the synthetic hibonite samples from Beckett et al. (1988). The red line corresponds to the quadratic expression fit to the data (equation shown at top). Dashed black curves represents the error dispersion. This correlation enables determination of the $Ti^{4+}/\Sigma Ti$ ratio (0.86 ± 0.01) of the hibonite grain sampled in NWA 5028.

Figure 6. Microprobe data on a CTA CAI from the NWA 5028 CR2 chondrite. a) Backscattered electron (BSE) image of the CTA CAI showing where the hibonite grain was extracted (orange rectangle). The region of interest is located at the edge of a dark (in BSE contrast) rim that surrounds the CTA (e.g., Ramprasad et al., 2018). b) BSE image of the RS2 area (e.g., Ramprasad et al., 2018) showing the hibonite grain (indicated by orange arrow and outlined with a white dotted curve). The grain exhibits sharp boundaries indicated by a dashed white curve. c) Higher magnification BSE image of the hibonite grain. Surrounding phases are identified. The red rectangle represents the extracted material.

Figure 7: Aberration-corrected STEM and diffraction data on hibonite extracted from NWA 5028. a) Low magnification HAADF - STEM image showing hibonite grains and adjacent perovskite. Areas from which diffraction and image data were acquired are indicated. b) Higher magnification HAADF - STEM image revealing lattice fringes of the oriented hibonite. c) SAED pattern of hibonite from NWA 5028, viewed down the $[11\bar{2}0]$ zone axis. Measurement of the pattern along the vertical direction reveals an interplanar spacing of 2.2 nm consistent with the c-axis of hibonite.

Figure 8: Quantified element maps acquired by TEM-EDS and presented in cation pfu (160×160 pixels). This dataset was acquired from the region shown in Figure 7a. Only major elements are plotted.

Figure 9: Quantification of the STEM-EDS data for hibonite grain 1 (hib.1 - see Fig.7a). Composition shown per formula unit assuming $Al+Ca+Mg+Ti+Si+Fe+V+Cr=13$. Each point represents a quantified pixel of the rebinned EDS map (10×10 pixels).

Figure 10: a) A map (40×40 pixels) of the $Ti^{4+}/\Sigma Ti$ ratio from hibonite grain 1 (hib.1 - see Fig.7a) determined using EELS by the edge-onset method. $Ti^{4+}/\Sigma Ti$ decreases from the interior (higher in the panel) to the grain boundary at the bottom. b) The chemical shift of the Ti $L_{2,3}$ edge (before double-step function removal) visible between the boundary of the grain (bottom part of the image) and the core.

Figure 11: a) Atomic-resolution STEM-HAADF data from hibonite grain boundary (see Figure 7a). b) HAADF image showing the location of atomic-scale measurements (Fig. 12). Atomic columns are visible in this $[11\bar{2}0]$ projection. The map is acquired near the grain boundary. c) High-contrast HAADF image showing the presence of brighter spots on the face sharing M4 sites and weak contrast on the M3 sites. Orange ellipses show? d) image simulations (QSTEM[®]) of a nominal hibonite compared to a model in the same orientation $[11\bar{2}0]$. The model shows 1:1 correspondence with the atomic position visible on the HAADF image and in the simulation. e) Image simulation of a nominal hibonite with aberrations. f) image simulation of hibonite containing 0.7 pfu of Ti and Mg substituting on M4 site and M3 site respectively. A model in the same orientation is compared. The white ellipses circle the site of Ti substitution (M4) g) Image simulation of the same hibonite (0.7 pfu of Ti/Mg) with aberrations. The orange ellipses show the replica of the brighter spot. The space between the blocks are darker than in e) due to the lower Z value as a result of Mg substituting into the M3 site.

Figure 12: Atomic-resolution EELS mapping of the local area shown by the red box in Fig. 11b in the $[11\bar{2}0]$ orientation. (a) HAADF reference image. (b) Ca $L_{2,3}$ atomic-resolution EELS map. (c) Ti $L_{2,3}$ atomic-resolution EELS map. (d) $Ti^{4+}/\Sigma Ti$ map. We masked the pixels containing low Ti $L_{2,3}$ intensity to better reveal the relationship with the Ti columns and the $Ti^{4+}/\Sigma Ti$ ratio. The map exhibits variation of Ti^{4+}/Ti^{3+} of 0.4 with an error of ± 0.08 .

Figure 13: Mg_{Excess} in cation per formula unit (Mg/Ti^{4+}) compared to the $Ti^{4+}/\Sigma Ti$ ratio determined by our single window approach in a hibonite grain of NWA5028. The superimposed orange arrows in the plot correspond to reaction 5 (vertical arrow) and to the reaction 8 (diagonal arrow). The vertical only impacts the Mg concentration, whereas the diagonal line corresponds to Ti^{3+} replacing Ti^{4+} and increasing the isolated Mg defect. The horizontal dashed line corresponds to $Mg=Ti$ or an ideal 1:1 correlation between Mg^{2+} and Ti^{4+} . Error bars are plotted according to the EDS quantification accuracy and the error discussed in section 4.2.

Figure 14: Schematic of the formation and evolution of the hibonite grain selected near the rim of the CTA CAI. Two pathways 1 and 2 are considered, with each consisting of formation and equilibration stages 1 and 2, respectively in the solar protoplanetary disk. See the text for discussion. Ultimately, the grain did not reach equilibrium and contains an element and Ti-oxidation-state gradient. The direction of the $Ti^{4+}/\Sigma Ti$ gradient is different from the direction of the elemental gradient (orange arrows vs white/blue arrows in the bottom row).

Figure 1

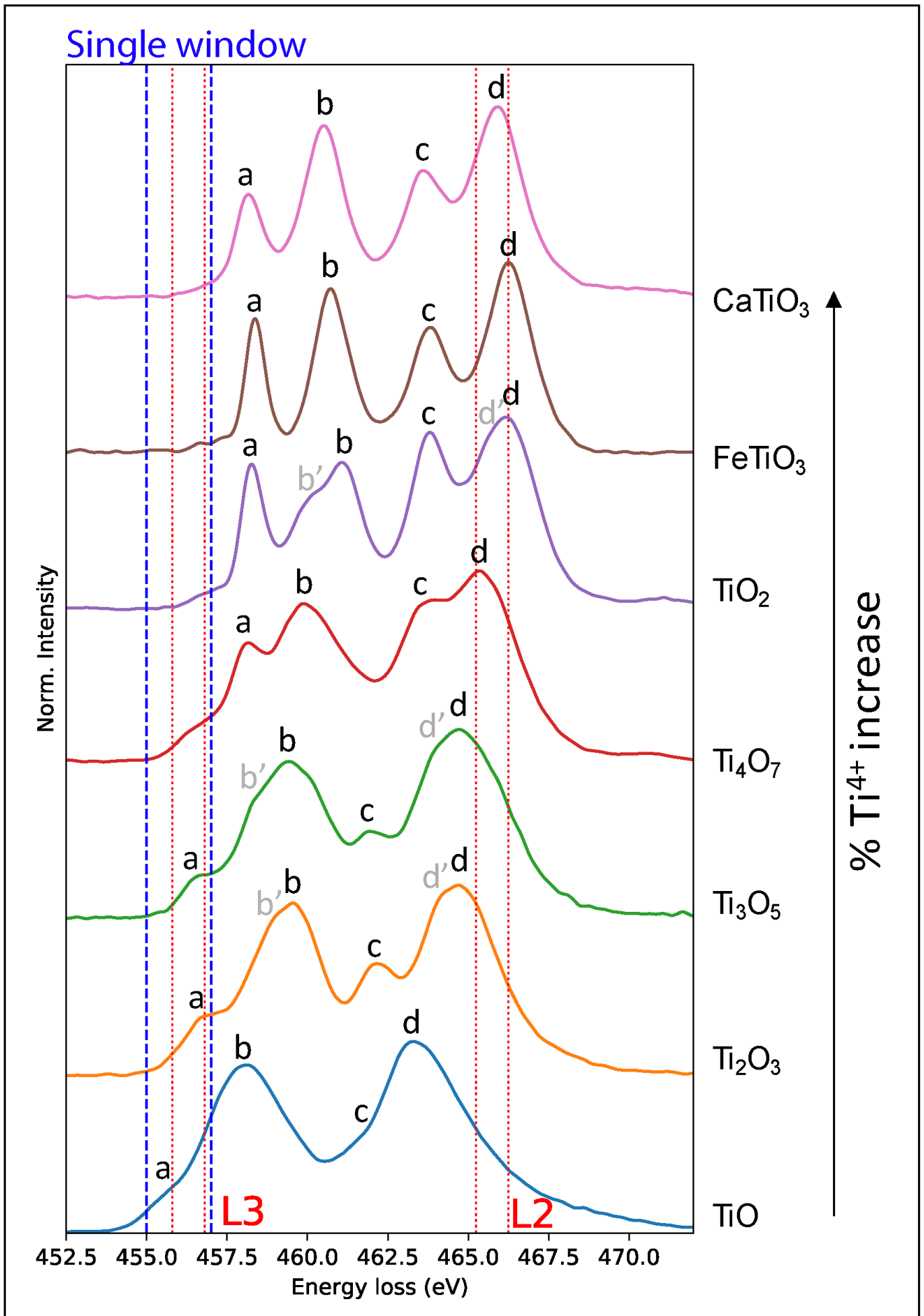


Figure 2

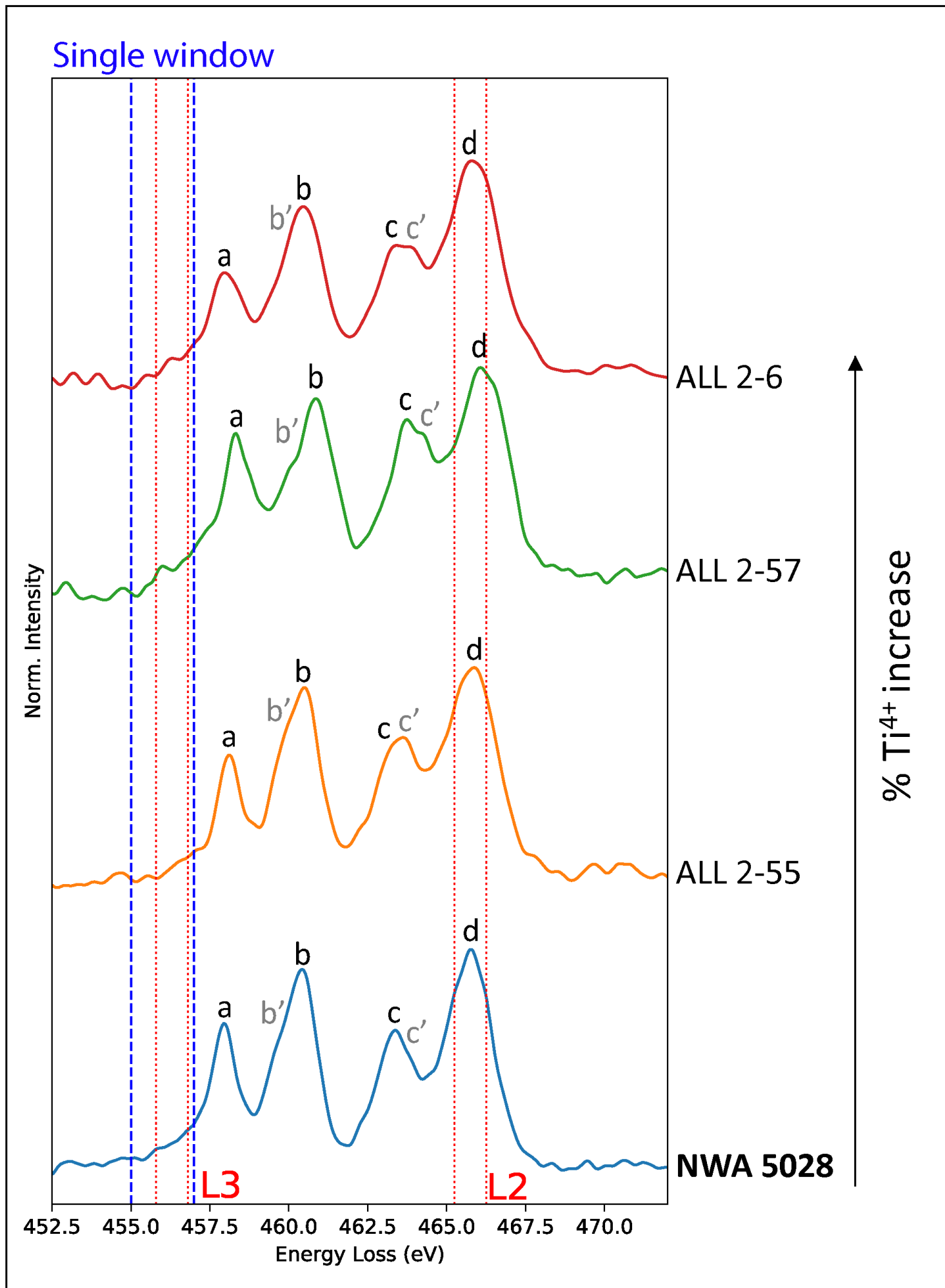


Figure 3

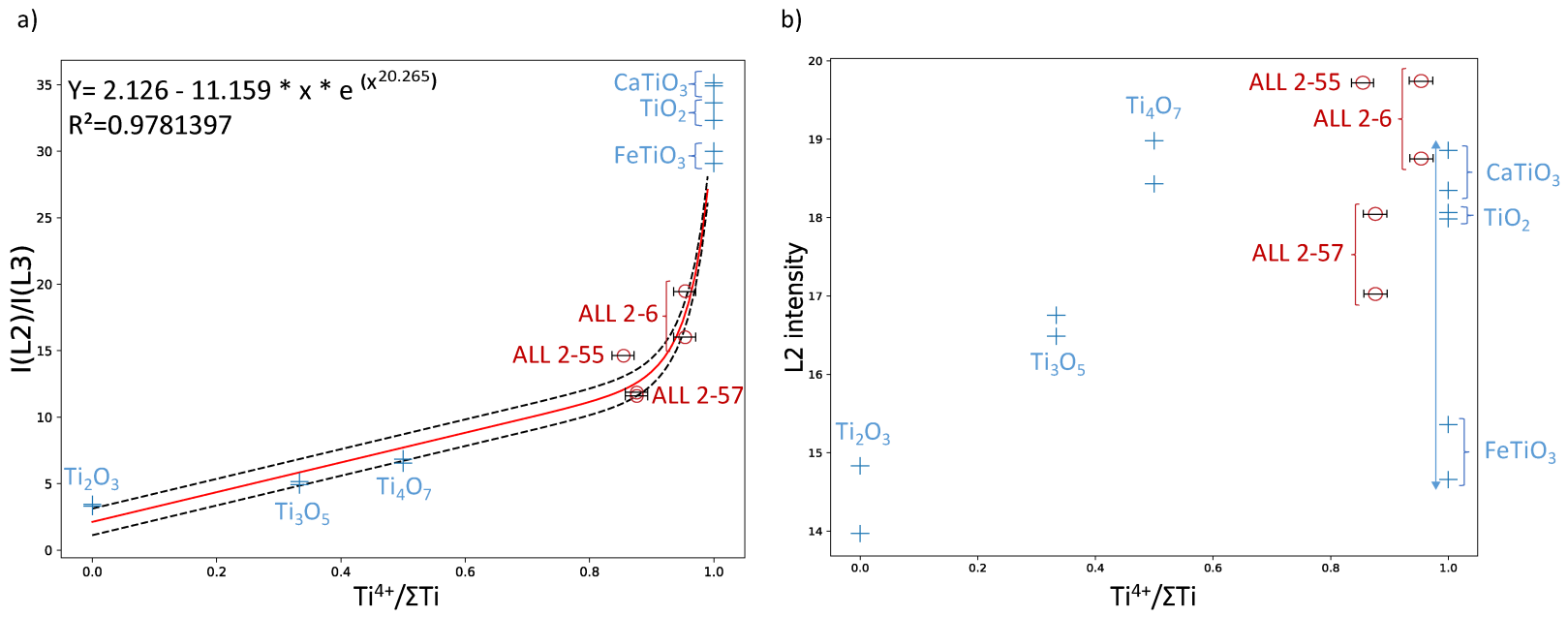


Figure 4

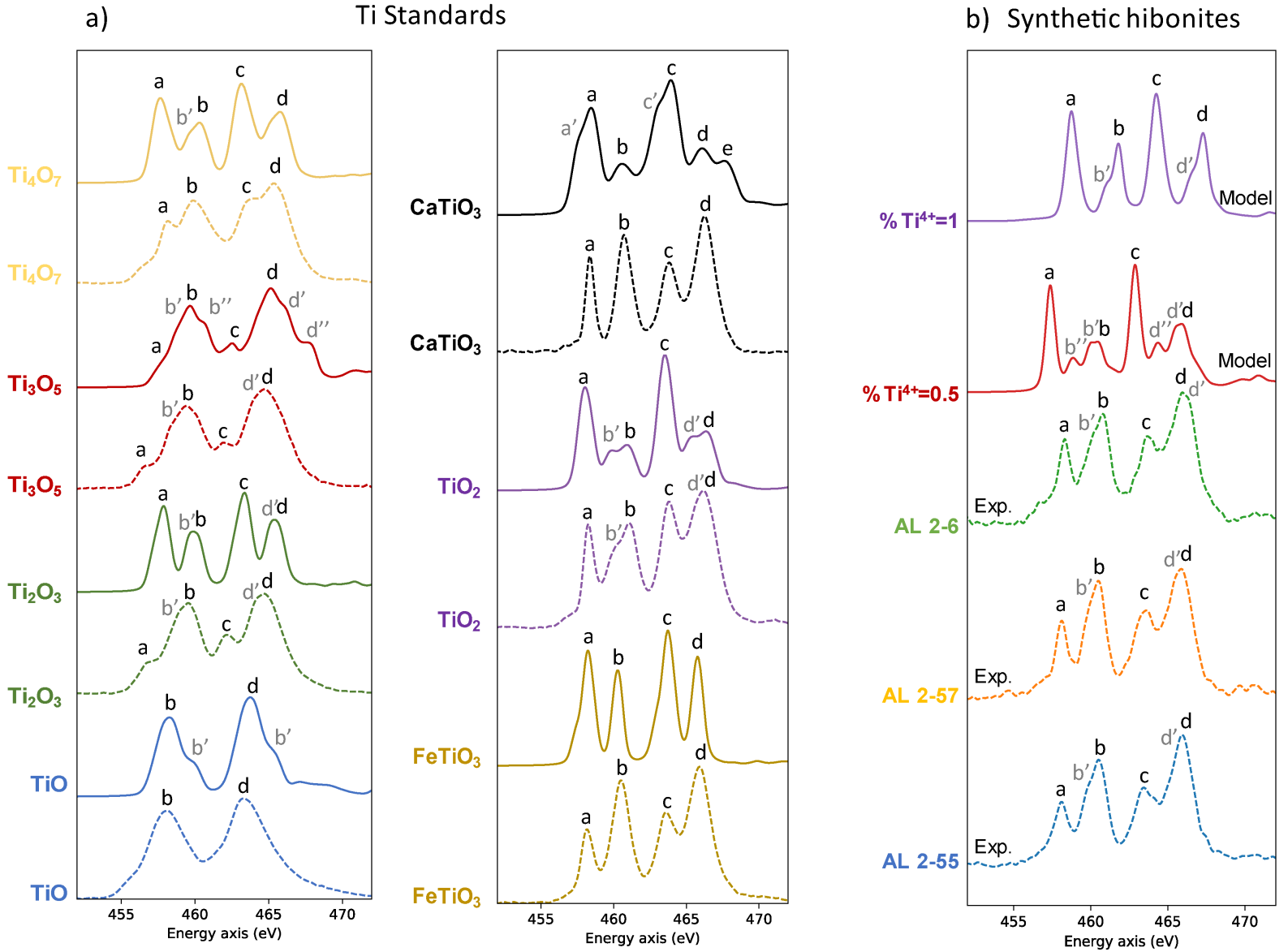


Figure 5

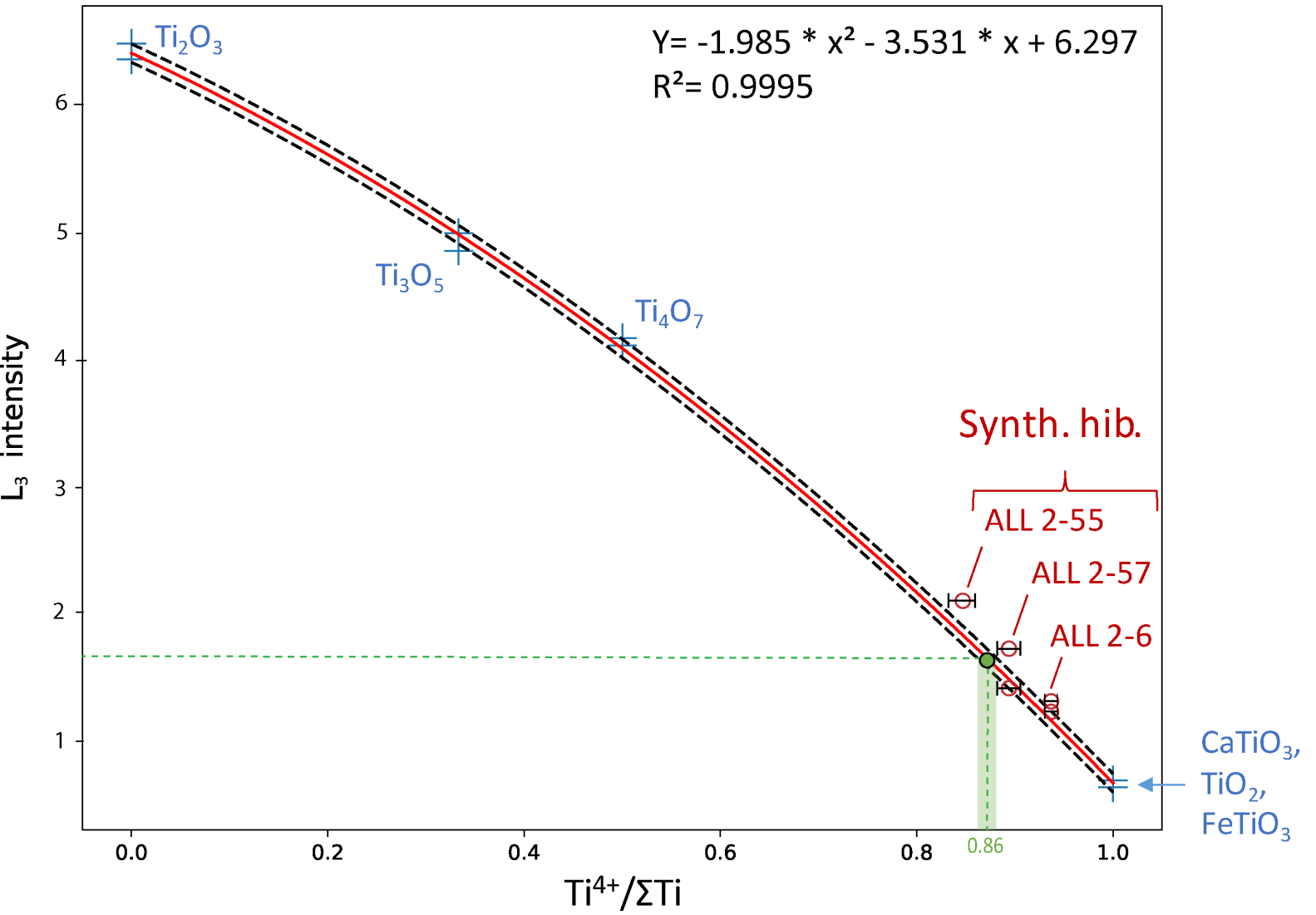


Figure 6

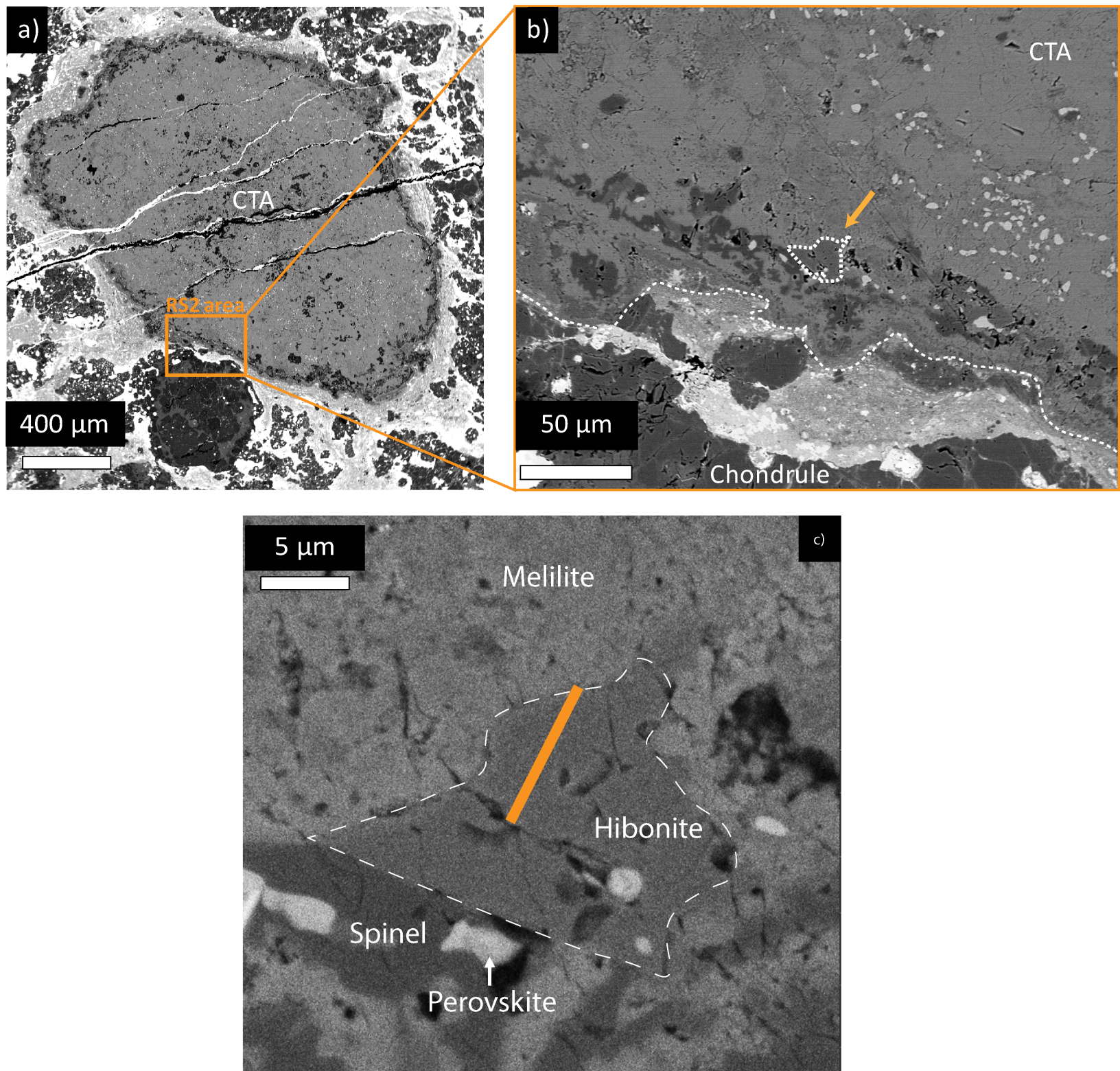


Figure 7

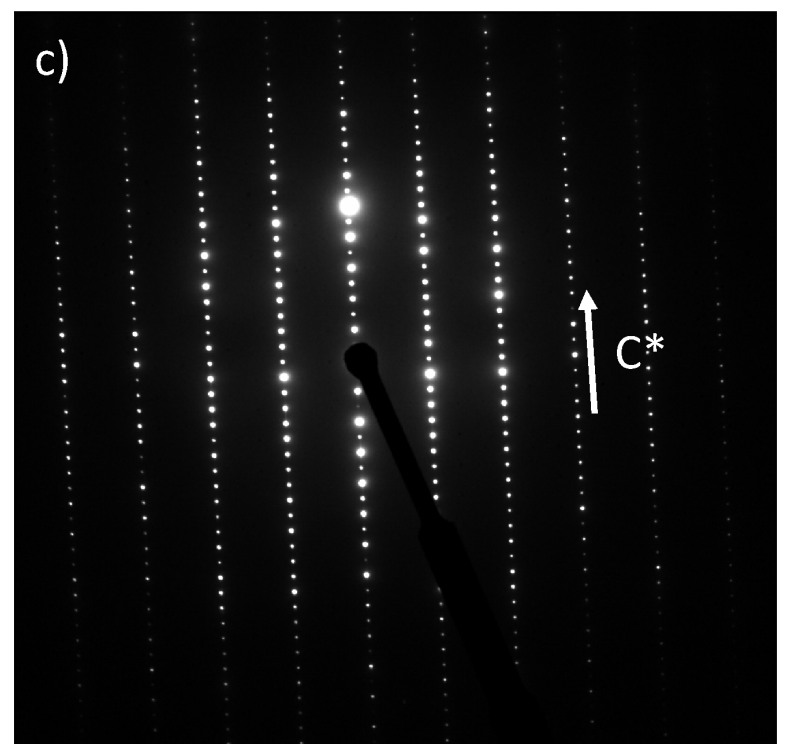
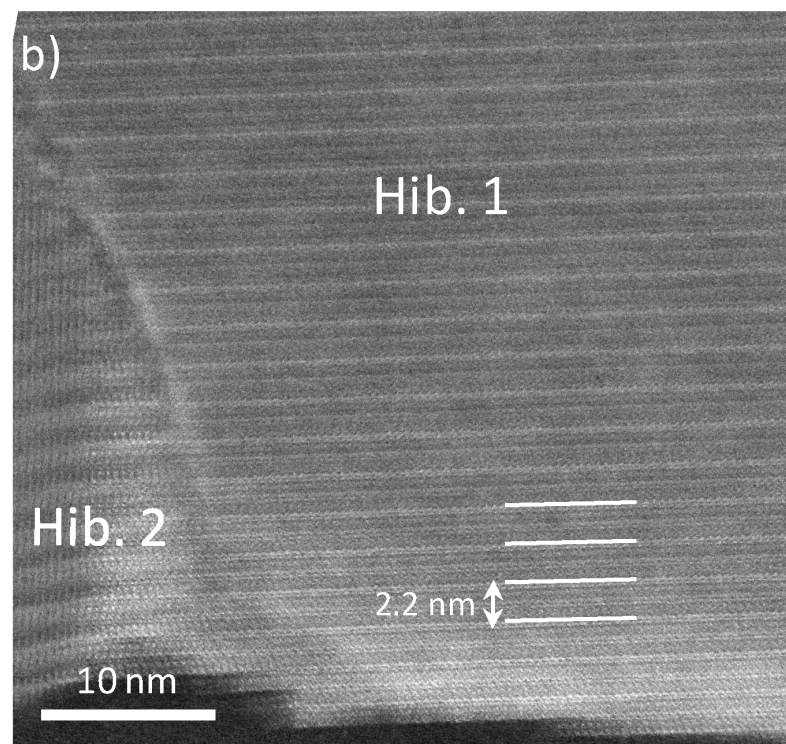
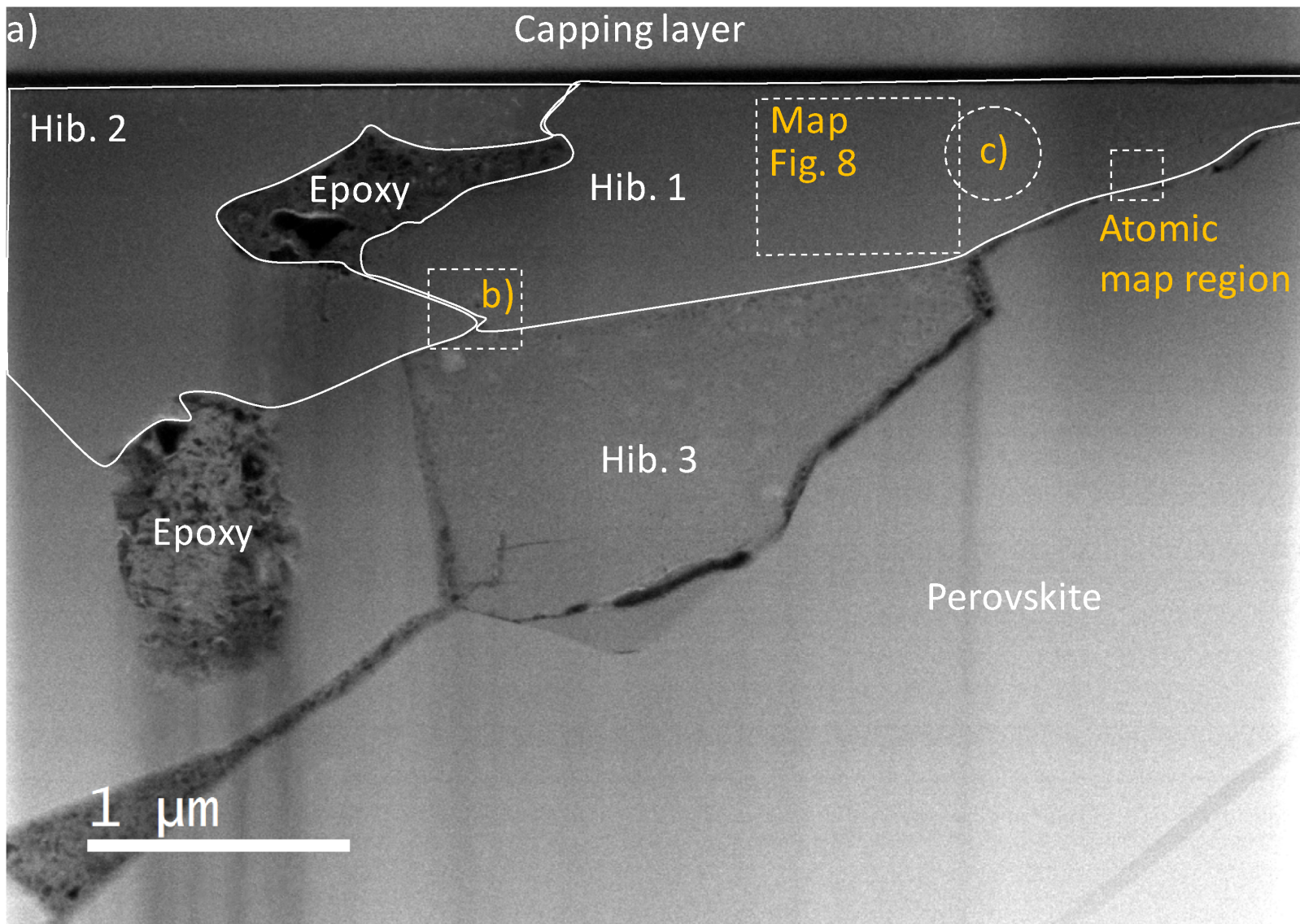


Figure 8

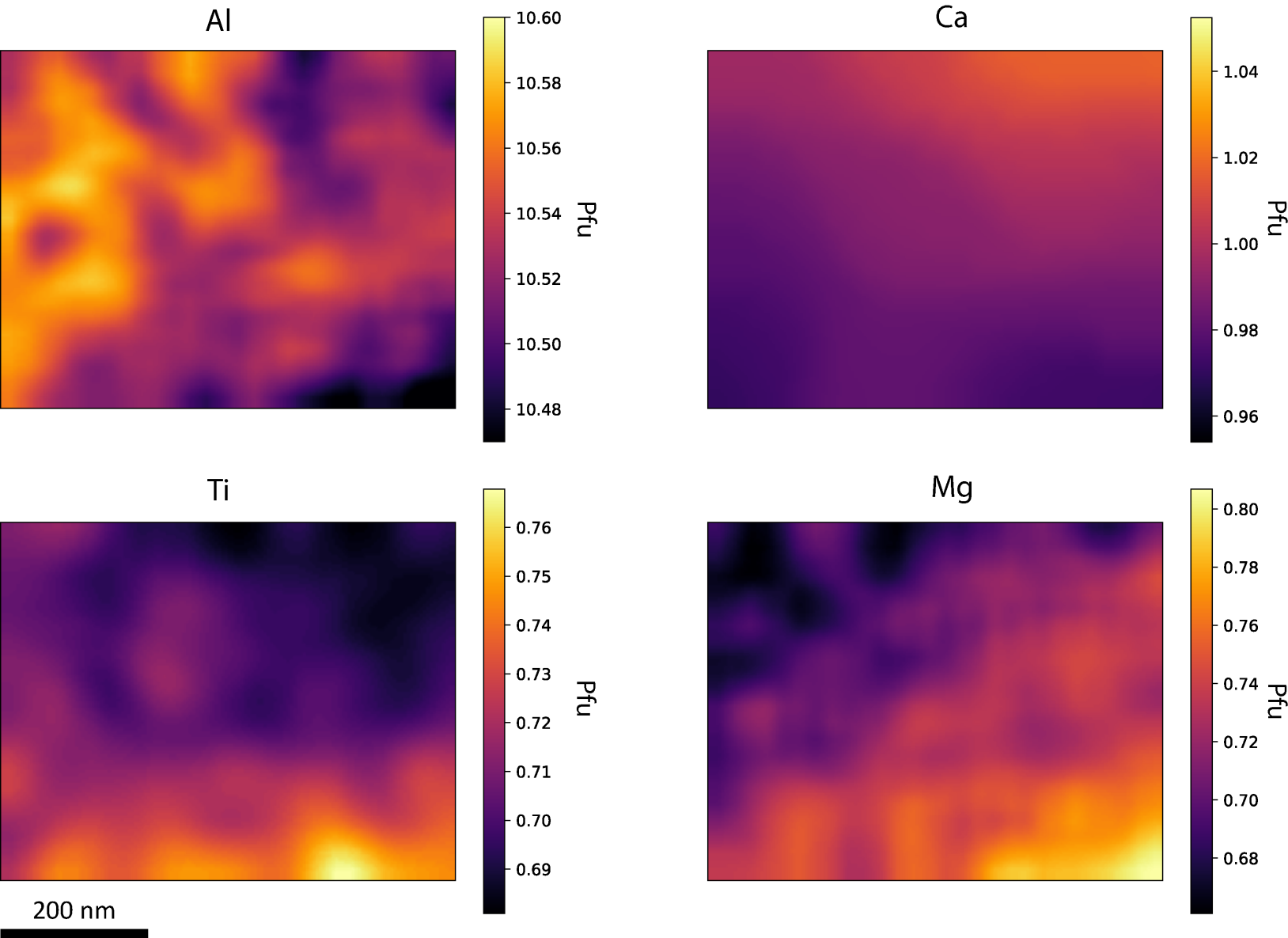


Figure 9

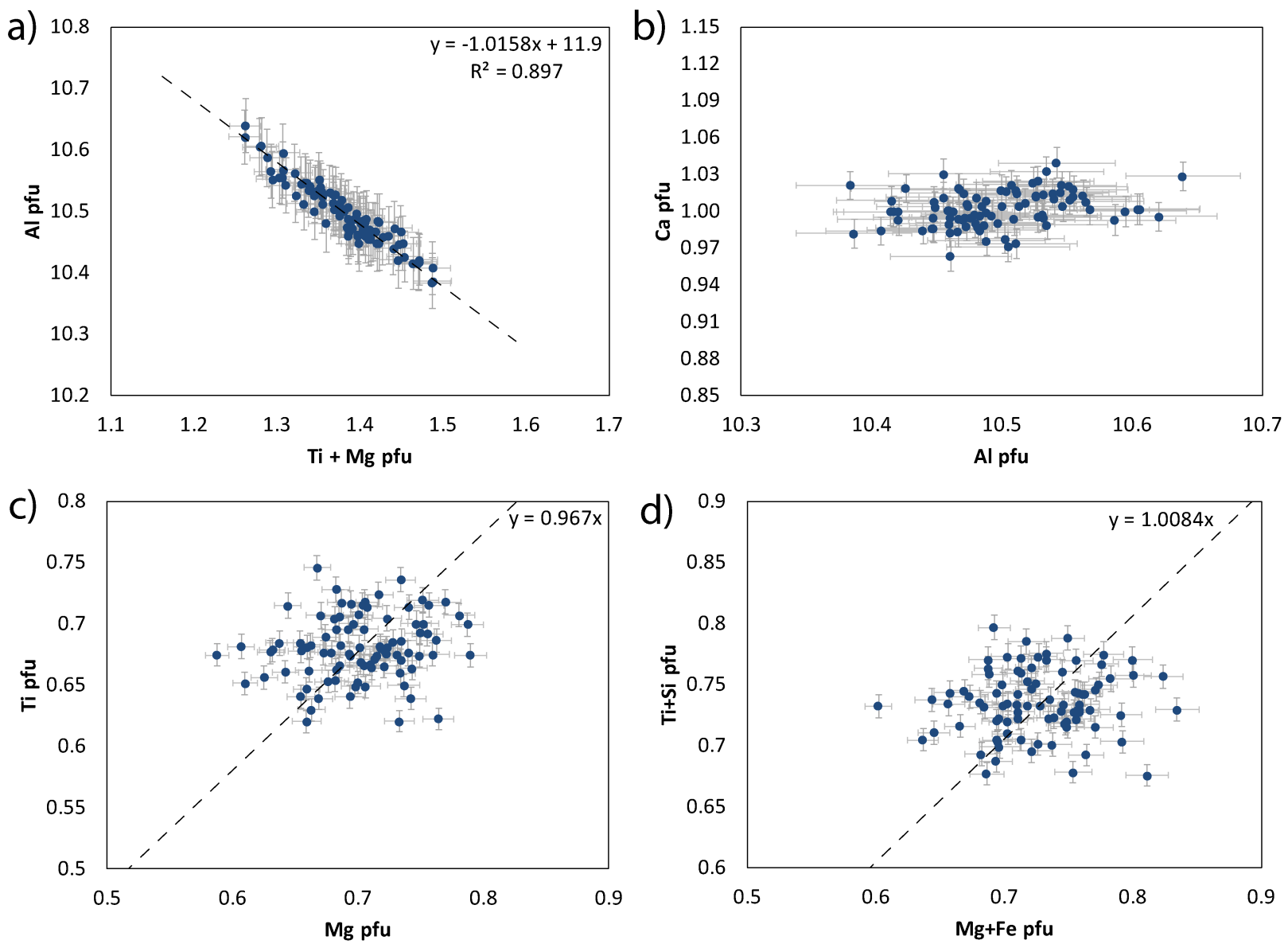
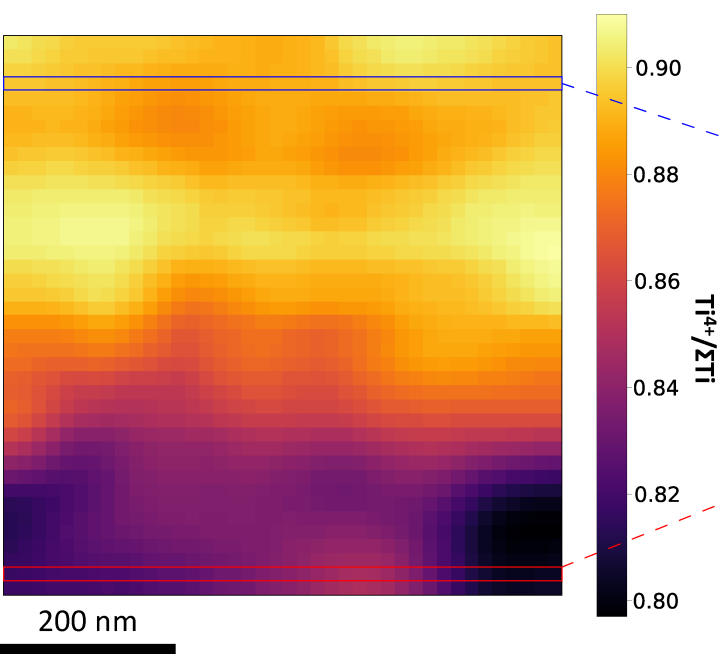


Figure 10

a)



b)

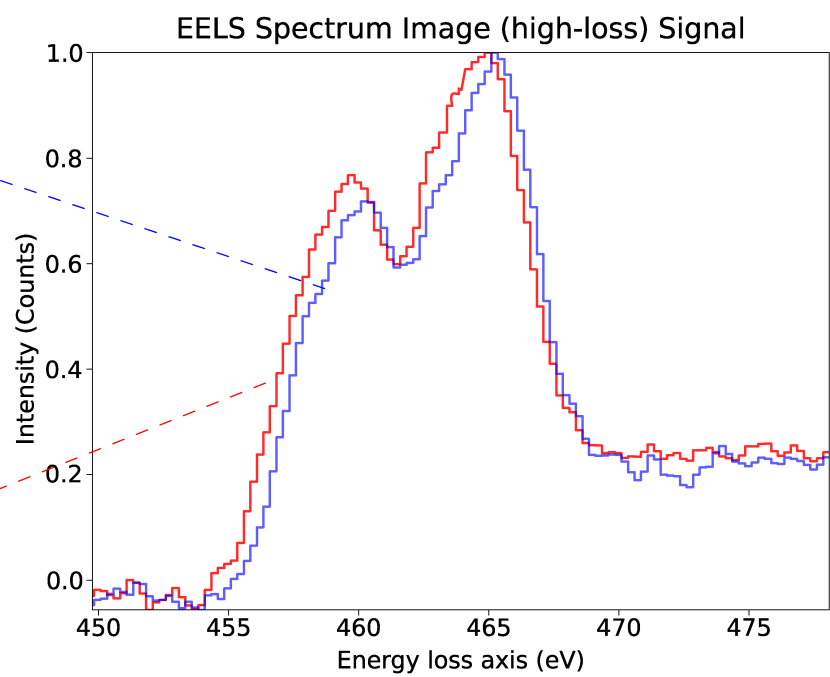


Figure 11

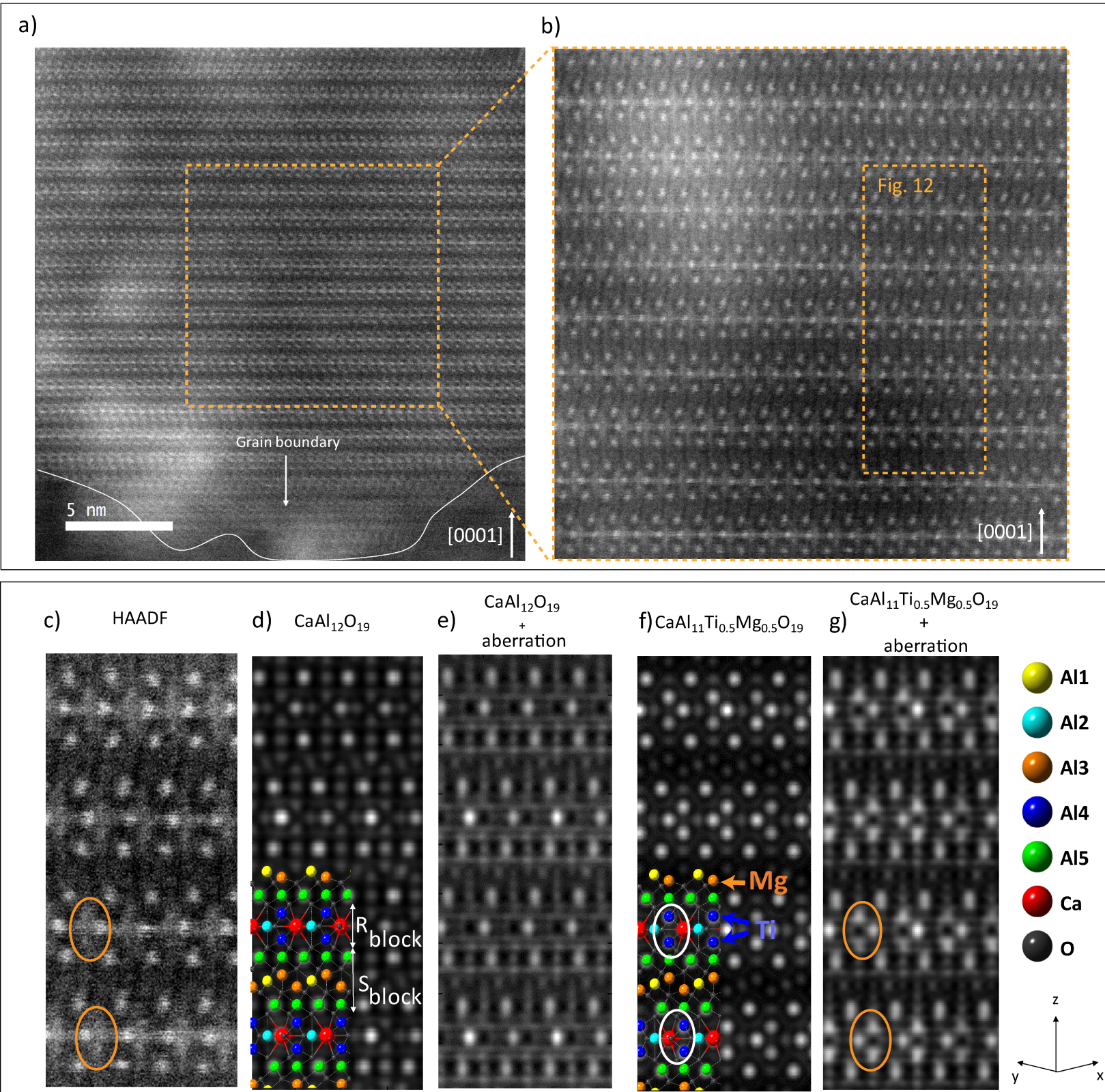


Figure 12

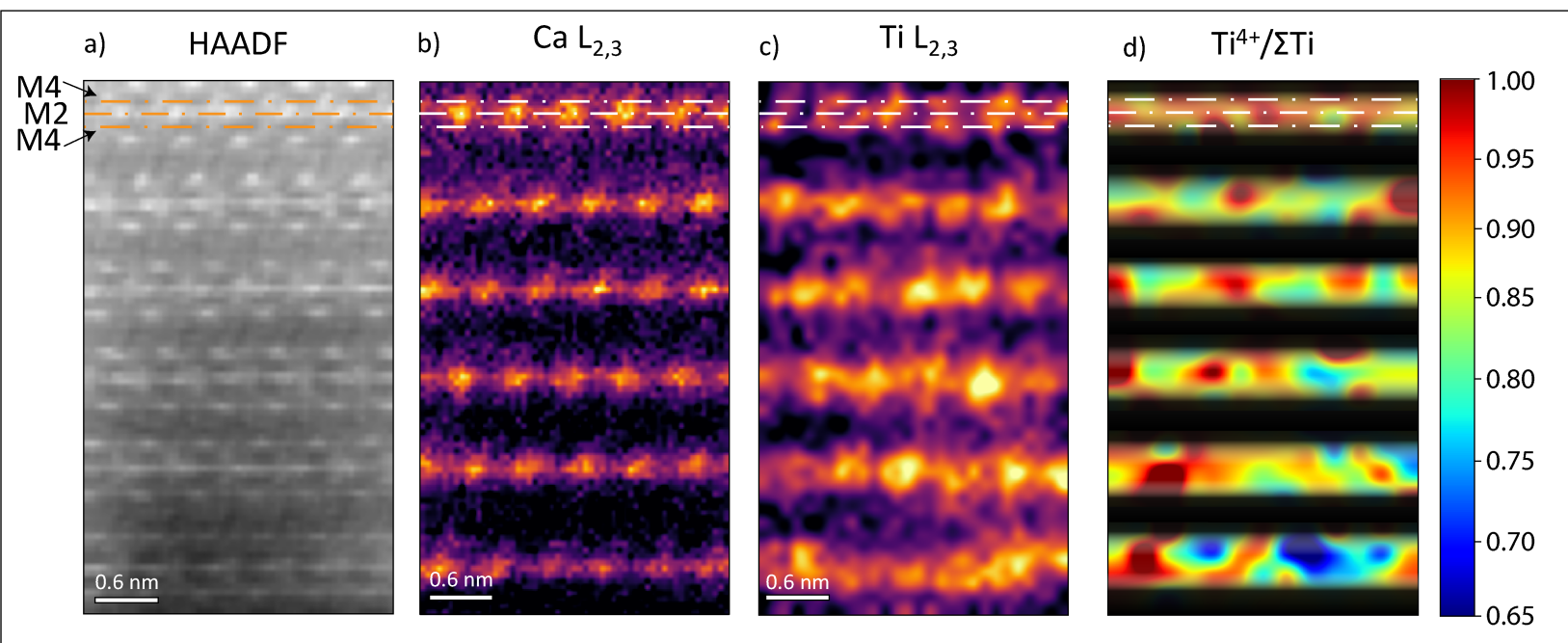
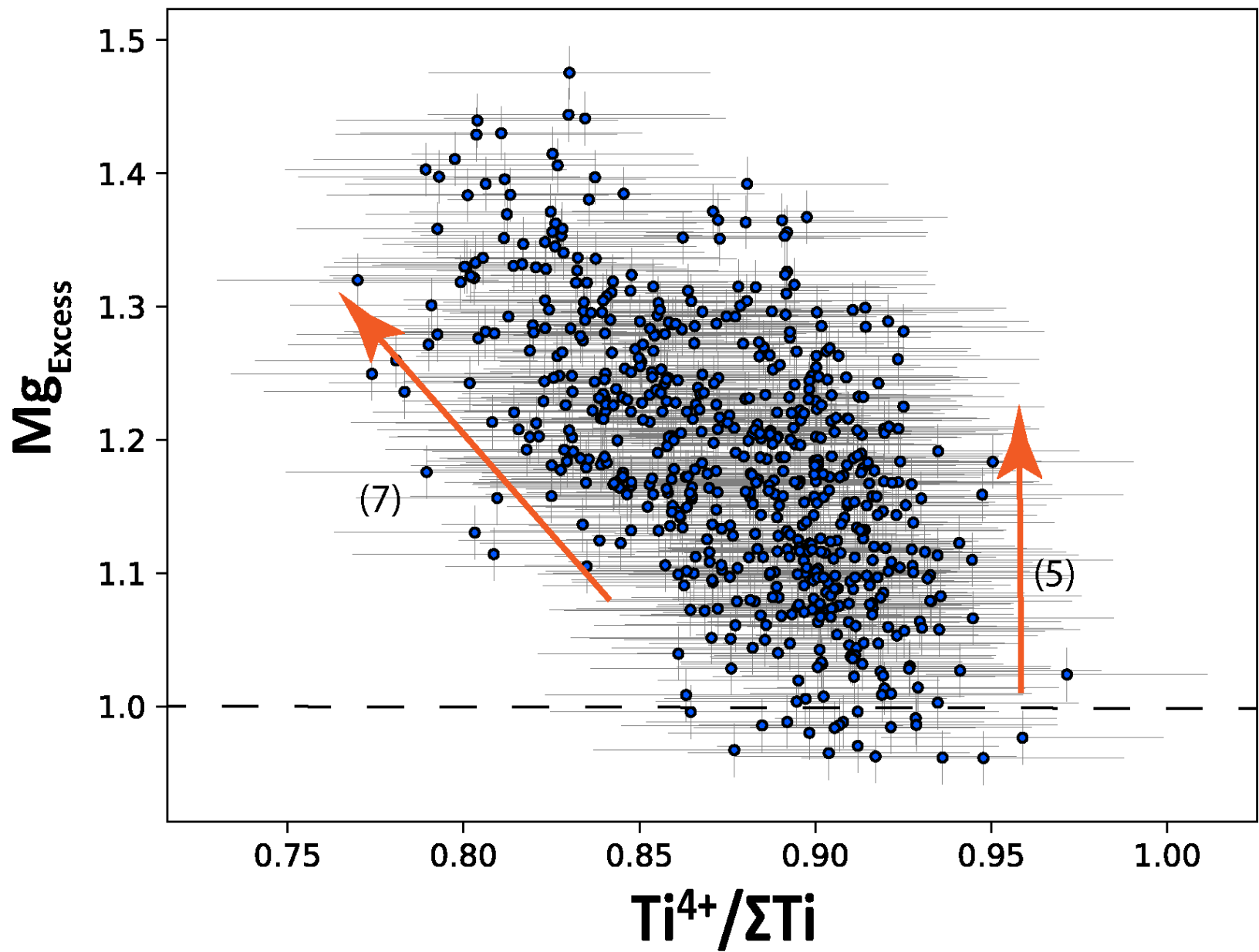


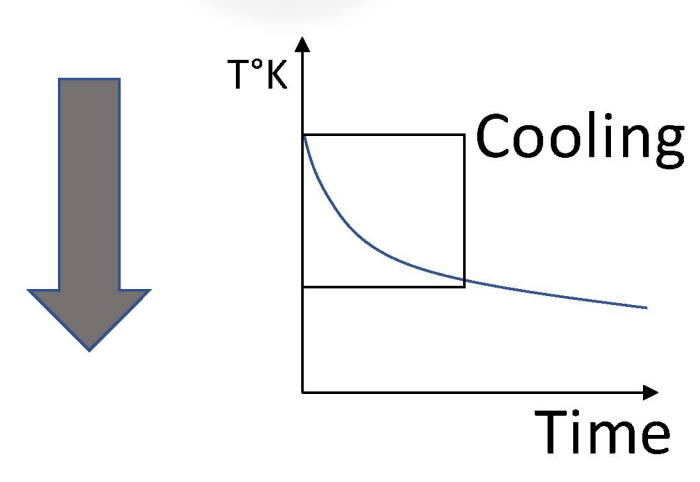
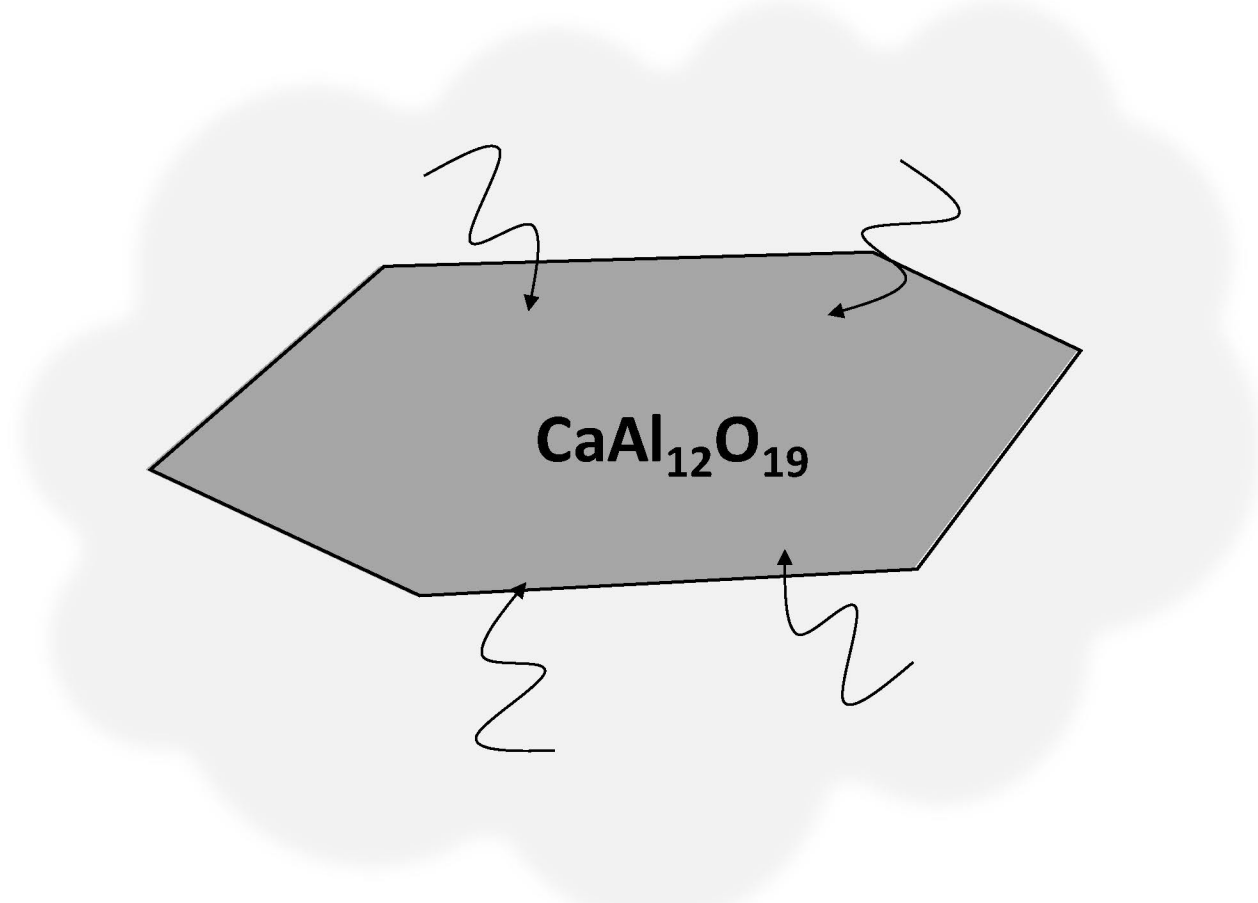
Figure 13



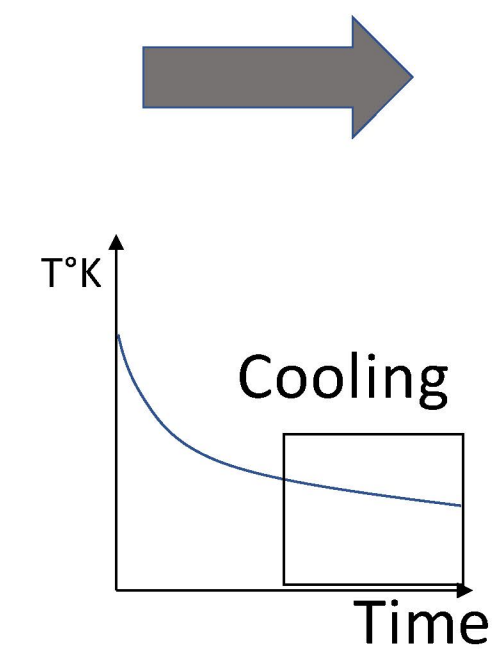
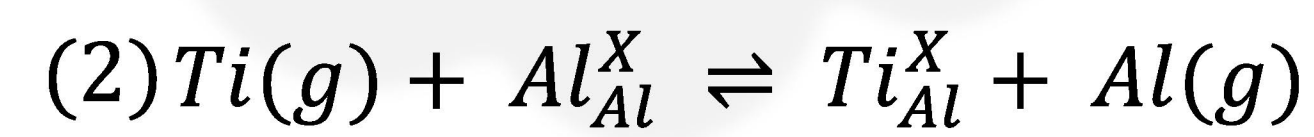
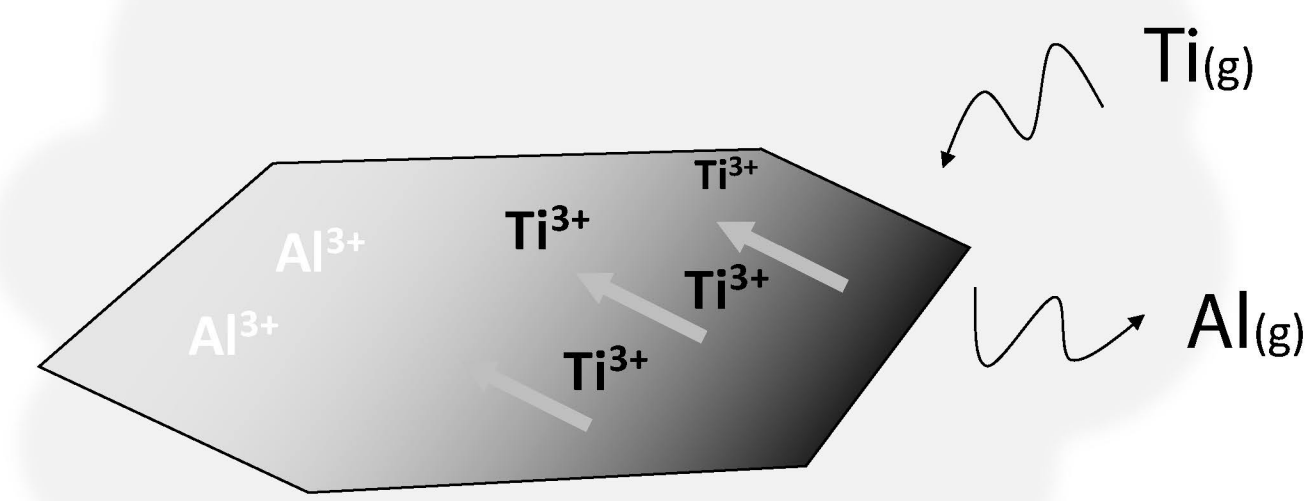
1

Compositional heterogeneities arise from initial condensation

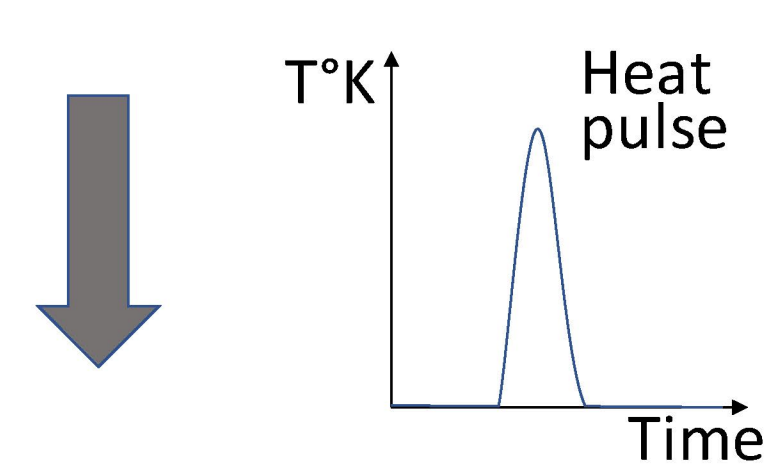
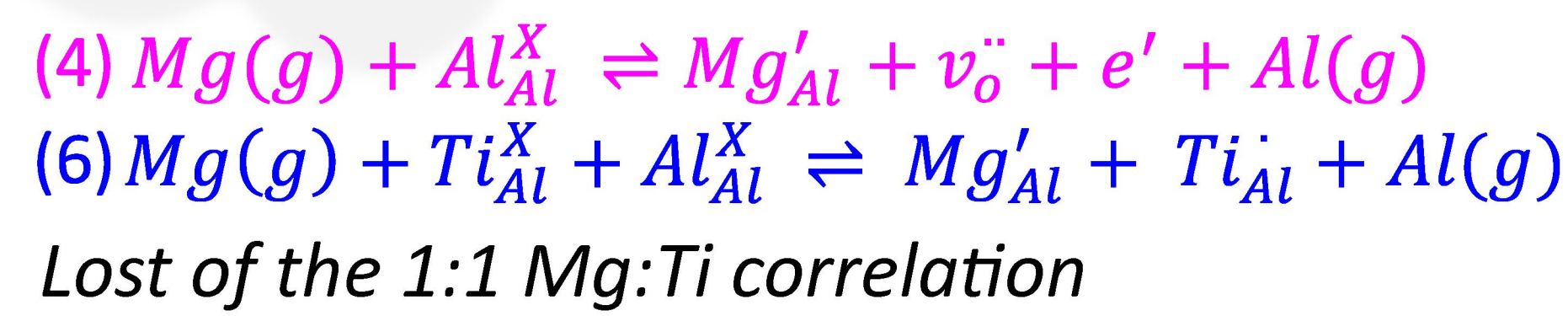
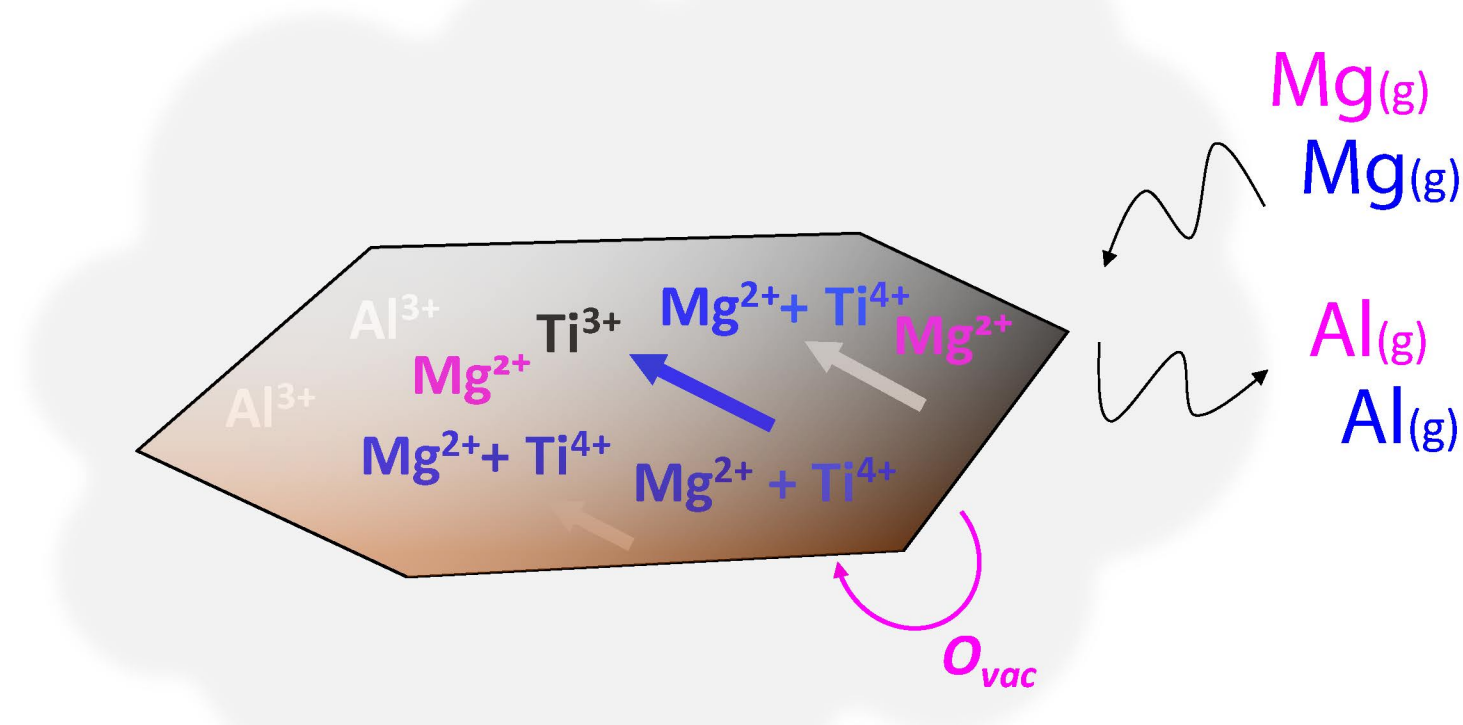
a) Solid-gas interaction



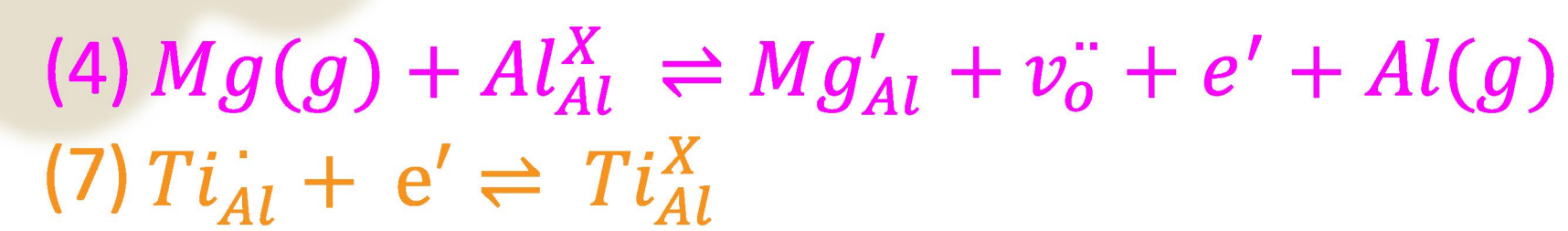
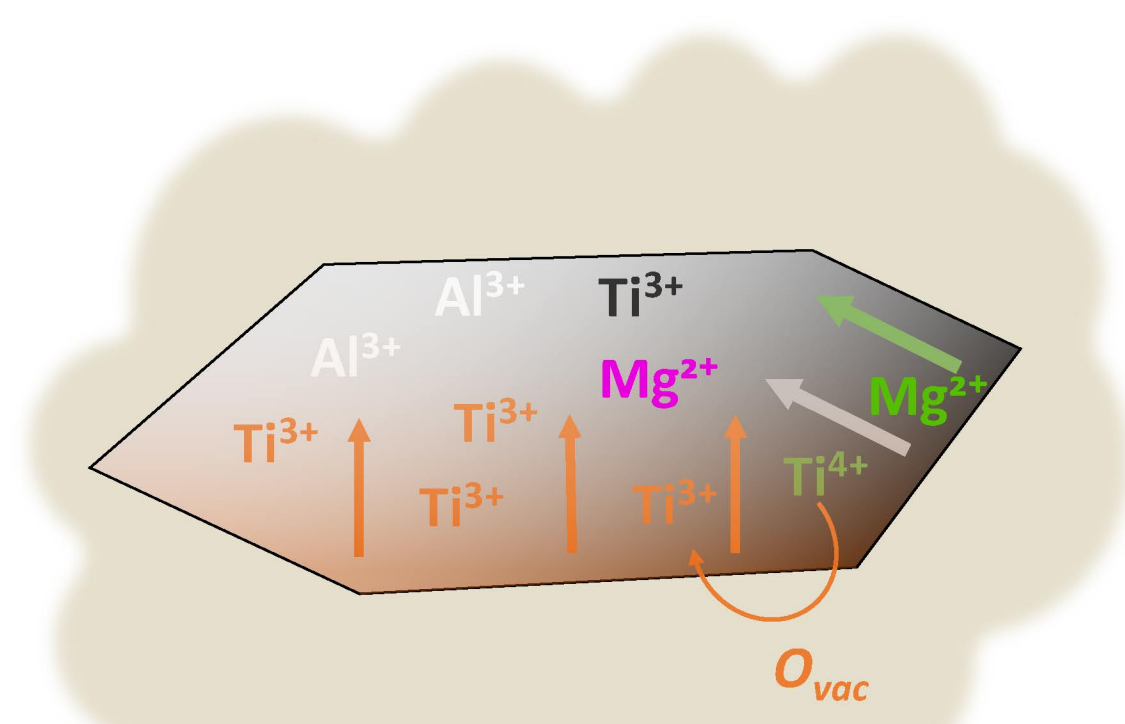
b) Ti incorporation



c) Mg incorporation



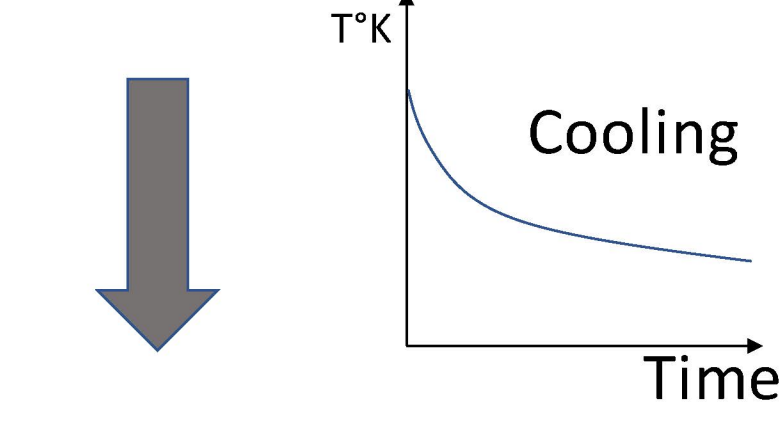
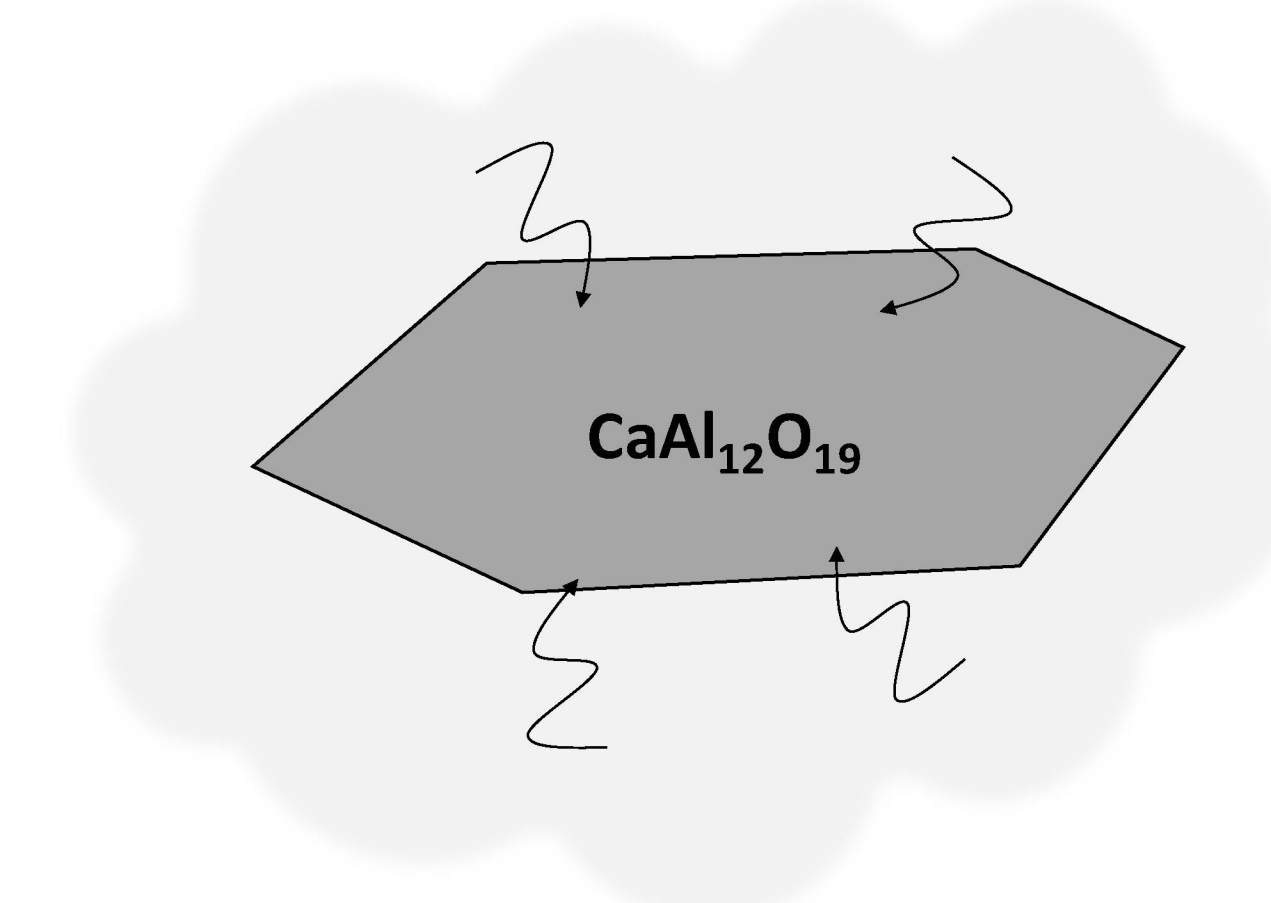
d) Possible redistribution of Ti and Mg and formation of new oxygen vacancies



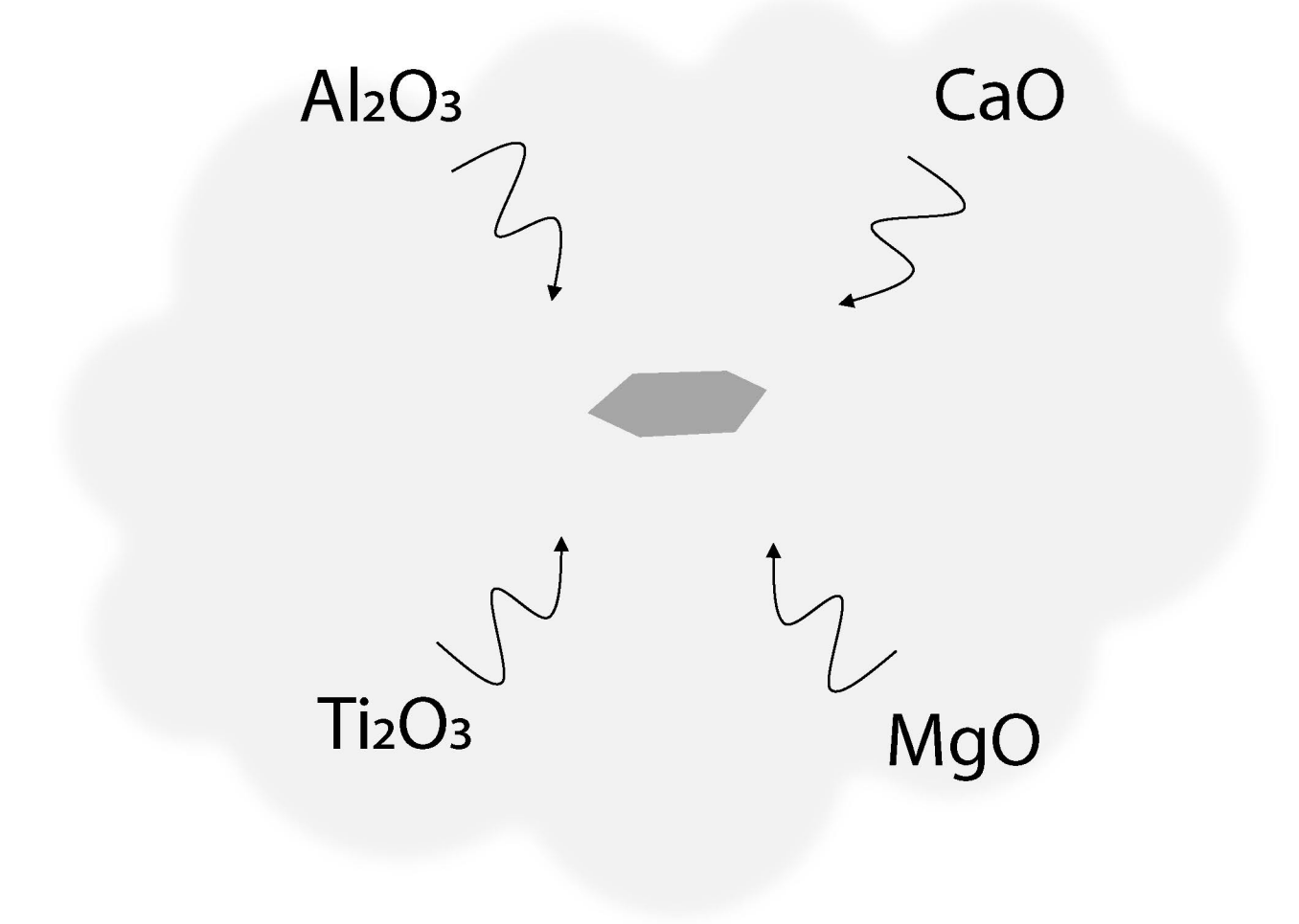
2

Compositional heterogeneities are inherited from a nebular transient thermal event

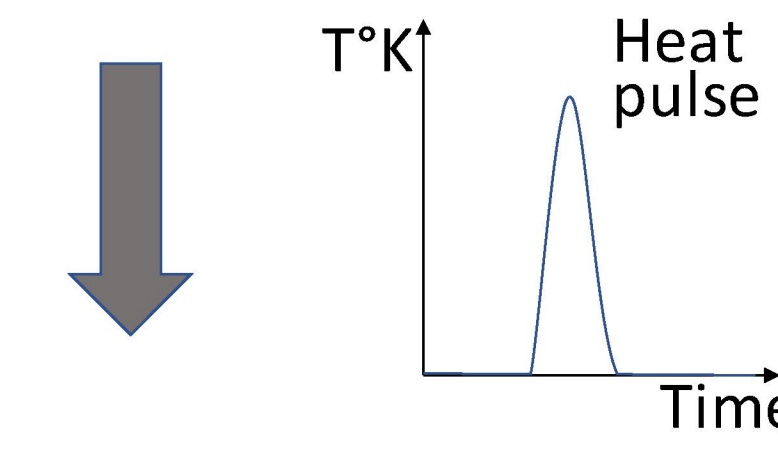
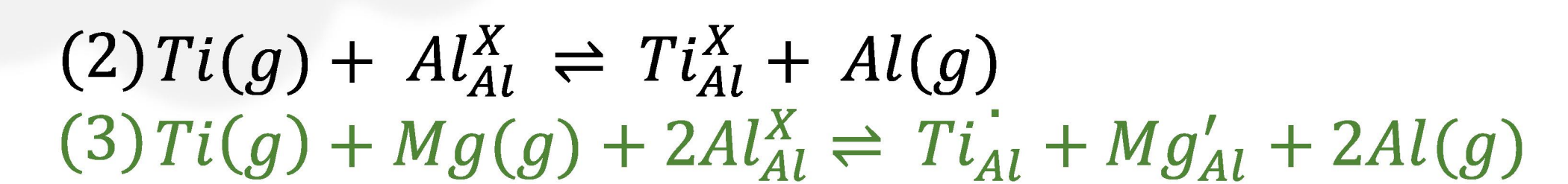
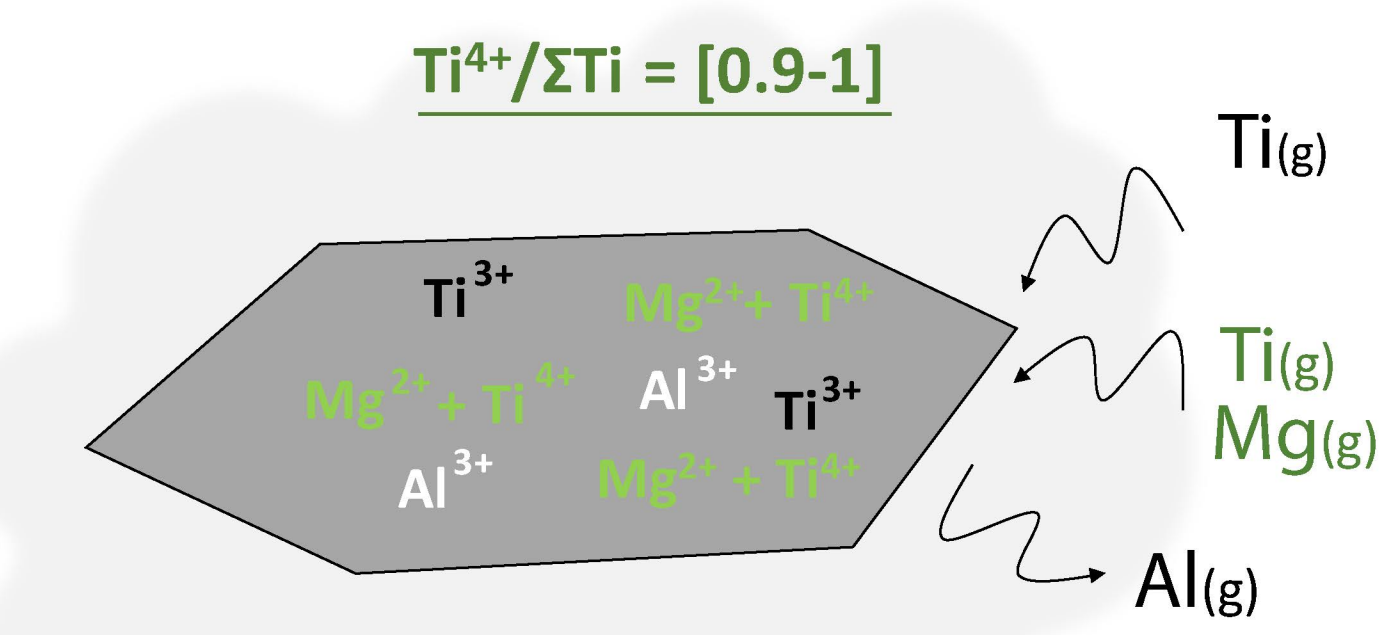
a) Solid-gas interaction



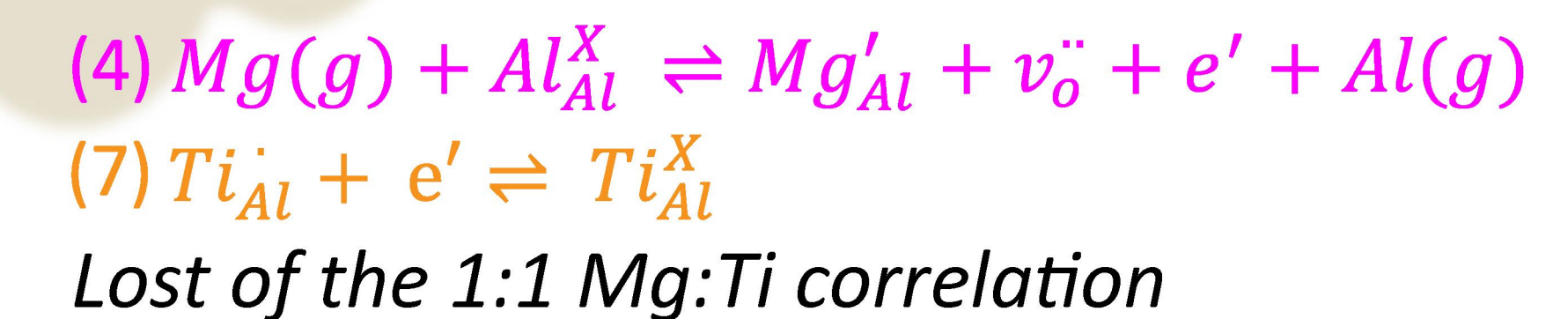
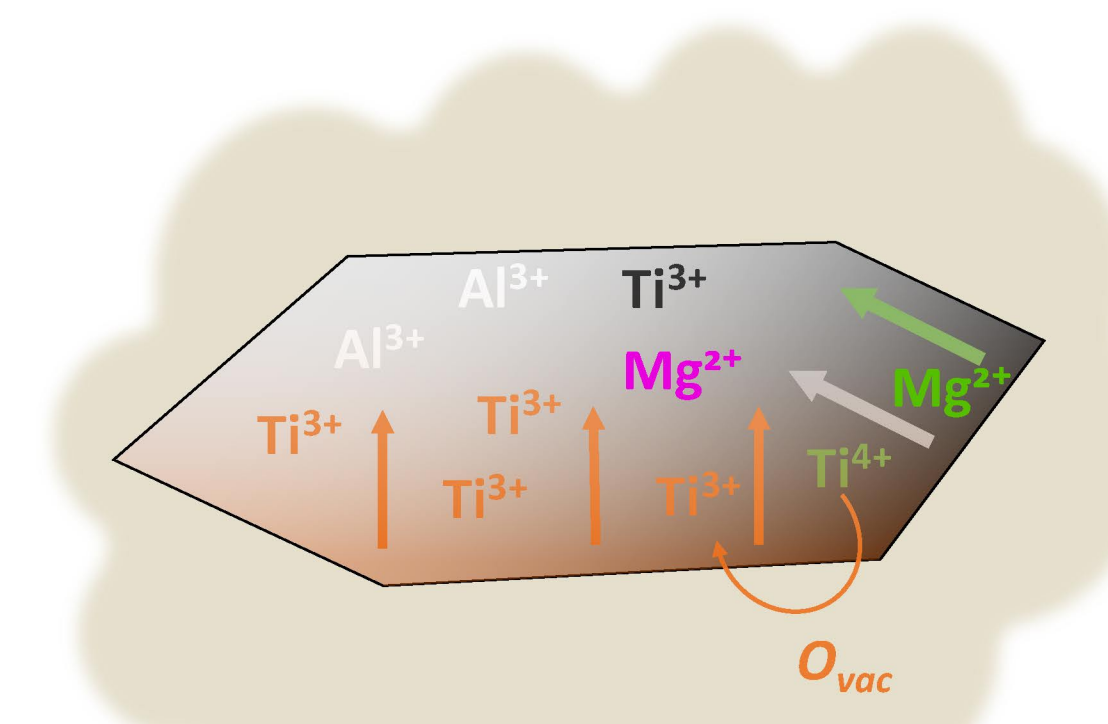
b) Direct condensation



c) Homogeneous distribution



d) Redistribution of Ti and Mg and O vacancies formation



Stage 1

Stage 2
CTA phase